DYNAMIC FEEDBACK PULSE SHAPING FOR HIGH POWER CHIRPED PULSE AMPLIFICATION SYSTEMS

by

DAT NGUYEN
M.Sc. University of Minnesota, Twin Cities 2007

A dissertation submitted in partial fulfillment of the requirements
for the degree of Doctor of Philosophy
in the Department of Physics
at the University of Central Florida
Orlando, Florida

Summer Term
2011

Major Professor: Peter J. Delfyett

ABSTRACT

The topic of this proposal is the development of high peak power laser sources with a focus on linearly chirped pulse laser sources. In the past decade chirped optical pulses have found a plethora of applications such as photonic analog-to-digital conversion, optical coherence tomography, laser ranging, etc. This dissertation analyzes the aforementioned applications of linearly chirped pulses and their technical requirements, as well as the performance of previously demonstrated parabolic pulse shaping approaches.

The experimental research addresses the topic of parabolic pulse generation in two distinct ways. First, pulse shaping technique involving a time domain approach is presented, that results in stretched pulses with parabolic profiles with temporal duration of 15 ns. After pulse is shaped into a parabolic intensity profile, the pulse is compressed with DCF fiber spool by 100 times to 80 ps duration at FWHM.

A different approach of pulse shaping in frequency domain is performed, in which a spectral processor based on Liquid Crystal on Silicon technology is used. The pulse is stretched to 1.5 ns before intensity mask is applied, resulting in a parabolic intensity profile. Due to frequency to time mapping, its temporal profile is also parabolic. After pulse shaping, the pulse is compressed with a bulk compressor, and subsequently analyzed with a Frequency Resolved Optical Gating (FROG). The spectral content of the compressed pulse is feedback to the spectral processor and used to adjust the spectral phase mask applied on the pulse. The resultant pulse

after pulse shaping with feedback mechanism is a Fourier transform, sub-picosecond ultrashort pulse with 5 times increase in peak power.

The appendices in this dissertation provide additional material used for the realization of the main research focus of the dissertation. Specification and characterization of major components of equipments and devices used in the experiment are present. The description of Matlab algorithms that was used to calculate required signals for pulse shaping are shown. A brief description of the Labview code used to control the spectral processor will also be illustrated.

In dedication to my family, and friends, for all the support.

ACKNOWLEDGMENTS

The author would like to express his gratitude to his friends and family for support and encouragement during my time in graduate school. I would like to thank my advisor, Professor Peter J. Delfyett for his guidance toward my Ph.D. thesis, thanks for my mentor and peers from my Ultrafast Photonics group: Dr. Shinwook Lee, MS Scott Rozzo, Dr. Dimitrios Mandridis, Dr. Ibrahim Ozdur, Dr. Sarpur Ozharar, thanks for my colleagues Dr. Umar Piracha, Sharad Bhooplapur, Nazanin Hoghooghi, Dr. Charles Williams, Dr. Josue Davila-Rodriguez, Marcus Bagnell Abhijit Ardey, Christina Bagnell, and Anthony Klee for valuable contribution, discussion, idea and help to this work.

I also would like to give thanks to my faithful friends from other walk of life, especially people from my time in University of Minnesota, Twin Cities: Dr. Alexander Scott, Prof. Bradley (Peanut) McCoy, Dr. Sujeewa Kumaratunga, MSc. Byoungsoon Kim, Dr. Junchung Kim, Dr. Masaya Nishioka, Dr. Hyuk-jae Chang.

Thanks for friends I met and got to know in Orlando, I can only list a few of you here, but you know who you are Dr. Philip Marraccini, Betsy Kuruvilla, Lauren Fielding, Craig and Jennifer Constantinos, Mike and Rachel Rapacz, Naomi Parks, Shannon O'Donoghue, Alison Milliner, Javier Peres-Cardareli, Dr. Abiy Agiro, Noah Seta, Ashley Kennard, and many others… you make this bearable.

TABLE OF CONTENTS

LIST OF FIGURES

LIST OF TABLES

LIST OF ACRONYMS/ABBREVIATIONS

ADC	Analog-to-Digital Conversion
AM	Amplitude Modulation
ASE	Amplified Spontaneous Emission
CFBG	Chirped Fiber Bragg Grating
CFF	Cavity Fundamental Frequency
CPA	Chirped Pulse Amplification
CW	Continuous Wave
dB	Decibel
dBm	Decibel relative to 1 mW
DCF	Dispersion Compensating Fiber
DFB	Distributed Feedback
DFT	Discrete Fourier Transform
EDFA	Erbium Doped Fiber Amplifier
FDML	Fourier Domain MLL
FSR	Free Spectral Range

FWHM	Full Width Half Maximum
IM	Intensity Modulator
LCoS	Liquid crystal on Silicon
MLL	Mode-Locked Laser
NLSE	Nonlinear Schrodinger Equation
OCT	Optical Coherence Tomography
OTD	Optical Time Delay
PM	Phase Modulation
PMF	Polarization Maintaining Fiber
PSD	Power Spectral Density
RF	Radio Frequency
RMS	Root Mean Square
SBS	Stimulate Brillouin Scattering
SHG	Second Harmonic Generation
SMF	Single Mode Fiber (usually SMF-28e)
SNR	Signal-to-Noise Ratio

SRS	Stimulate Raman Scattering
SSFM	Split Step Fourier Method
TS	Time Stretch
t-λ	Time-to-Wavelength
WDM	Wavelength Division Multiplexing
WSS	Wavelength Selective Switch
X-CPA	eXtreme Chirped Pulse Amplification

CHAPTER 1: CHIRPED PULSE AMPLIFICATION

1.1 Introduction to Chirped Pulse Amplification

In amplifiers for ultrafast optical pulses, the optical peak intensities that occur can become extremely high, so that detrimental nonlinear pulse distortion or even destruction of the gain medium or some other optical elements can happen. This can be effectively prevented by employing the method of chirped pulse amplification (CPA), which was originally developed in the context or radar technology, but later applied to optical amplifier. Chirped pulse amplification is currently the state of the art technology, which is being employed by all the highest power lasers with output power greater than 100 terawatts.

As an introduction, some systems that either use or can benefit from uniform-intensity linearly-chirped optical pulses at low repetition rate are discussed in the following section. Chapter 1 contains a review of applications for extremely chirped pulses and a literature review on the generation of chirped pulses.

Chapter 2 describes in detail different approaches to generate of parabolic pulses for chirped pulse amplification; specific implementation fiber tailoring techniques.

Chapter 3 and 4 contains the student's experimental work. The work focuses on two distinct approaches for the generation of the parabolic pulses based on time domain optical Fourier transformation approach and frequency domain optical Fourier transformation approach.

Chapter 5 explores the spectral phase characterization utilizing interferometry approach. The work focuses on measuring the optical spectral phase of the CPA laser system with much faster acquisition time; that allows real time measurement and feedback to the optical spectral processor to achieve high quality pulses and faster time response than the FROG-based approach. This approach also reduces footprint of the system, simple to implement, significantly reduces cost of optical parts in the setup. Comparison of results from this approach and FROG shows that this is indeed a reliable approach.

The final part of the thesis discusses the future directions and potential next steps of research to the work presented.

1.2 Frequency Chirped Pulse Applications

1.2.1 Short pulse amplification in optical fibers

Many applications of ultrashort pulses require high power optical pulses with energy exceeding 1 J. That energy is not directly available from the laser producing pulse train. Therefore it is necessary to amplify the pulse externally to reach the required energy level. Currently the state-of-the-art technique for this purpose is known as the chirped pulse amplification approach [1–11]. This technique was first introduced in 1974, but received widespread attention only after 1985 when D. Strickland, G. Mourou and co-workers reported terawatt peak power in their amplification experiment of short pulses [1–3,6].

The most common nonlinear phenomenon in optical fibers originates from the third-order susceptibility ($\chi^{(3)}$) when pulses propagate through fiber, usually referred as self-phase modulation (SPM) effect. The second important nonlinear effect results from stimulated inelastic scattering, leading to significant loss of power in the form of excited vibration modes [12]. A large frequency shift of approximately 13 THz is called stimulated Raman scattering (SBS), due to the excitation of optical phonons. A smaller shift approximately 17 GHz is called stimulated Brillouin scattering as a result of the excitation of acoustic phonons [13]. In this experiment, due to the broad nature of the bandwidth of our mode-locked laser (MLL), much larger than the Brillouin gain bandwidth, the SBS effect can be ignored, and our focus would be on limiting the negative effects of SPM [14].

The basic principle behind CPA is to use a nonlinear medium to stretch the pulse before amplification. Due to short temporal duration of the ultrashort pulses, when ultrashort pulses propagate through the gain media, there will be gain saturation as well as other detrimental effects associated with high peak power such as pulse distortion, self-phase modulation and nonlinearity processes that severely limit the amplification of pulse power. This is especially true for the fiber amplification systems, where the confinement of the laser radiation and the long interaction length makes fiber attractive for solid state laser system; however nonlinear effects impose fundamental limitations on the systems, which may lead to severe pulse distortion and damage to fiber [5].

Pulse broadening in contrast reduces the peak power, making it possible to amplify the pulse by a large amount before gain saturation limits the energy-extraction efficiency, and at the

same time avoiding possible damage to optical components of the laser systems. The use of optical fibers even though is not crucial for chirped pulse amplification; their nonlinearity provides an easy way to induce the frequency chirp on the pulse. This chirp in turn can be effectively compensated by the bulk grating compressor to maintain quality of short pulse after amplification. Further discussion of pulse broadening using CFBGs will be shown in the following chapters.

1.2.2 Chirped pulse amplification scheme

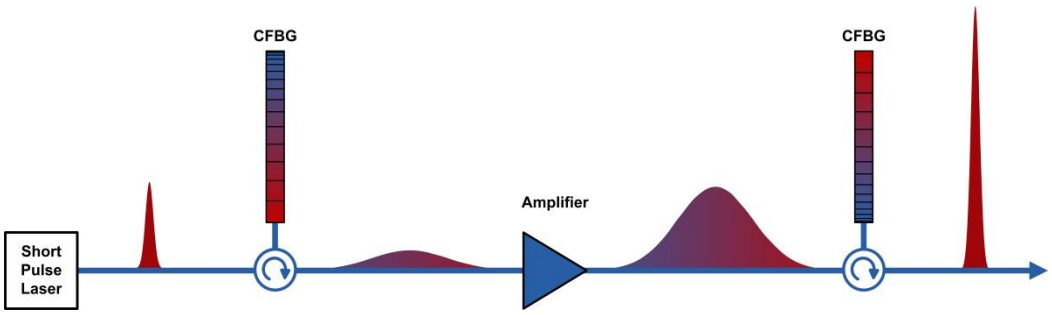

Figure 1-1: The sketch of a chirped pulse amplification system. Pulse from an utrashort MLL source is stretched with a nonlinear medium or dispersion grating. This stretched pulse is then amplified with an optical amplifier before compression with a bulk compressor to achieve high peak power pulse.

The concept of chirped pulse amplification has revolutionized the laser field, and is very useful for the amplification of femtosecond and picosecond pulses, as well as maintaining pulse fidelity before and after amplification. This technique was used in radar technology, and later

adapted to laser amplification. The principle of this technology is to expand (or stretch) the pulses before amplification, followed by pulse compression to its original shape, as illustrated in Figure 1-1. Pulse stretching is done by passing through a media that provides, for example, a positive group delay dispersion (GDD) to expand the pulse considerably in time, while acquiring a positive frequency sweep. The stretched pulse therefore preserves the bandwidth of the input pulse but lowers the peak power of the pulse by the stretching factor.

After stretching, the pulse is amplified by either single or multi-stage amplifier. Due to peak power reduction associated with stretching, nonlinear effects, self-focusing, optical damage as well as other detrimental effects are significantly suppressed. After amplification, the pulse is sent to a media, or optic systems with negative GDD. This second dispersive element compensates for the frequency sweep introduced by the first, and therefore restores the initial shape of the input pulse before amplification. This process ensures only the compressor stage is subjected to the full peak power of the final amplified pulse.

The dispersive media employed as the stretcher is usually diffraction gratings. However, other media such as high nonlinear fiber or FBG can be used as well. Typically the Treacy grating pair is built as pulse compressor, which provides anomalous dispersion. The compressor recombines spatially separated beams into a single coherent laser beam. The use of bulk compressor safeguards the compressor from possible optical damage or undesirable nonlinearity associated with high peak power pulses.

1.3 Chirped Pulse Amplification Applications

As described in the previous section, CPA technique is originally used in frequency modulated continuous wave (FMCW) radars, where a source with a long coherence length is used to achieve metrology and sensing of targets at long range [15]. Conventional FMCW lidar systems rely on tuning the wavelength of a diode laser using current injection modulation [16]. However, obtaining perfect linear optical frequency sweeps at fast sweep rates with large frequency excursions is challenging.

Recently, a new approach that relies on passively generating chirped pulses has been presented [17–19], which is based on using a CFBG for the generation of temporally stretched, frequency chirped pulses from a MLL. Unlike conventional lasers, the optical spectrum of a MLL consists of many individual axial modes that provide optical bandwidths of hundreds of GHz, sufficient for sub-millimeter range resolution. Furthermore, the coherence length of a MLL is dictated by the optical linewidth of a single axial mode, which can be in the kHz range, enabling ranging at target distances of hundreds of kilometers when coherent detection at the receiver is used. Most recently, this concept has been demonstrated by Piracha and co-workers, to achieve range resolution of sub-millimeter at 10 km distance [18,19]

The technique of chirped pulse amplification was originally introduced in the 1960s to increase radar signal power [20]. This technique has been modified and improved over the past few decades and is now also used for the amplification of optical signals [1,6,11,21–24]. Some of the current highest power laser systems are the Vulcan Petawatt Upgrade at the Rutherford

Appleton Laboratory's central laser facility, the Diocles Laser at the University of Nebraska-Lincoln, the Gekko Petawatt laser at the Gekko XII facility in the Institute of Laser Engineering at Osaka University, the OMEGA EP laser at the University of Rochester's Lab for Laser Energetics and the former petawatt line on the former Nova laser at the Lawrence Livermore National Laboratory. These laser systems employ the CPA approach to generate high optical output power.

However, in fiberized systems, when desired energy levels are in the milijoule range, linear pulse amplification is limited because nonlinearities and dispersion of the gain media can cause severe pulse distortion and consequently degrade the pulse quality. Since self-phase modulation (SPM) is proportional to the derivative of the pulse instantaneous intensity, the amplification of optical pulses with parabolic temporal intensity profile results in the generation of linear chirp that can be compensated in a straightforward manner.

Parabolic pulse generation has been demonstrated using several different techniques, but the quality of the parabolic pulses demonstrated is only moderate, because the input pulses evolve asymptotically into a near-parabolic shape [25–32]. Moreover, as the pulses propagate, even as they retain their parabolic shape, their width and amplitude changes, thus there is not a well-defined mechanism to actively and dynamically control pulse characteristics. Also, it has been shown that third order dispersion and linear absorption have detrimental effects on parabolic pulse evolution and thus, on the performance of configurations utilizing dispersion decreasing fiber [33].

Recently, a technique for dynamic shaping of pulses has been demonstrated using an approach based on the temporal stretching of pulses using a dispersion element [34,35]. This technique enables dynamic control of the pulse properties such as pulse shape, pulse width and amplitude with high resolution and a large signal to noise ratio making it suitable for a variety of applications including super-continuum generation, optical communication, high power femtosecond laser amplification, and chirped pulse amplification. This approach is described in detail in CHAPTER 2:.

CHAPTER 2: PRINCIPLES OF PARABOLIC PULSE SHAPING

2.1 Introduction to Parabolic Pulse Shaping

Data processing utilizing photonic technologies in the optical domain has very promising potential for many applications in various areas such as optical communications, metrology, optical sensing, micro-engineering, microscopy image processing, optical computing and many others. The advantages of processing information in the optical domain consist of large bandwidth and high processing speeds. Therefore, techniques for generating, controlling and manipulating ultrashort optical pulses and arbitrary waveform is highly importance in many research areas, such as high speed optical communications, optical signal processing, and bio-photonics.

However, current electronic techniques of signal manipulation are far advanced compared to all-optical processing devices. One of the key features of electronics is the capability of generating electrical waveform in temporal domain with arbitrary shape for a variety of integrated circuits applications.

Pulse shaping in optical domain has been implemented in optical domain using devices such as Liquid Crystal Spatial Light Modulator, wavelength to time mapping, acousto-optic modulators, and electro-optical phase arrays, which allow arbitrary spectral intensity and phase to impart on the pulses. [36]

2.2 Applications of Parabolic Pulse in Signal Processing

Applications of parabolic pulses have not been limited to ultrashort high power pulse generation and highly coherent continuum sources, but also optical processing techniques that utilized their unique features. These include, but not limited to optical regeneration including pulse re-timing, pre-receiver nonlinear processing in the optical domain, and mitigation of linear waveform distortions. Moreover, the simplicity of the intensity profile of parabolic pulse makes it desirable to a range of applications, such as time-domain add-drop multiplexing, wavelength conversion, time to frequency mapping of multiplexed signals, as well as enhanced spectral compression.

2.3 Active Pulse Shaping Techniques Overview

2.3.1 Pulse Shaping in the Frequency Domain

Due to their short duration, ultrafast laser pulses with time durations in the ps or shorter, cannot be directly shaped in the time domain. One way to realize a pulse shaper is the Fourier transform wave shaper, which uses a spatial light modulator (SLM) as a mask. Its operation principle is based on the optical Fourier transformation (OFT) between the time and frequency domains [37]. The schematic of a standard pulse shaper design is shown in Figure 2-1.

An incoming ultrashort laser pulse is dispersed using a grating and the light is collected by a lens of focal length *f*. The spectral components of the original pulse are separated at the

back focal plane of the lens, which is called the Fourier plane. By this means, the intensity and phase of spectral components can be individually accessed by placing a SLM at the system Fourier plane. The pulses are reconstructed by performing an inverse Fourier transformation back into the time domain by a mirrored setup consisting of an identical lens and grating. Pulse shaping is performed by modulating the incident spectral electric field E(ω) by a (linear) mask having a spectral transfer function M(ω). This results in a spectral electric field E(ω) given by:

$$E_{out}(\omega) = M(\omega)E_{in}(\omega) \tag{2.1}$$

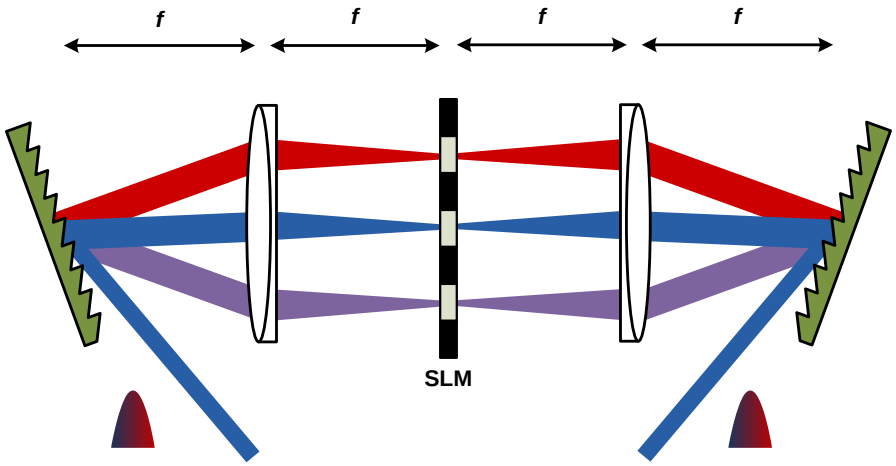

Figure 2-1: Conceptual schematic of pulse shaper in frequency domain based on optical Fourier transformation (OFT). This designed is called "zero dispersion pulse compressor" using a pulse shaper mask. The mask is designed to modulate spectral content of the input pulse to match the requirement of output pulse. A programable spatial light modulator (SLM) can be used in the place of the mask to control spectral phase and intensity of the pulse, instead of a costly dual phase-intensity mask.

The mask can be used to modulate either the spectral amplitude A(ω), or the phase Δφ.

$$M(\omega) = A(\omega)\exp\left(i\Delta\varphi(\omega)\right) \tag{2.2}$$

2.3.2 Pulse Shaping in the Temporal Domain

In this approach, the near transform limited pulses generated by a Mode-Locked Laser (MLL) are dispersed. That can be done using a Chirped Fiber Bragg Grating (CFBG) or simply a fiber spool. The time profile of the dispersed pulses will match the optical spectrum of the laser, due to frequency-to-time mapping resulting from the linear chirp. Let us assume a Gaussian optical spectrum for the rest of the discussion, without loss of generality. The purpose of the rest of the setup is to convert the pulse shape from Gaussian to parabolic. Concurrently, it is advantageous to clip the tails of the Gaussian pulse using a passive optical band pass filter, which creates sharp edges on the pulse. Subsequently, there are two different ways that can result into the parabolic pulse shape;

a) The pulses are converted to square using a feedforward system [38] and then the parabolic shape is attained using an Mach-Zehnder interefometric switch biased at the appropriate point and driven by a ramped RF signal. This approach has the advantage of being dynamic and is able to deal with changes in the pulse shape and the optical spectrum. The schematic of this approach is shown in Figure 2-2

b) In the second approach, as illustrated in Figure 2-3, a simple amplitude modulator is used, where the driving electrical signal is quasi-static and has to be calculated to incorporate the optical spectral shape, the modulator's nonlinear response and the desired (parabolic) pulse shape. This is the approach we chose in this paper to produce parabolic intensity profile pulse.

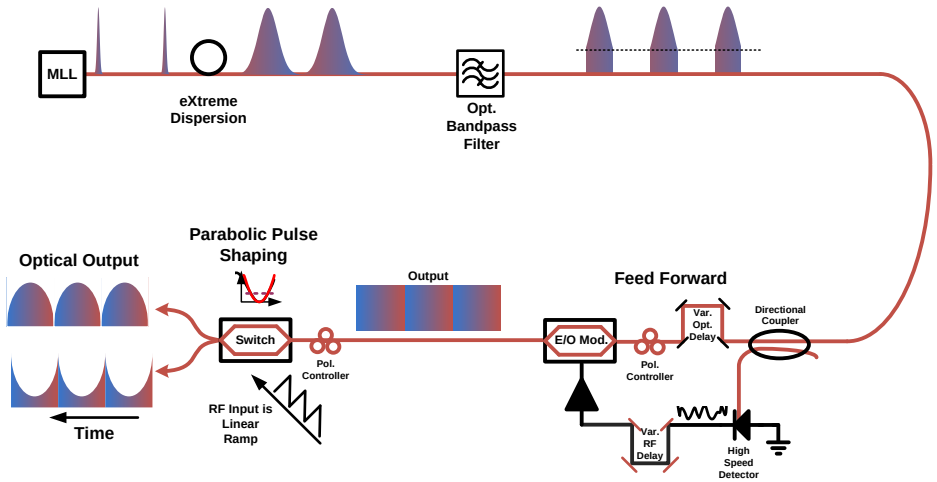

Figure 2-2: The schematic of pulse shaper in temporal domain utilizing a feedforward mechanism. Pulses from a MLL are stretched with an optical pulse stretcher before being sent to an optical bandpass filter to create sharp edges of the pulses. The feedforward mechanism helps flatten the pulses, producing output pusles with squarish optical spectrum. These pulses travels through an optical switch, where an RF ramp signal is applied to the switch, shaping the output pulses into parabola. Due to frequency-to-time mapping, the temporal spectrum also assumes the parabolic shape.

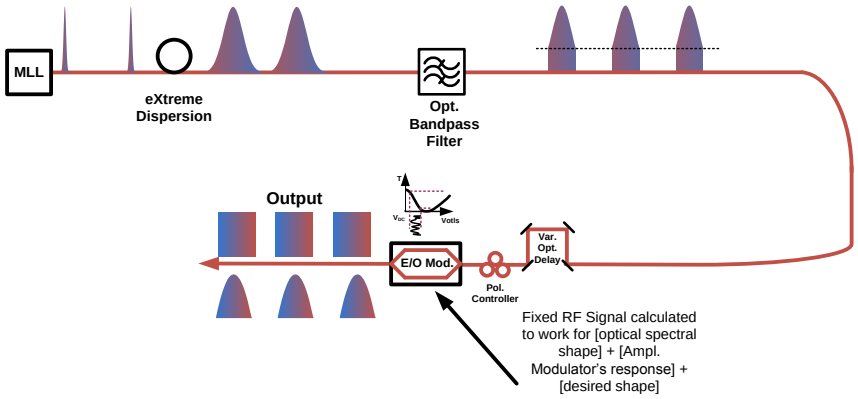

Figure 2-3: Diagram of pulse shaper in temporal domain using an intensity modulator. The quality of the output pulses depends on the availability of the RF bandwidth of the intensity modulator, the electrical signal driving the modulator, the compexity of the intensity profile of input pulses, and the amount of stretching associated with the optical pulse stretcher.

2.4 Passive Pulse Shaping Techniques

2.4.1 Pulse Shaping using Normal Dispersion Fibers

Normal dispersion fibers with dispersion carefully calculated and designed and engineered to achieve parabolic pulse shaping. One of the earlier works in parabolic pulse generation was the theoretical demonstration of self-similar propagation of short pulses of parabolic intensity profile in optical fibers with normal group-velocity dispersion (GVD) and strong nonlinearity [39]. This concept has also been extended to optical fiber amplifiers. By use of the technique of symmetry reduction, parabolic pulses were shown to propagate self-similarly in a normal dispersion rare earth doped fiber amplifier, and verified experimentally [29,40–42]. Most of the effort has been on generating parabolic pulses in fiber amplifier with normal

dispersion [26,28,43], in which pulse propagates in normally dispersive and nonlinear fiber amplifiers, taking advantage of the asymptotic reshaping that occurs during that process [29,32,39]. There are a number of experimental demonstrations of parabolic pulse generation, focusing on amplification from rare earth doping [29], Raman amplification in standard optical fibers [27], and utilizing active or passive dispersion decreasing optical fibers [28]. Pulse shaping using optical fiber that exhibits a decrease in the absolute dispersion along its length has also been reported [25,26,30]. This approach is based on the observation that the longitudinal decrease of the normal dispersion is equivalent to optical gain [25]. Passive pulse shaping using super structured fiber Bragg gratings [44], a combination of two carefully chosen normally dispersive optical fibers [28], or continuously tapered dispersion decreasing fiber has also been successfully demonstrated [30,45]. Pulse shaping techniques that control amplitude and phase of input pulses have also been investigated, and have significantly improved the performance of CPA system [28,45,46].

Passive pulse shaping techniques only generate parabolic pulses with moderate quality, since the input pulses evolve asymptotically into a near parabolic shape. As the pulses propagate, even though they retain their quasi-parabolic shape, their width and amplitude evolve. Thus, there is no mechanism to actively and dynamically control the pulse characteristics. Also, it has been shown that third order dispersion and linear absorption also have detrimental effects on parabolic pulse evolution and thus on the performance of configurations utilizing dispersion decreasing fiber [33].

2.4.2 Algorithms for Fiber Dispersion Calculation

2.4.2.1 **Genetic/Annealing Algorithms**

Genetic algorithms are Monte Carlo based algorithms. Monte Carlo algorithms use probability to determine the global optimum. In the case of a generic genetic algorithm, the total number of variables forms an array. Each variable represents a gene, and the total array of values represents an individual in the population. Each individual corresponds to a location within the overall solution-space, as shown in Figure 2-4. Thus, individuals with better "fitness" contain values within their genes that are better optimized than individuals with lower fitness. In principle, the algorithm starts with a random selection of individuals whose genes broadly represent the total volume of possible solutions. The individuals are then tested for fitness (e.g. the random sets of variables are tested against some pre-determined condition) and those with the highest fitness are allowed to move to the next generation. These fit individuals will also create offspring by randomly swapping genes with other "fit" individuals. This random recombining of genes creates new individuals who are then also tested for fitness. In theory, the algorithm will move toward the global optima, avoiding local optima through breeding. Given enough time and individuals the algorithm will find the global optimum. The larger the population, the fewer generations it takes to reach the optimum. Because of the large number of individuals, this algorithm works best when multiple individuals can be checked for fitness concurrently, thus maximizing throughput. When throughput is limited, the large number of random samples which lead to unfit individuals can become cumbersome. Since theory predicts that initially there will be many more unfit individuals than fit ones, early generations often move a large

portion of poorly fit individuals on to the next generation. While this provides for a healthy population in that there is a large random sampling of the solution-space, it also results in a large number of unnecessary calculations.

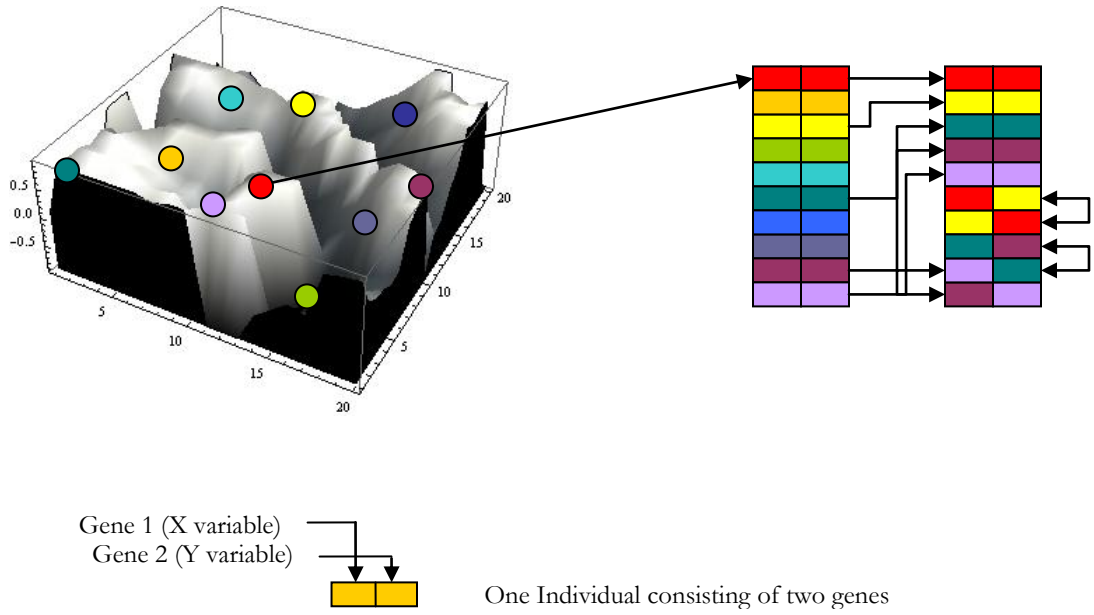

Figure 2-4: A 2-dimensional example of a genetic algorithm. An individual is made of genes containing an array of variables. The most optimal of individuals (largest z-axis values) randomly cross genes in order to create new individuals which are then tested against the environment.

Simulated annealing, like other probabilistic metaheuristics, economically finds a good approximation of the global optimum given a high dimensionality. This method varies from other Monte Carlo-based methods in that it avoids local optima by being less greedy. Greed is

defined as the degree in which an algorithm limits successful moves to only beneficial moves. A greedy function would reject all moves with lower optimization and only accept those moves which result in a better state than the current one. The problem with this is the ease in which such a function can get trapped in local optima. Simulated annealing randomly probes the field-space by starting with a limited number of samples, often one. This individual proceeds through a random walk in which a step of predetermine-size is taken in a random direction (one variable is changed a fixed amount each iteration). If the new position is better, the solution is kept. If it is worse, a probability function determines if the position is kept or if the individual returns to the previous location. This probability of staying at a bad location is determined through the drawing of a random number. If the random number, the samples "temperature", is below the "environmental temperature", the move is kept. As the system proceeds, the environmental temperature decreases, reducing the likelihood that the sample will stay at a worse location than its previous location. The system thus progresses toward a lower energy system with an ever-decreasing likelihood of moving out of its current minima/maxima. The movements continue until either a preset number of iterations is reached, or an acceptable solution is found. A modification of this process combines quantum annealing (decreasing step length with a static acceptance rate) with simulated annealing to create adaptive simulated annealing.

The methods described above give a sampling of the possibilities in optimization algorithms currently used in the field of iterative computational optimization. Because of the immensity of the field of metaheuristics, further investigations into optimization algorithms will continue.

2.4.2.2 **Backward Propagation using Split Step Fourier Method (SSFM)**

The propagation of optical pulses in nonlinear dispersive fibers has been mathematically derived, which uses the electromagnetic wave equation as a starting point. The effects of fiber losses, dispersion and fiber non-linearities can also be accounted for in the wave equation to show the evolution of the pulse shape as it propagates over a length of optical fiber.

Different numerical methods are available for solving the wave equation. One such method called the split step Fourier method has been used extensively to solve pulse propagation problems in nonlinear dispersive mediaThe Split Step Fourier method for pulse propagation is used to solve the pulse propagation problem in nonlinear, dispersive media, by dividing the propagation distance into small step [14]. This equation is called Nonlinear Schrodinger equation (NLSE) , which describe the temporal and longitudinal dependency of the slowly varying pulse envelope A(z,t) long the fiber in the retarded time frame t

$$\frac{\partial A}{\partial z} = \left(\widehat{D} + \widehat{N}\right)A \tag{2.3}$$

Where A is the complex electric field, $\widehat{D} = \frac{1}{2}(j\beta_2 \, {\partial^2}/{\partial t^2} + \alpha)$ is the differential operator accounting for fiber dispersion and loss, and $\widehat{N} = j\gamma A^2$ is the nonlinear operator. α is the attenuation factor, β_n are the Taylor expansion coefficient of dispersion parameter, in this particular case β_2 is the group velocity dispersion, and γ is the effective nonlinearity coefficient, respectively. The pulse amplitude A(z,t) is assumed to be normalized such as $|A|^2$ represents the

optical power. The nonlinear coefficient γ is defined by $\gamma = \frac{n_2 \omega_0}{c A_{eff}}$ where A_{eff} is the effective mode area, n_2 is the nonlinear refractive index coefficient, c is the speed of light $3x10^8$m/sec, and ω_o is the center frequency of the optical field. These parameters therefore represent the linear effects of dispersion, gain/loss and self-phase modulation as the lowest-order nonlinear effect.

The phase excursion imposed by the SPM can lead to nonlinear chirp, which cannot be compensated by standard dispersive element. Another important parameter, the accumulate nonlinear phase of a pulse propagating through the fiber, called B-integral is defined as

$$B = \frac{2\pi}{\lambda} \int_0^L n_2 I(z)\, dz \tag{2.4}$$

Where I(z) is the intensity of pulse propagating over the fiber length L. The B-integral is considered as linear propagation when smaller than 1. When B-integral exceeds that value, the propagation is considered nonlinear, and pulse quality is consequently degraded.

To illustrate the consequence of SPM, the demonstration of this technique is shown in Figure 2-5, with input pulse assumes Gaussian shape during propagation, and as pulse propagates along 15m of fiber, side bands are created. For this particular simulation, only nonlinear and dispersion parameters are non-zero.

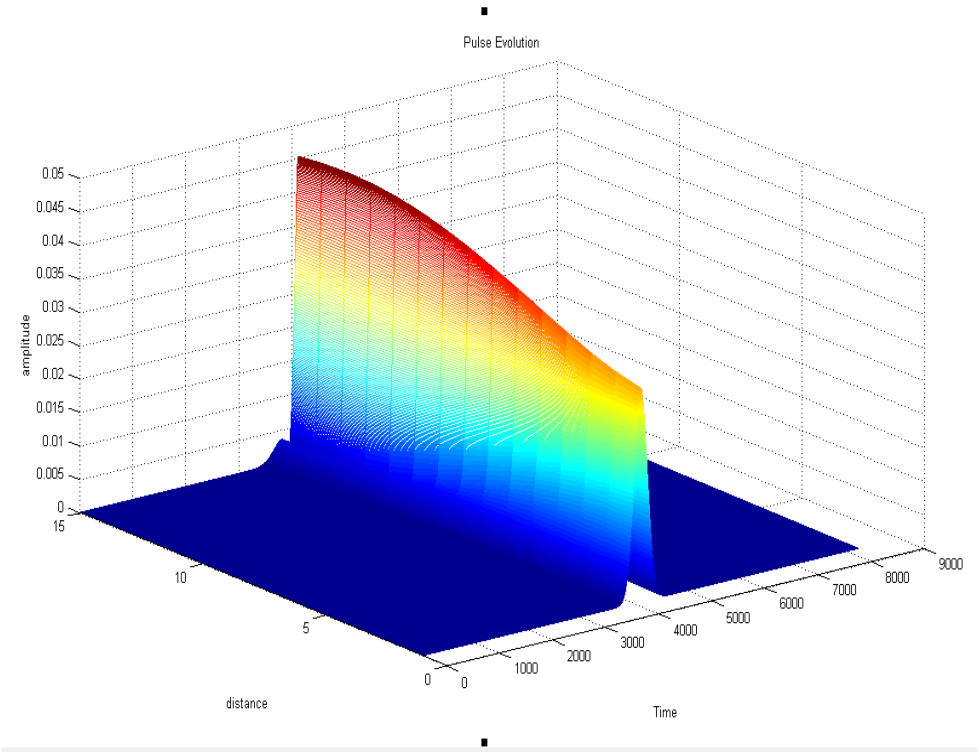

Figure 2-5: Pulse propagation in fiber using Split Step Method. Input pulse has a Gaussian shape with full width half maximum temporal duration of 1 ps. Pulse travels through 15 m of fiber with high dispersion slope.

The modelling result indicates pulse broadening due to SPM, and sidelobes appears. These sidelobes contain a significant amount of pulse energy, and therefore reducing peak power of pulse after propagation. The simulation was performed with pulse propagation in only 15 m of fiber, and still a significant pulse distortion was observed, with negative effects such as reduction of peak power and degradation of pulse contrast. This simulation is essential in the estimation of dispersion required in engineering fiber properties for self-similar pulse propagation.

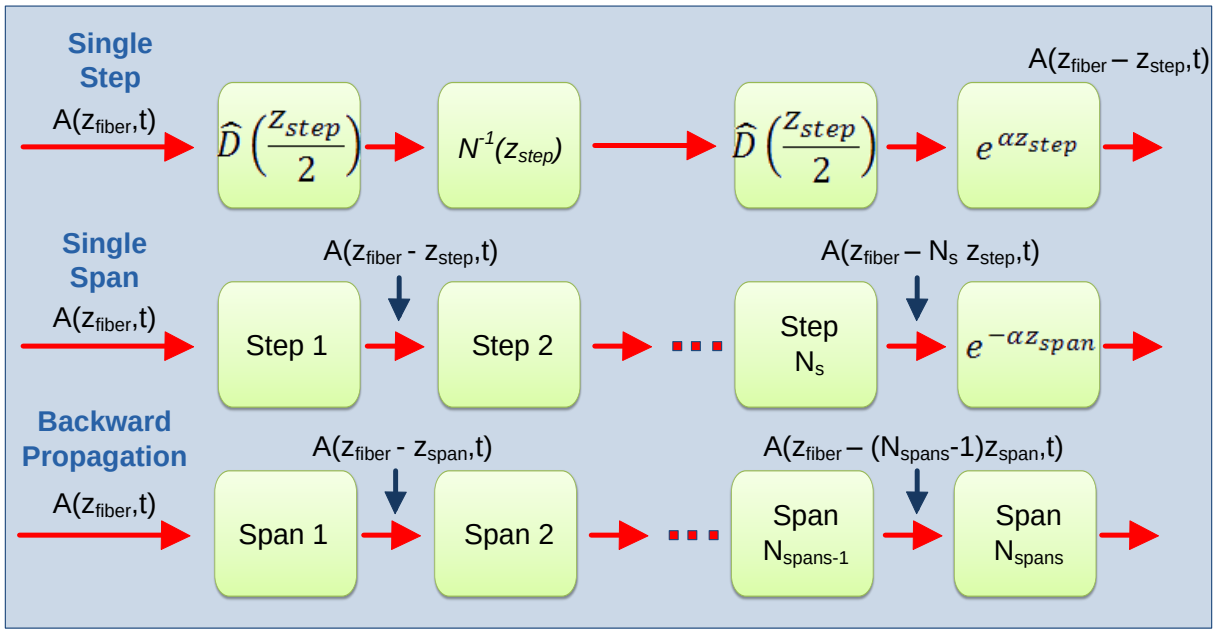

Figure 2-6: Block diagram of backward propagation in fiber using Split Step Fourier Method.

For backward propagation, the optical pulse power and intensity profile of the desired output pulses from the system is backward propagated utilizing the split step Fourier method [14,47]. By knowing the desired output pulse from CPA system, using backward propagation technique, we can predict the optical properties of the required input pulse, which will be generated by the Finisar spectral processor. Backward propagation using the single step Fourier method can be employed by dividing the total propagation distance into smaller spans, with each span consisting of many smaller steps (Figure 2-6). Within a step, the effect of nonlinearity is included at the midplane. Half of the dispersion is accounted for before the midplane, and the other half after the midplane. Fiber loss is accounted for in each step while amplification is reversed after each span. Compensation for the entire propagation length is achieved by

repeating these steps. By selecting a step size that is small enough, the evolution of the optical pulse as it backward propagates through a system can be obtained.

To obtain optical pulses with high power, linear chirp and parabolic intensity profiles from our CPA system, the optical pulse power and intensity profile of the desired output pulses from the system is backward propagated using the split step Fourier method. System nonlinearities and dispersion effects are included in the simulation to obtain the required power and intensity profile of the input pulse. Therefore, if an input optical pulse with the characteristics predicted by the simulation is launched into the CPA system, it will result in good quality, high power, linearly chirped pulses that can be compressed easily using a grating compressor to result in high peak powers.

CHAPTER 3: TIME DOMAIN OPTICAL FOURIER TRANSFORMATION PULSE SHAPING

3.1 Introduction

Chirped pulse amplification (CPA) has been widely used to achieve pulses with high energy for many applications such as radar technology or non-thermal ablation [6,48–51]. Increased energy per pulse can be extracted from gain media if the pulse is chirped and temporally stretched to a pulse duration longer than the storage time of the gain media [23,24]. However, in fiberized systems, when desired energy levels are in the miliJoule range, pulse amplification is limited because nonlinearities and dispersion of the gain media can cause severe pulse distortion and consequently degrade the pulse quality. As a result, advanced measures are required to mitigate the effect of nonlinearities and dispersion. Pulse shaping techniques that control amplitude and phase of input pulses have been investigated, and have significantly improved the performance of CPA systems [10,46,52].

Optical pulses, whose temporal shape is parabolic, appear to be a very suitable candidate for reducing the impact of nonlinearities and to achieve high peak powers [46]. The use of parabolic pulses for fiber CPA has attracted considerable attention due to their ability to retain their intensity profile during propagation in highly nonlinear and dispersive media [32,39,41,46]. Self-phase modulation, which is proportional to the temporal intensity of the pulse, induces a linear frequency chirp during amplification of parabolic pulses. The linear chirp also allows efficient pulse compression, therefore making parabolic pulses especially

suitable for use in a wide range of applications, such as high power femtosecond lasers, super-continuum generation for optical telecommunications, fiber amplifiers and chirped pulse amplification [29,44].

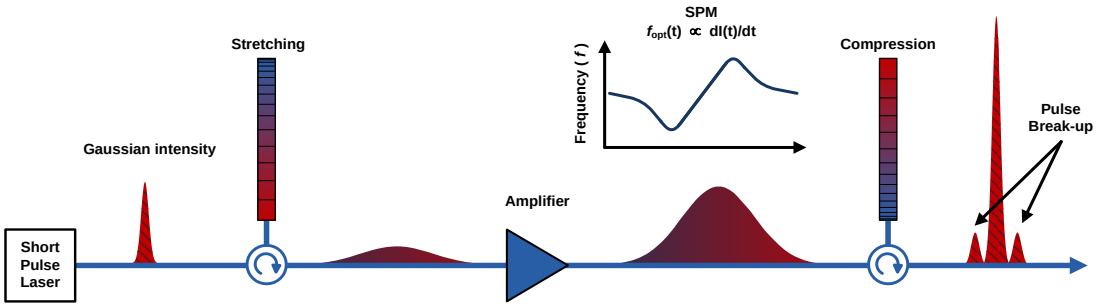

Figure 3-1: Non linear effects on pulses with different input intensity profile; with Gaussian temporal intensity profile.

Several different approaches for parabolic pulse generation have been demonstrated. One of the earlier investigations in parabolic pulse generation was the theoretical demonstration of self-similar propagation of short pulses of parabolic intensity profile in optical fibers with normal group-velocity dispersion (GVD) and strong nonlinearity [39]. This concept has also been extended to optical fiber amplifiers, taking advantage of the asymptotic reshaping which occurs upon propagation within fiber amplifiers. By using the symmetry reduction technique, parabolic pulses were shown to propagate self-similarly in a normal dispersion rare earth doped fiber amplifier [29,40,41]. Since then, much work has been done to generate parabolic pulses using dispersion-decreasing fiber (DDF) with normal group velocity dispersion [25,26], Raman amplification in optical fibers [27], and active or passive dispersion decreasing optical

fibers [28]. Further investigations to passively generate parabolic pulses using tapered dispersion-decreasing fibers have also been reported [30,45].

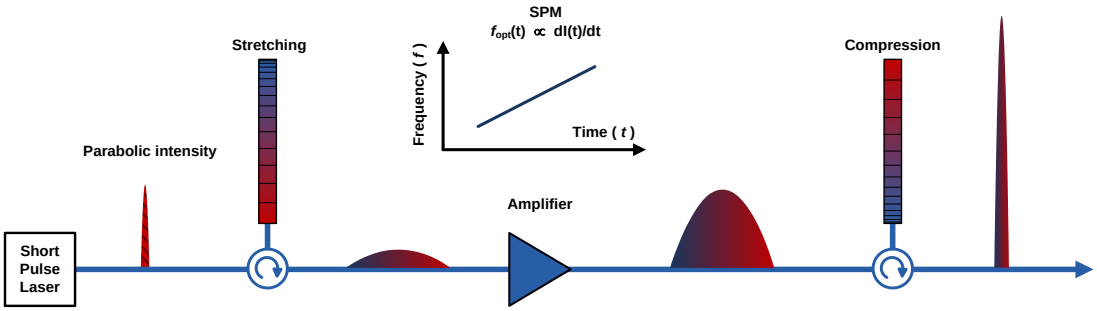

Figure 3-2: Non linear effects on pulses with different input intensity profile; with parabolic temporal intensity profile.

The quality of the parabolic pulses generated with these approaches is only moderate, because the input pulses evolve asymptotically into a near parabolic shape. Also, as the pulses propagate, even as they retain their parabolic shape, their width and amplitude change, so there is not a well-defined mechanism to actively and dynamically control pulse characteristics. Also, it has been shown that third order dispersion and linear absorption have detrimental effects on parabolic pulse evolution and thus, on the performance of configurations utilizing DDF [33].

In this chapter, a dynamic temporal pulse shaping technique of time domain optical Fourier transformation (OFT) technique is explored. Time domain OFT is the technique in which the spectral profile is converted into a waveform in the time domain, enabling the elimination of undesirable waveform distortion caused by linear perturbation in optical fibers, such as high

order dispersion, jitter, and polarization mode dispersion [36] (Boscolo p9, 2012). Optical pulses from a mode-locked laser are temporally stretched to a temporal duration of several nanoseconds. An intensity modulator is driven with an appropriate voltage signal to shape the input pulses into parabolic temporal profiles. This technique to generate a parabolic temporal intensity profile as well as dynamically control properties of the output pulse with any input pulse profile is demonstrated experimentally.

3.2 Experimental Setup

3.2.1 Frequency selection down of seed pulse train

The pulse train from the Calmar mode-locked laser is sent to an acousto-optic modulator. The AOM is used to frequency-select the repetition rate of the pulse train from 20 MHz down to 1.25 MHz as described previously. Figure 3-3(a) is the 20 MHz fundamental frequency of Calmar laser, as seen on RF spectrum analyzer, and Figure 3-3 (b) is the power spectrum after frequency-selection down, with the repetition rate of 1.25 MHz.

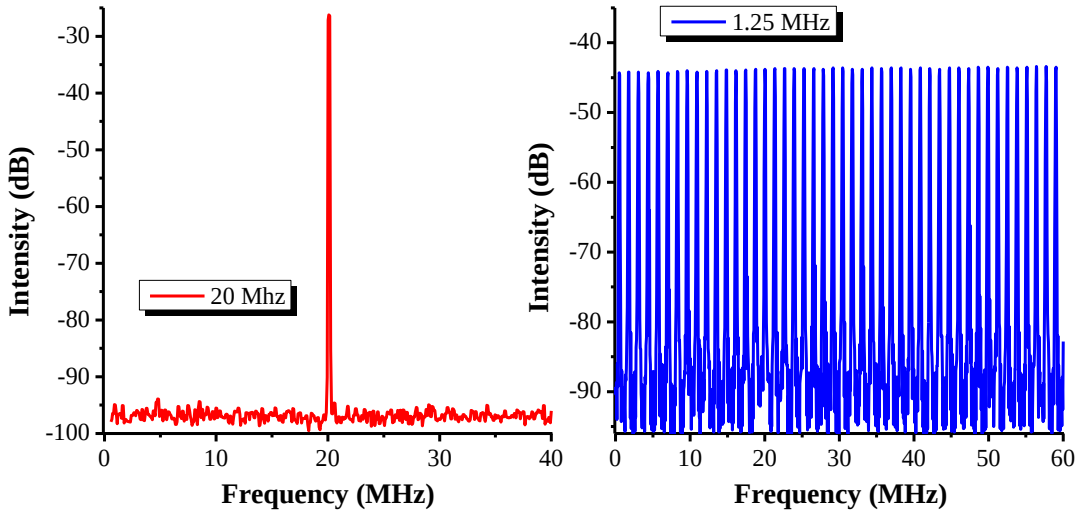

Figure 3-3: Photo-detected power spectrum of Calmar laser before and after frequency-selection, recorded with a RF spectrum analyzer (RFSA). An RF frequency divider was used to generate an RF trigger signal to the AWG, with the repetition rate of the triggering signal equals to the desired repetition rate of output laser pulse train. Due to the limitation of AWG, which can't respond to triggering signals with repetition rate higher than 2.5 MHz, the experiment was performed at frequency selection down set to 1.25 MHz, which is 8-fold slower than the 20 MHz repetition rate of the pulse train of the seed laser.

3.2.2 Parabolic pulse shaping employing $LiNbO_3$ intensity modulator

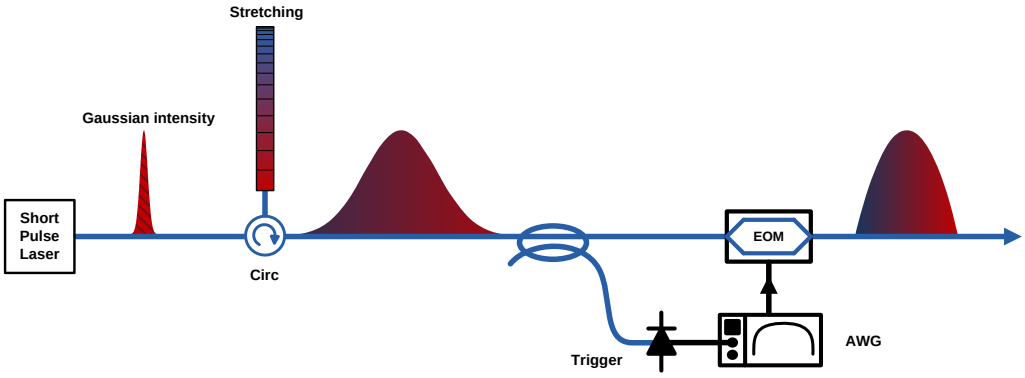

Figure 3-4: Experimental setup for pulse shaping. Cir: circulator, PD: Photodiode, EOM: intensity modulator, AWG: arbitrary waveform generator. The intensity profile of the input pulse is chosen to be the well-known Gaussian shape. After pulse stretching, due to frequency-to-time mapping, the stretched pulse also assume Gaussian shape. The temporal duration of the stretched pulse has to be sufficiently long with respect to the bandwidth of the intensity modulator for the scheme to work.

The schematic for temporal pulse shaping is shown in Figure 3-4. The near transform limited pulses generated by a mode-locked laser (MLL) are temporally stretched using dispersion-compensating fiber (DCF). Due to the high dispersion experienced by the pulses in the DCF, a wavelength-to-time mapping of the temporally stretched pulses is observed, so the temporal profile of the dispersed pulses closely resembles the shape of the input optical spectrum [53]. Subsequently, the stretched pulses are sent into an intensity modulator. A broad bandwidth arbitrary waveform generator (AWG) is used to generate a voltage drive signal. This

drive signal is applied to the intensity modulator and is synchronized with the arrival of the stretched pulses, to impart a parabolic intensity profile to the stretched pulses.

To synchronize the voltage signals generated by the AWG with the incident optical pulses, pulses from the same mode-locked laser are photo-detected, and used to trigger the AWG. Since the quality of the shaped pulses directly depends on the quality of the voltage drive signal, an AWG with a sufficiently large bandwidth and high temporal resolution is required to generate a high quality drive signal. The AWG used in the experiment has a sampling rate of 10 GSamples/sec and a bandwidth of 10 GHz. After shaping, the parabolic pulses are photo-detected, and a sampling oscilloscope is used to monitor the quality of the pulses.

The typical transmission function of an intensity modulator is given by the equation

$$T(V) = \sin^2\left(\frac{\pi \cdot V}{2 \cdot V_\pi}\right) \tag{3.1}$$

where V is the applied voltage and V_π is the voltage at which the transmission of light through modulator changes from minimum to maximum. For a known intensity profile of an input pulse $I(t)_{input}$, the response function in time P(t) of the intensity modulator required to generate a parabolic pulse can be calculated by:

$$P(t) = \frac{I_{output}(t)}{I_{input}(t)} \tag{3.2}$$

where $I(t)_{output}$ is the desired output parabolic intensity profile.

From (1) and (2), the required drive voltage signal can be obtained by:

$$V(t) = \arcsin\left(\sqrt{P(t)}\right) \cdot 2\frac{V_{\pi}}{\pi} \tag{3.3}$$

The important aspect of this approach is that it allows dynamic control of the properties of the output pulses such as pulse shape, pulse width, and amplitude, and can be configured to work with input pulses with any intensity profile.

3.3 Results and Discussion

Two different types of configurations were used in this work: a CW laser which simulates a square pulse input to the system and a MLL with Gaussian-shaped pulses. As a proof of concept experiment, a temporally gated CW laser is used as a seed source to simulate a square pulse input to the system, as can be seen in Figure 3-5. It should be noted that the square pulses

with linear chirp and uniform intensity can be produced with the frequency swept mode-locked laser [54].

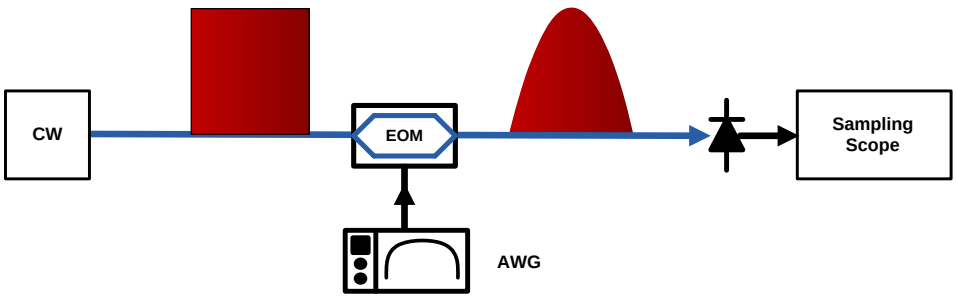

Figure 3-5: Time domain parabolic pulse creation using a CW laser source. The period and duration of the output signal is determined by the period and duration of the electronic signal generated with the AWG. The resolution of the electronic signal is limited by the bandwidth of the AWG, which is 10 GHz, or 0.1 ns.

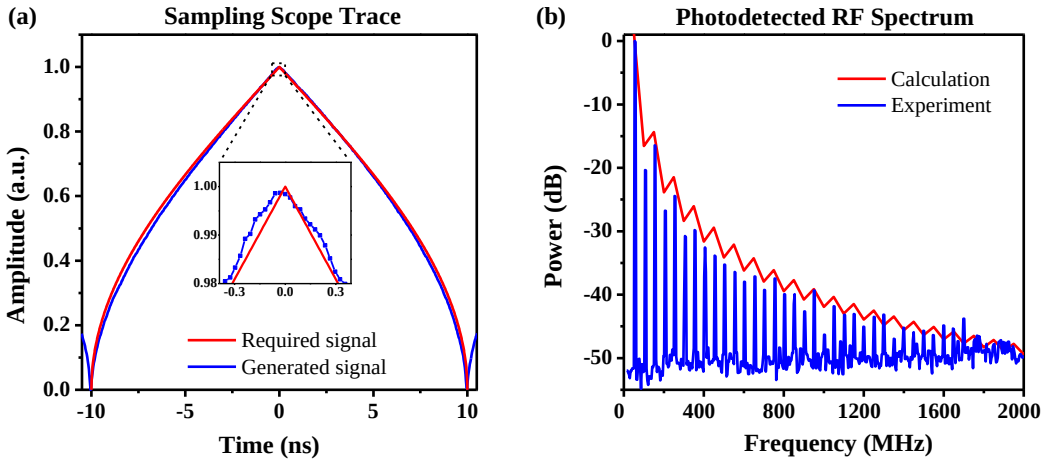

Figure 3-6: (a) Required and generated drive signal for square input pulses; inset: zoom-in of the peak. The required and genertd drive signals sufficiently resemble each other, with the difference resulting from the limitation in resolution and bandwidth of the AWG (b) Experimental and calculated power spectrum of drive signal, with the calculated power spectrum follows the contour of the measured power spectrum of the drive signal very well

Using the procedure described in section 2, the voltage drive signal is calculated and plotted in Figure 3-6(a). It's evident that the drive signal (blue) generated by the AWG (Figure 3-6 (a)) matches very well with the required signal (red). The power spectrum of this signal is shown in Figure 3-6 (b), where the calculated power spectrum agrees with the measured spectrum up to 1.5 GHz. In this figure, the required power spectrum (red) is the envelope of the desired signal, because it is calculated from a non-periodic drive signal, unlike the measured power spectrum of periodic signals generated by the AWG (blue). The signal generated by the AWG is used to drive the modulator, resulting in parabolic pulses, plotted on a logarithmic scale in Figure 3-7(a).

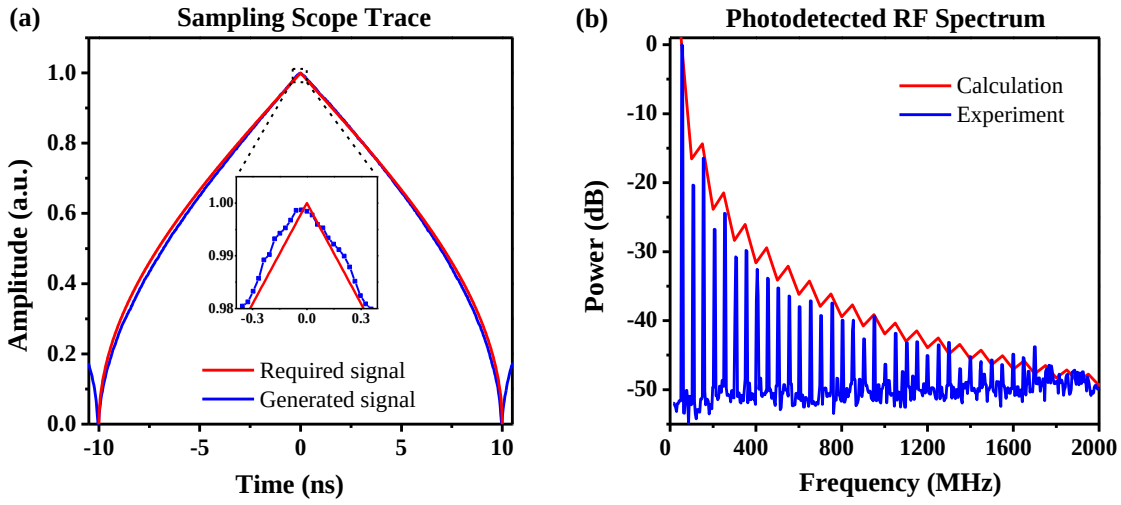

Figure 3-7: (a) Parabolic intensity profile of pulse after intensity modulation (b) Residual error after pulse shaping, compared with a perfect parabola.

Notice that in Figure 3-7 (a), the pulse edges fall sharply following the parabolic fit, with an observed extinction ratio of 30 dB. To further demonstrate the precision of the generated parabola, the residual error over the full temporal duration of the pulse of 20 ns is calculated, by taking the difference of this parabolic pulse with the fitted parabola, and is shown to be less than 3%, as seen in Figure 3-7 (b).

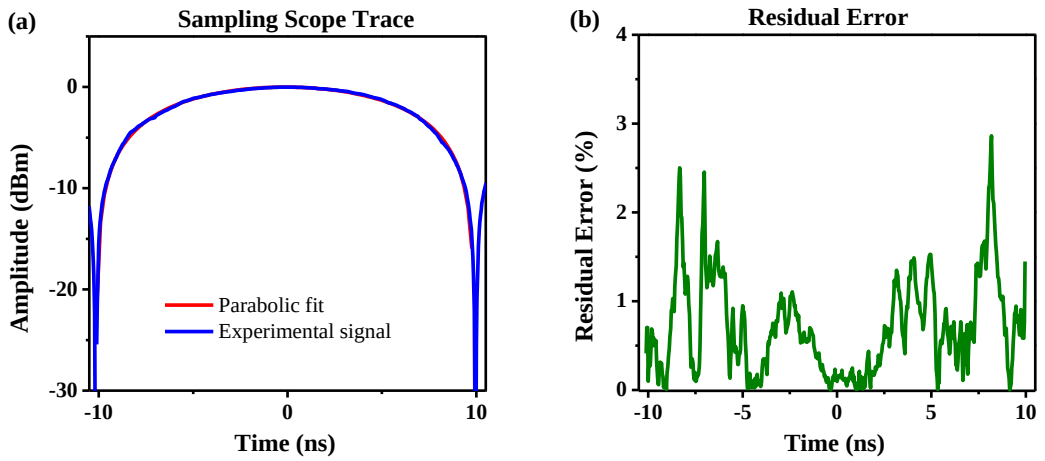

Figure 3-8: (a) Time-domain picture of output parabolic pulses as recorded with sampling scope (b) Residual error of generated parabolic pulses compared to a perfect parabola.

In the second experiment, near transform limited pulses generated from a MLL are temporally stretched using 10 km of DCF. The shape of the optical spectrum is approximated by a Gaussian function with a full width at half maximum (FWHM) bandwidth of 6.6 nm, with a center wavelength at 1556 nm and a repetition rate of ~2.45 MHz. Pulses passing through the DCF are temporally stretched and spectrally dispersed, with the temporal profile of the dispersed pulses closely resembling the Gaussian shape of the optical spectrum. The DCF has a dispersion of ~1350 ps/nm which induces a linear frequency chirp and temporally stretches the pulses to 8.9 ns duration (FWHM): $\Delta t = D \cdot \Delta\omega$, where Δt is the pulse duration at FWHM, D is the dispersion of the DCF, and $\Delta\omega$ is the optical bandwidth (FWHM).

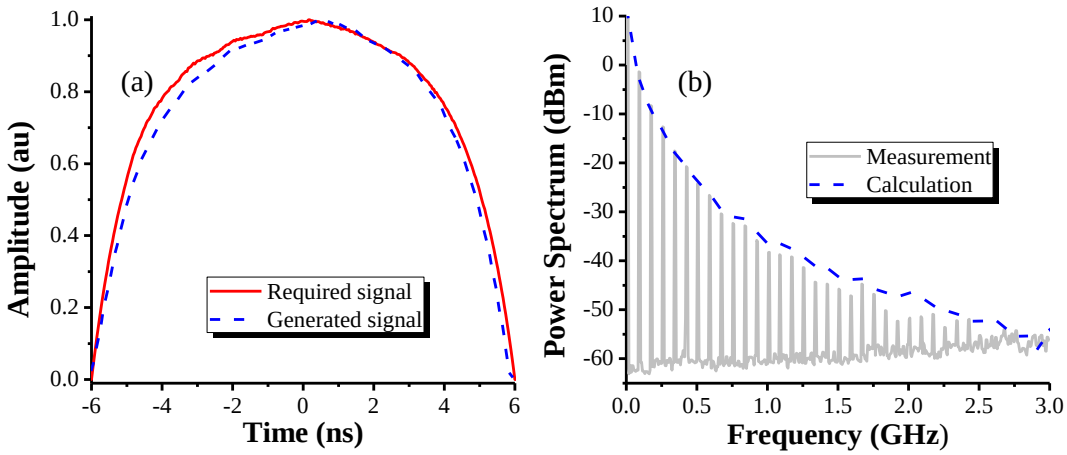

Figure 3-9: (a) Drive signal for parabolic input pulse, with temporal duration of approximately 12 ns (b) Experimental and calculated power spectrum of drive signal. The calculated power spectrum (b-dashed) shows very good agreement with the measured spectrum up to approximately 3 GHz, with more deviation toward the higher frequency. The comb spacing of RF tones corresponds to the temporal width of the drive signal.

Stretched pulses with longer temporal durations allow higher resolution shaping, due to the fixed temporal resolution of the AWG. The pulse train is then directed to an intensity modulator that is driven by an appropriate voltage signal, to produce pulses with parabolic intensity profiles. Figure 3-9 (a) shows the calculated drive signal, with a temporal duration of ~12 ns. The small discrepancies between the generated signal and the required signal are due to the bandwidth limitation of the AWG. The generated power spectrum of this drive signal can be seen in Figure 3-9 (b) and is found to be in agreement with the calculated power spectrum up to 1.75 GHz in bandwidth.

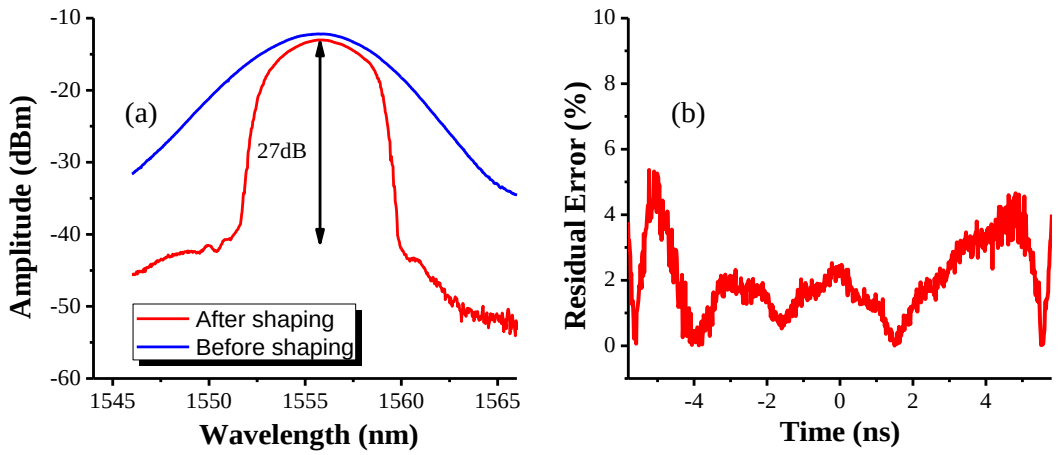

Figure 3-10: (a) Optical spectrum of pulse before and after pulse shaping (b) Calculated residual error of generated parabolic pulses compared to a perfect parabola. The maximum deviation is approximately 5% at the wings, and smallest at the center, approximately 2%, with overall rms deviation is about 2.5%.

The drive signal is applied to the intensity modulator and is synchronized with the arrival of the stretched pulses, resulting in parabolic pulses. Figure 3-10(a) shows the optical spectrum before and after pulse shaping, and an extinction ratio of 27 dB is observed. A close observation of Figure 3-10(a) reveals that the optical power at the wings of the input pulse is attenuated to create parabolic shape at output pulse. The amplitude of pulses before and after pulse shaping has been adjusted for easy comparison. Figure 3-10 (b) shows a residual error of less than ~5% over the pulse duration of 12 ns.

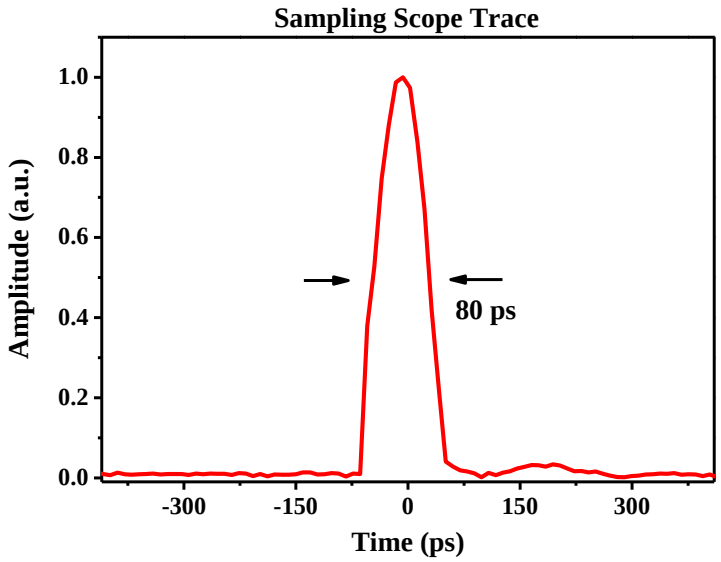

Figure 3-11: Time-domain picture of pulses as seen on sampling oscilloscope after pulse shaping and compressing. Notice the sharp edge of the trace, which indicate parabolic pulse shaping helps reduce nonlinearity induced-pedestals. The compression was limited to 80 ps to preserve quality of the pulse and limit the presence of temporal pedestal and pulse breaking, with detrimental effects on pulse shape.

To demonstrate the compressibility of the pulses after the temporal shaping, pulses are compressed to achieve high peak power using a commercially available chirped fiber Bragg grating (CFBG). The parabolic pulses having a 8 ns temporal duration (FWHM) before compression are compressed to 80 ps, a compression factor of 100, as seen in Figure 3-11. In this experiment, the limiting factor of compression appears to be the group delay ripple of the CFBG of approximately 80 ps. Using a different CFBG with smaller group delay ripple can reduce group delay ripple effect, and produce much shorter compressed pulses [23]. It should be noted that SPM phase can complicate compression of pulse. In our experiment, the peak power –

length product is ~0.13 Wkm, which is much smaller than the 1.5 Wkm thresholds in SMF for SPM, minimizing nonlinear residual dispersion.

3.4 Conclusions

A recently conceived application, namely, time domain parabolic pulse generation is discussed in detail. In order to reduce the detrimental effects of nonlinearities that occur during pulse amplification, a dynamic temporal architecture for the generation of parabolic pulses has been proposed and demonstrated experimentally. The concept of λ-t mapping is utilized for parabolic pulse generation, enabling dynamic control of the pulse properties such as pulse shape, pulse width and amplitude. Pulse shaping using a gated CW laser input is shown, yielding parabolic pulses with less than 3% error and 30 dB signal to noise ratio. Using a mode-locked laser source, parabolic pulses with less than 5% error and 27 dB signal to noise ratio are achieved. These parabolic pulses are compressed by a factor of 100 to 80 ps, using a chirped fiber Bragg grating.

In conclusion, in the past few decades, significant progress has been made in the field of chirped pulse generation and amplification, which has enabled a wide variety of applications. In the future, further improvements in parameters such as the linearity of the chirp, the chirp bandwidth, and sweep rates will result in even better performance.

CHAPTER 4: FREQUENCY DOMAIN PULSE SHAPING

4.1 Introduction

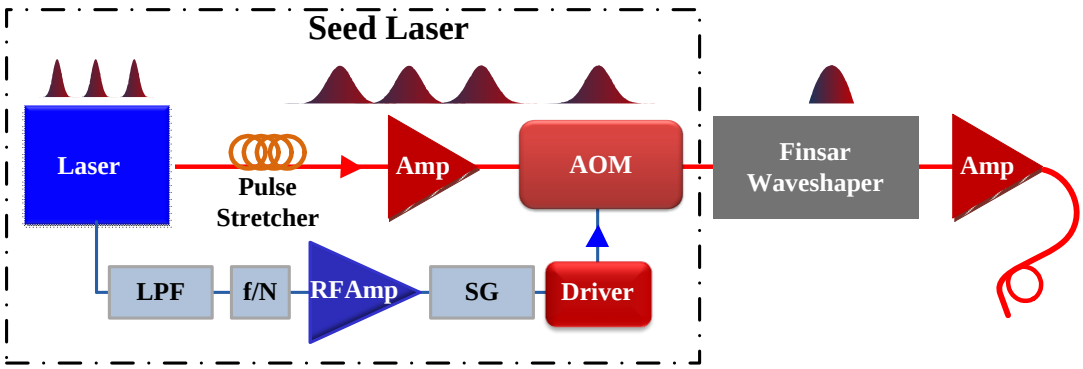

Figure 4-1: Block diagram of chirped pulse amplification setup. Amp: optical amplifier; AOM: acousto-optic modulator; Finisar: waveshaper; LPF: low pass filter; f/N: frequency divider; RFAmp: RF amplifier; SG: signal generator, Driver: AOM driver. The dash box is the seed laser for the Finisar spectral processor.

Chirped pulse amplification systems are one of the key components in telecommunication system as well as high power ultrafast sources. Optical pulses with parabolic temporal intensity profile have been shown to be especially suitable for CPA systems, due to their attractive features such as resistance to optical wave breaking, ability to retain their intensity profile during propagation in gain media, and enhanced linearity in chirp. Their linear chirp also allows efficient and high quality pulse compression. Consequently, parabolic pulse

generation has attracted much attention, with a pulse shaping approach involving a dynamic technique to control pulse intensity in the temporal domain has been reported most recently.

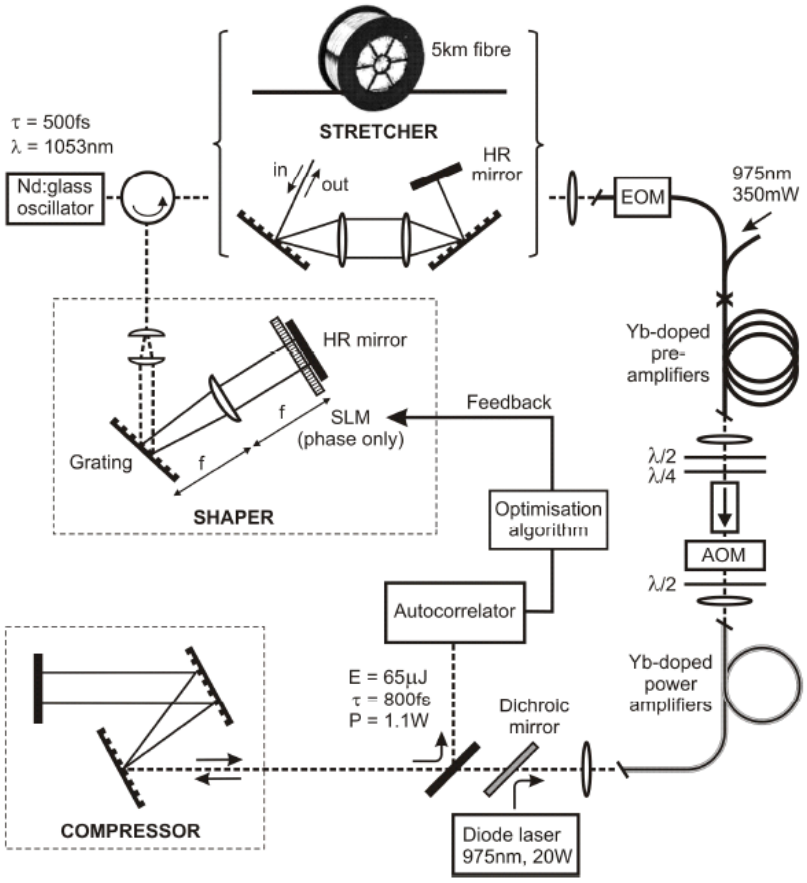

Figure 4-2: Schematic of chirped pulse amplification setup of an Yb fiber CPA system by J.H.V. Price et.al. [55]. An adaptive control loop using feedback from an autocorrelator was used to adjust the spectral phase of the input pulses. The resulting autocorrelation peak was increased by a factor of 3.4 when a fiber stretcher was employed and by a factor of 2.9 with a bulk stretcher.

It should be noted that when the desired energy levels are high, due to the combination of dispersion and nonlinear effects, even a small deviation in the temporal profile of the generated parabolic pulse from the perfect parabolic shape will result in large pedestal generation, therefore degrading pulse quality. Fiber CPA systems are particularly susceptible to this degradation effect due to their small mode areas and long interaction length.

Much research has been done to understand the mechanism of parabolic pulse generation and propagation in fiberized systems and to improve their quality. One of the earliest investigations was the demonstration of self-similar propagation of temporal parabolic pulses in optical fibers with normal group velocity dispersion and strong nonlinearity [39]. This concept has been extended to include using dispersion decreasing fiber [25], Raman amplification in optical fibers, active or passive dispersion decreasing fiber [28,43], as well as tapered dispersion decreasing fibers [45]. Pulse shaping techniques involving amplitude or phase modulation have also been explored to improve pulse quality and increase peak power of CPA systems [46,52,55,56]. Most recently, a pulse shaping approach involving a technique to dynamically control the pulse intensity in the temporal domain has been investigated [34,35].

However, pulse shaping involving both spectral phase and intensity has never been investigated. J.H.V. Price and co-worker had shown CPA system with a strong spectral modulation, resulting in 3.4-fold increase in peak power and near transform limited pulses. Phase shaping was performed to offset the broadening effect of SPM in the amplifiers as well as to compensate for the mismatched dispersion between the compressor and pulse stretcher. Spectral

phase shaping was done by optimizing Taylor coefficients of the phase profile, and the output pulses are monitored using the autocorrelator.

In this work, we proposed and demonstrated an active feedback loop, which controls both the spectral phase and amplitude of the pulses, resulting in the generation of transform-limited parabolic pulses of a CPA system operating in C-band using erbium fiber amplifier. Controlling spectral phase was essential to achieve high quality, clean, transform limited pulse, and this can be achieved by analyzing output pulse with a SHG-FROG to fully characterize pulse properties with high accuracy.

4.2 Frequency Pulse Shaping Schematic

The schematic of this approach is shown in Figure 4-3. A Calmar seed laser is used to generate pulses at 1552 nm at 20 MHz repetition rate with a full width half max (FWMH) optical bandwidth of ~7 nm. The pulses are temporally stretched using a polarization maintainig (PM) fiber stretcher with a dispersion of 100 ps/nm, resulting in a linear frequency chirp across the pulses. After stretching, pulses are amplified with a PM optical amplifier.

An Acousto-Optic Modulator (AOM), combined with an electronic driver, is employed to frequency-select the pulse train to a lower frequency. After frequency selection, a second PM optical amplifier is used to amplify the pulse train. The RF signal from Calmar laser is injected into a 20 MHz low pass filter (LPF) to select the first 20 MHz tone. A frequency divider is used after the LPF to divide the frequency of RF signal from 20 MHz to sub-MHz. The signal with the

required repetition rate coming out from the frequency divider is amplified with an RF amplifier before being used to trigger the signal generator. The signal generator produces the square gating signal to modulate the 200 MHz carrier frequency signal from the AOM driver. This signal is applied to the AOM, resulting in an output pulse train with the desired repetition rate.

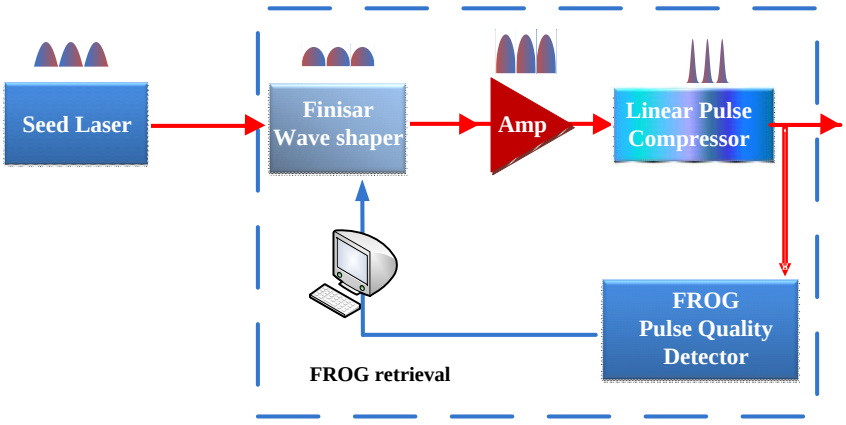

Figure 4-3 Block diagram of chirped pulse amplification with adaptive feedback loop (dashline box). Seed laser sends out stretched pulses, which are shaped into parabolic intensity profile with the Finisar waveshaper before being amplified with the booster amplifier. Amplified pulses are compressed with the linear pulse compressor to achieve short pulses. Part of pulses after compression is coupled out for monitoring and characterize with the SHG-FROG and fedback into the Finisar spectral processor to adjust the spectral modulation parameters.

A Liquid Crystal on Silicon phase and amplitude controller (LCOS) was used to shape the stretched pulses to produce a parabolic temporal intensity profile. The schematic, description and operation of the Finisar spectral processor can be seen in detail in the Appendix. After pulse shaping, an optical amplifier was used to amplify the pulses to high average power. A Treacy

grating pair was used to compress the amplified pulses to attain short pulses with high peak power.

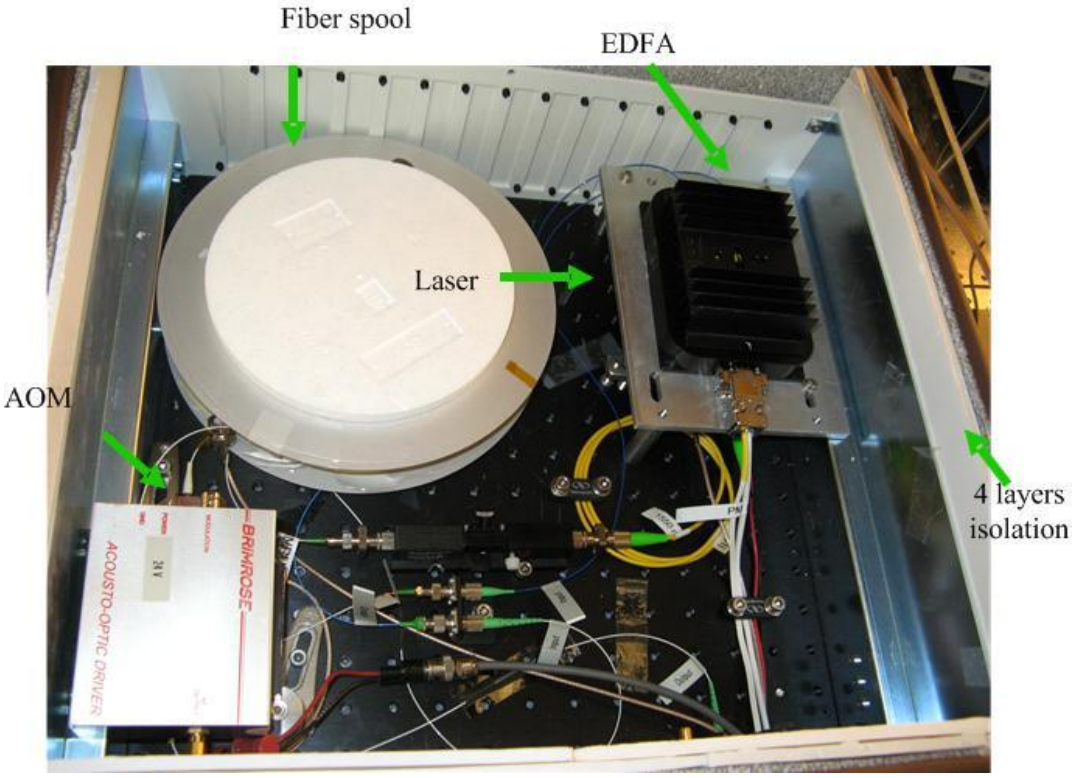

Figure 4-4. Laser source for a parabolic pulse shaping fiber CPA system. A fiber spool is used to stretch pulses to ~1.5 ns duration. Pulse train is frequency selected down from 20 MHz to 1.25 MHz by using an AOM synchronyzed with the output laser. A polarization maintaining Erbium-doped amplifier is used to pre-amplify the pulse after frequency selection before pulse shaping. A 4-layer thermal isolation box was used to house the laser and other fiber components to minimize the effect of environmental temperature fluctuation.

A Frequency Resolved Optical Gating (known by the acronym FROG) setup [57] will be implemented to analyse the quality of the pulses in terms of their temporal duration, intensity and

frequency chirp. The FROG spectrogram is a function of the frequency and time delay, are the squared magnitude of the Fourier transform of a 2D signal, and hence solvable by the phase retrieval algorithm [57–59]. The FROG-retrieved spectral phase output will be directed to a computer (PC). An adaptive feedback loop (Figure 4-3) is used to monitor the pulse quality using FROG and dynamically modify the pulse shaping parameters in the LCOS, based on the input profiles and the system response function, to result in pulses with minimal amounts of phase ripple, amplitude ripple, high order dispersion, and non linear effects.

In the following sections, a brief description and characterization of components used in CPA is shown. We will present results of frequency-selection down, and the output pulse train will be used as input for the Finisar waveshaper. Some preliminary results of parabolic pulse shaping by amplitude attenuating pulse optical spectrum using the Finisar is shown. A proposal of simulation of pulse propagation using split step Fourier method (SSFM) to study the effects of dispersion and high order nonlinearities will also be shown. Finally will be results and discussion.

4.3 System Components

4.3.1 Polarization Maintaining EDFA

Two custom-made Erbium doped EDFAs have been used in the experiment setup as the EDAF pre-amplifiers to compensate for the optical power loss before the stretched, parabolic shaped signal is amplified with a booster amplifier. The EDFA amplifier serves as a polarization

insensitive traveling wave amplifier (TWA), with a the typical gain within the range of 20-30 dB, and length of a few meters of optical fiber. Polarization maintaining Erbium doped fiber was used to constructed the amplfiers to simplify the task of controlling and maintaining polarization in the laser systems. The peformance of the PM EDFAs were experimentally characterized. From the Figure 4-5, the EDFAs operate over the wavelength range of 1545-1565 nm, with maximum output power of ~ 60 mW and small signal gain of 22 dB. The EDFAs were designed with internal optical filter to operate in this specific optical wavelength range to match the optical bandwidth of the CFBG stretcher in the experiment, to avoid and minimize effect of ASE. Output power of the EDFAs can be controlled by changing the driving supplied DC voltage, with range of applied voltage from DC to 2.5 Volts. To characterize gain parameter of the EDFA, a turnable CW laser is used, with center wavelength at 1550 nm, and input power of is incrementally increased every 0.1 mW upto 2.5 mW. The results shown in Figure 4-5(b) indicate a small signal gain of approximately 22 dB at 0.1 mW input power.

Table 1. Polarization Maintaining Erbium-doped Amplifier Specification

Parameters	Min	Typ	Max	Unit
Output Wavelength Range	1547.0		1558	nm
Max ouput power at -6dBm input	16			dBm
Input pulse width		1.0		ns
Input repetition rate	0.5		20.0	MHz
Input power range	-6.0		-2.5	dBm
Input pulse peak power			1.5	W
Small signal gain	25			dB
Polarization extinction ratio	20			dB

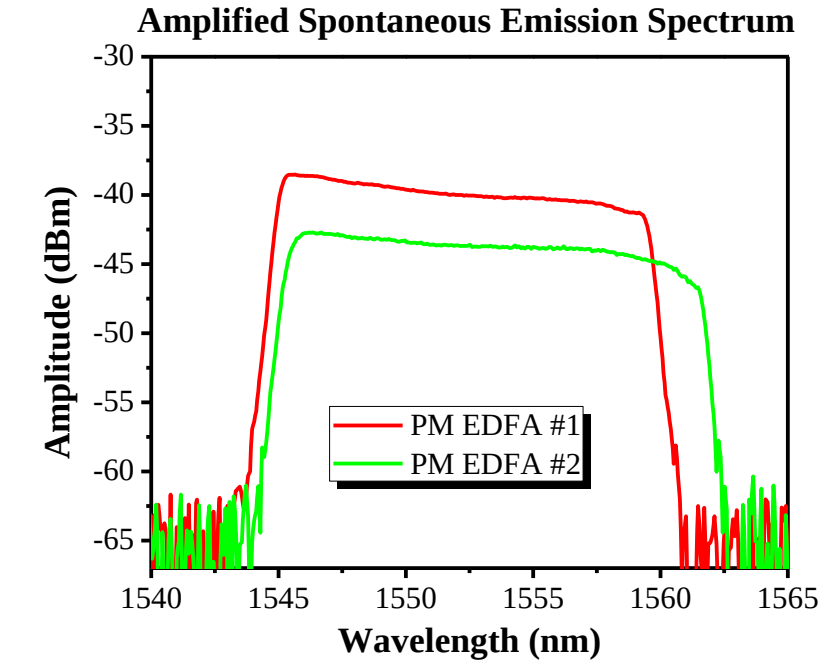

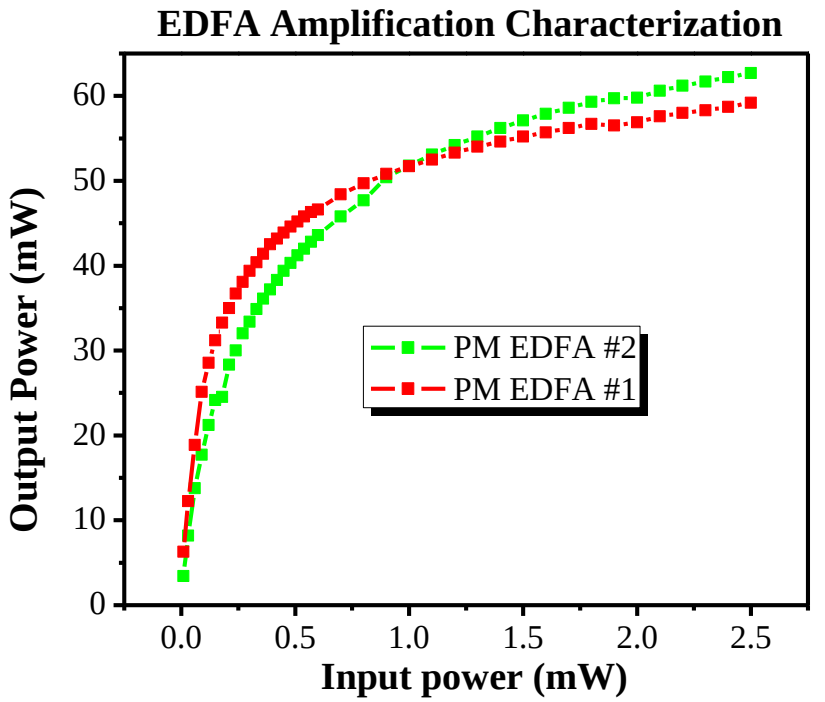

Figure 4-5 Polarization Maintaining EDFA Characterization

4.3.2 CFBG fiber stretcher

The first fiber Bragg grating had been fabricated by Ken Hill in 1978 [60] using a visible laser propagating along the core of fiber to induce structural change, and therefore permanently modify reflective index of the fiber. Subsequently, the holographic technique using the interference pattern of ultraviolet laser light coming from the side of fiber to create the periodic structure of the Bragg grating was demonstrated [61] (transverse holographic technique). The angle between the UV beams determines the period of the light pattern in the fiber core and consequently the Bragg wavelength. Another technique involves point-by-point inscription by infrared femtosecond laser to produce long period Bragg gratings [62].

The Bragg condition for the reflection of light involving refractive index perturbation can be expressed as

$$\frac{2\pi}{\Lambda} = 2\frac{2\pi n_{eff}}{\lambda} \tag{4.1}$$

Therefore $\lambda = 2\, n_{eff}\, \Lambda$;where Λ is the grating period, n_{eff} is effective refractive index of the fiber and λ is the Bragg wavelength. The Bragg condition means the wavenumber of the grating matches the difference of the opposite wave vectors of the incident and reflected waves. This condition also ensures that light of other wavelength not satisfying the Bragg condition would not be affected by the Bragg grating. The reflection bandwidth of the FBG depends on the length and strength of the refractive index modulation.

FBG since then has gained important applications such as gain equalizer to equalize gain of optical amplifiers. FBG can also be used in temperature and strain sensors. FBG can be designed to acts as dispersion compensation [63] to introduce a time delay as a function of wavelength, so that different wavelength is reflected at different grating location. FBG also acts as pump reflector in distributed fiber Bragg reflector (DBR) lasers and distributed feedback (DFB) laser as well as many other uses in fiber optic communication and fiber sensor application involving wavelength filtering [64].

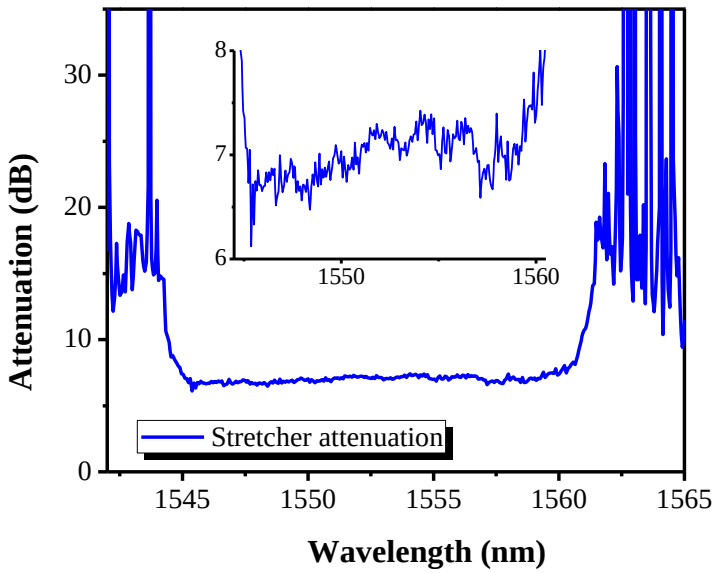

Figure 4-6. Pulse stretcher amplitude attenuation, with average attenuation is 7 dB. Outside the range 1542-1562 nm, the steep attenuation serves as an optical filter to cutoff undesirable bandwidth to limit the ASE effect. Inset: zoom-in of the plateau area, which indicate a non-uniform loss over the whole spectrum. The resulting intensity modulation would affect the overall quality of pulses, and therefore compensation for that modulation would require a broad bandwidth of modulation devices, such as intensity modulator, or spectral processor.

The FBG can be designed to operate either in transmission or reflection mode [64]. In this experiment, the CFBG is reflective fiber, with more than -40 dB transmission loss. The fiberized pulse stretcher has optical bandwidth of 20 nm and dispersion approximately 100 ps/nm. Figure 4-6 is the amplitude distortion caused by the pulse stretcher, which is the difference of optical spectrum before and after going through pulse stretcher. This distortion will be imparted on the optical spectrum of input pulse. The intensity mask applying to the Finisar to generate pulses with parabolic profile will compensate for this distortion.

One advantage of using fiber spool stretcher over chirped fiber Bragg grating stretcher is the low or non-existent non uniform loss of optical power over the input spectrum. As a result, output spectrum resembles input spectrum. Consequently, if input spectrum has smooth optical intensity profile, such as Gaussian shape, it would significantly reduce the required bandwidth of electrical components as well as resolution of optical devices, and at the same time, improve quality of output signals. However, as the fiber CFBG is inherently shorter than a typical fiber spool required to attain the same amount of dispersion, it's more stable to surrounding thermal fluctuation; and it is more likely to be immuned to mechanical vibration of the optical table and other environmental changes. A fiber CFBG also requires much shorter warm up time compared to a fiber stretcher spool. The fiber CFBG used in the setup has a physical length of about 70 cm, in contrast to several hundred meters fiber length of the fiber spool.

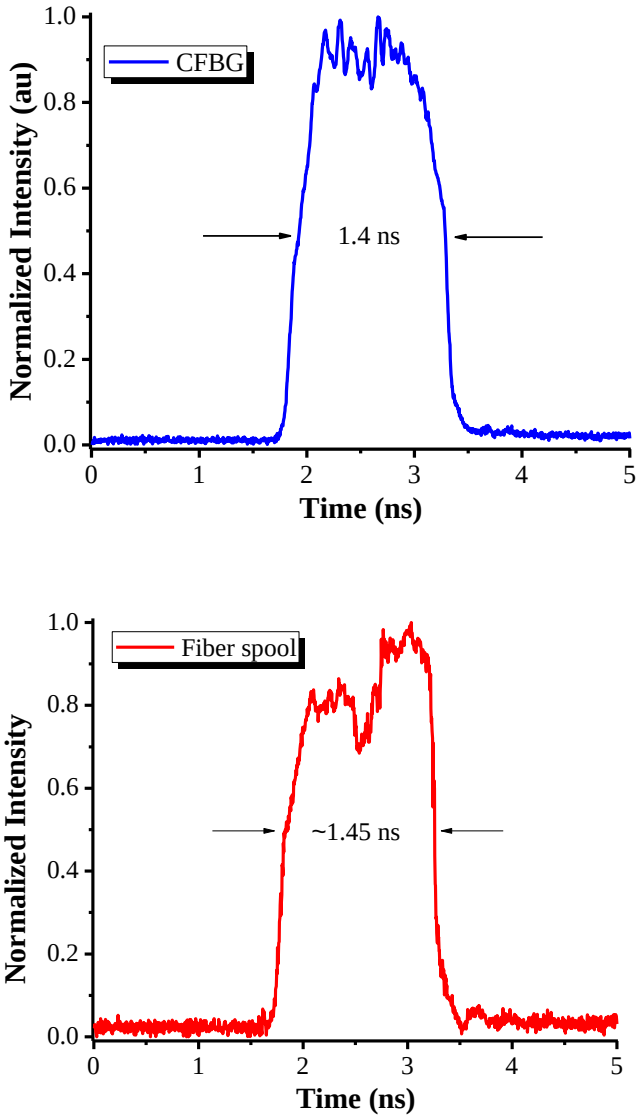

Figure 4-7. Comparison of stretched pulses with different dispersive media; subpicosecond, near transform limited pulses from a mode locked laser are stretched with (a) a commercially available Proximion chirped fiber Bragg grating, with dispersion value D ≈ 100 ps/nm (b) a custom made fiber spool of dispersion compensate fiber (DCF), with total dispersion designed to be approximately 100 ps/nm. Notice the apparent difference in optical profiles of output spectra is the result of changing polarization of input pulses, due to mechanical disposition or distortion of input fiber.

4.3.3 Treacy grating pair compressor

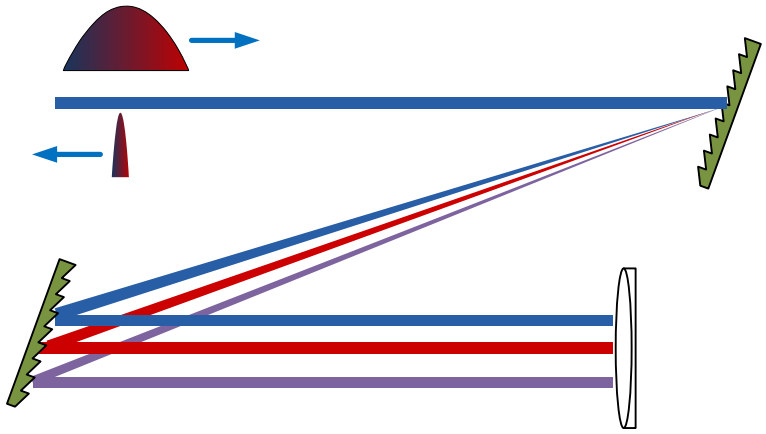

Figure 4-8. Geometry of the double-pass Treacy grating pair pulse compressor. The input beam incidents on the dispersion grating at Littrow angle, angularly disperses on the second grating. A flat mirror is used to reflect the dispersed beams back. The reflected beams then recombine at the first grating before tracing their way back to output port [65,66]. In the experiment, a roof-mirror was used instead of the flat mirror to separate input and output beams to different ports.

The Treacy grating pair compressor utilizes a parallel pair of identical diffraction grating in an arrangement first introduced by Treacy [66]. Unlike the Martínez-type compressor containing two lenses between the gratings, which can provide normal dispersion [67], the Treacy grating pair compressor can provide only anomalous dispersion. The architecture of the Treacy grating pair has high tolerance for optical systems with high peak power, without introducing additional nonlinear distortions. The grating pair compressor is very suitable for this

task, since they can be operated with large mode areas, in contrast to FBG, which limits the pulse energy to below 1 μJ, but there is size constrain in the fabrication of large volume Bragg grating.

Another unfavorable aspect of the volume compressor is the substantial reflection loss, which can be as high as 3 dB on a double pass grating pair. For that reason, electron beam lithography is employed to fabricate special transmission gratings, with only 0.13 dB, or ~3% optical power loss.

Besides the dispersion from the pulse stretcher, there will be additional dispersion resulting from chromatic dispersion (or material dispersion) and other nonlinearity effects when propagating through gain medium and other optical components. Therefore the dual grating compressor is constructed with the overall dispersion taken into account. The total amount of chromatic dispersion required in the stretcher and the compressor also depends on the initial pulse optical bandwidth, which should thus not be too small. Conversely, very large bandwidths introduce problems with matching higher-order dispersion on one hand, and gain narrowing in the amplifier on the other hand. Therefore, CPA systems employing dispersion grating pair work best for pulse temporal durations within few femtoseconds to a few hundred femtoseconds [5].

In this setup, the distance between two dispersive gratings is approximately 60 cm, with the incident angle at ~ 15^{o}. The alignment was such that center wavelength of the incident beam at 1552 nm illuminates the centers of the second grating after being angularly dispersed from the first grating. This condition is to ensure the spreading of dispersed beam over the entire surface of the second grating, thus avoiding beam clipping at the edges of the beam, and consequently, reducing optical bandwidth of pulses.

The dispersion of the grating pairs can be calculated using the following equation [65]

$$\frac{\partial \tau}{\partial \lambda} = \frac{\lambda b}{c}\left(\frac{d\theta_D}{d\lambda}\right)^2 \tag{4.2}$$

Where θ_D is the diffracted angle, which is a function of the frequency and incident angle θ_i, b is the slant distance between two gratings, c is the speed of light, λ is the optical wavelength, and propagation time $\tau = \partial\psi(\omega)/\partial\omega$ is the derivative of spectral phase over frequency. The angular dispersion is obtained from the grating equation

$$sin\theta_D = sin\theta_i + \frac{m\lambda}{d} \tag{4.3}$$

With d is the periodicity of the grating rulings and m is the diffraction order. In this setting, the grating is 1200 lines/mm, so d= (1200 lines/mm)$^{-1}$, and the gratings are used in the first-order Littrow configuration, or $m = -1$. Consequently, by differentiating the previous equation, we can obtain angular dispersion

$$\frac{\partial \theta_D}{\partial \lambda} = \frac{m}{d\cos\theta_D} \tag{4.4}$$

Resulting in second derivative of path length P over wavelength λ

$$\frac{\partial^2 P}{\partial \lambda^2} = \frac{m^2 b}{d^2 \cos^2 \theta_D} \tag{4.5}$$

Finally the anomalous dispersion for a double pass grating pairs compressor

$$D = \frac{\partial \tau}{\partial \lambda} = 2\frac{m^2 \lambda b}{c d^2 \cos^2 \theta_D} \tag{4.6}$$

or in terms of phase

$$\frac{\partial^2 \psi}{\partial \omega^2} = 2\frac{m^2 \lambda b}{2\pi c^2 d^2 \cos^2 \theta_D} \tag{4.7}$$

The third-order dispersion becomes important when compensating a chirp over a wide bandwidth, which has the opposite sign to the second-order dispersion

$$\frac{\partial^2\psi}{\partial\omega^2} = 2\frac{-\lambda^3}{2\pi c^2}\frac{\partial^2 P}{\partial\lambda^2} \Rightarrow \frac{\partial^3\psi}{\partial\omega^3} = 2\frac{-\lambda^4}{2\pi^2 c^3}\left(3\frac{\partial^2 P}{\partial\lambda^2} + \lambda\frac{\partial^3 P}{\partial\lambda^3}\right) \tag{4.8}$$

And for parallel diffraction gratings,

$$\frac{\partial^3\psi}{\partial\omega^3} = 2\frac{-3m^2\lambda^4 b}{4\pi^2 c^3\, d^2\cos^2\theta_D}\left(1 + \frac{m\lambda}{d}\frac{\sin\theta_D}{\cos^2\theta_D}\right) \tag{4.9}$$

Inversely, if input pulse is linearly chirped (purely quadratic spectral phase), then this third order phase term must be small for the grating pairs to provide high quality pulse compression, or $\frac{1}{6}\partial^3\psi/\partial\omega^3(\Delta\omega)^3 \ll \pi$, with $\Delta\omega$ is the optical bandwidth. The sign difference of the second and third order dispersion means that the grating pairs cannot be used to compensate both 2nd and 3rd order material dispersion [68,69].

4.3.4 Second Harmonic Generation Frequency Resolved Optical

4.3.4.1 Introduction to the FROG Technique

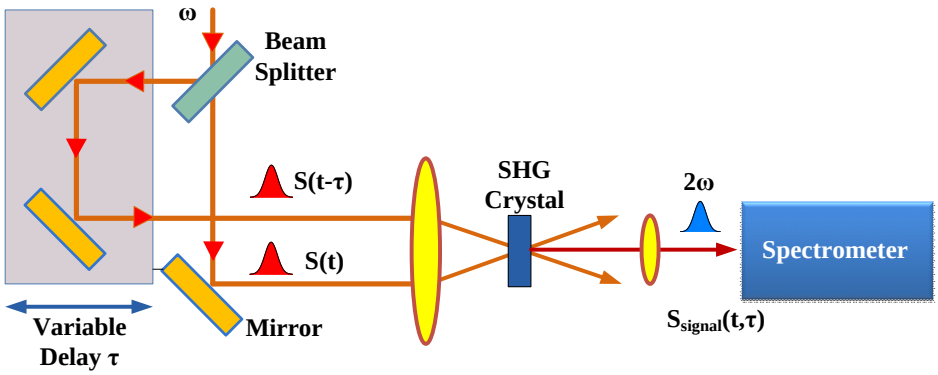

Figure 4-9. Schematic of a SHG-FROG setup. The physical size of the FROG depends on the optics in the experiment, and typically 2x2 feet. An up-to-date, single shot GRENOUILLE would be significantly smaller, with physical size 26 cm x 4.5 cm x 11.5 cm

The second harmonic generation frequency-resolved optical gating (SHG-FROG) is a well-known technique that completely measures and characterize ultrashort laser pulses to give the phase and time dependent intensity of pulse, with range from several femtoseconds to nanosecond in length [70]. This technique is mathematically rigorous, involving a second harmonic generation setup with a phase retrieval algorithm to deliver information of the spectral intensity and spectral phase of the ultrashort pulses [57–59,71,72]. The FROG has been demonstrated to be a reliable technique to characterize laser systems with temporal pulses width ranging from several femtoseconds to several picoseconds. Chirped pulse amplification systems

had been analyzed with the FROG to provide direct observation of residual phase distortion in the CPA system [73].

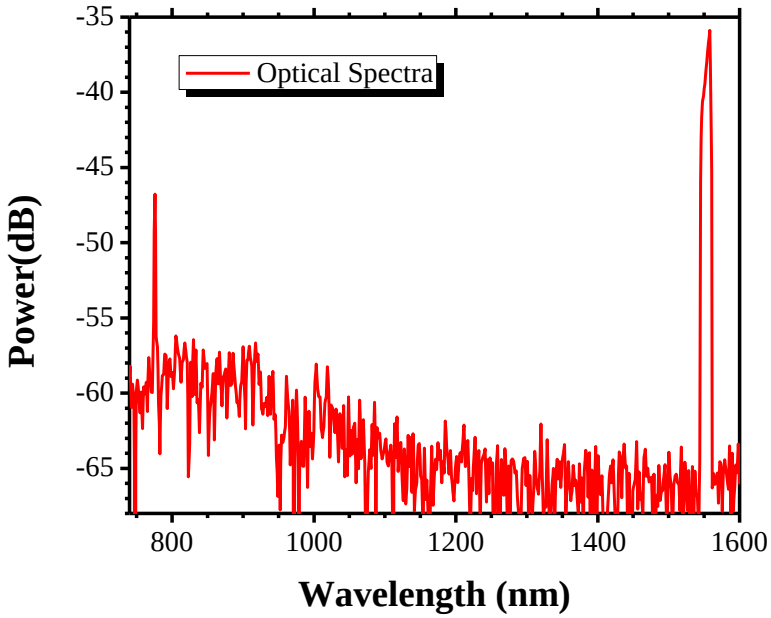

Figure 4-10. Optical spectrum of fundamental signal and corresponding SHG signal as observed on the OSA. In this particular example, the input fundamental signal is the Calmar laser pulse, which assumes the squarish shape. The maximum intensity of SHG signal is approximately 10 dB lower than the maximum intensityof the input fundamental signal, which is typical for BBO nonlinear crystal used in the FROG.

However, there are also several drawbacks of the FROG approach, including the bulky size of the FROG setup, complexity of free-space optic alignment, typical high peak power requirement to achieve a good signal to noise contrast, ambiguous time reversal, as well as long data acquisition and processing time.

Many different SHG spectra are measured as a function of temporal delay τ, by incrementally changing the optical path length difference between two arms. The FROG spectrogram is then constructed by stitching together the SHG spectra, as a 2D function of time delay τ and wavelength. The spectrogram as a time-frequency distribution is used to characterize signals whose spectral content is varying over time. The time delay $\Delta\tau$ is chosen with respect to the temporal width of the pulse so that an accurate picture of pulse is obtained, typically about one tenth to one fifth of the pulse full-width half maximum (FWHM) width, depending on the complexity of the pulse. The temporal duration of time delay needs to be chosen so that any signal that is greater than 10^{-4} of the maximum intensity of SHG trace should be included in the recorded spectrogram.

The experimentally measured FROG spectrogram is then used as input to the iterative algorithm to retrieve the temporal intensity and spectral phase of the pulse [71,74,75]. The FROG iterative retrieval algorithm is based on the iterative Fourier transform algorithm, developed in the field of phase retrieval.

The phase retrieval algorithm is a well-known problem, and is called two-dimensional phase-retrieval problem to reconstruct quantitative information about the electric field and the phase, which is discussed in detail in [58,59,76]. The reliability of this technique stems from the redundancy of the FROG spectrogram. For example, an electric field sampled at N points has 2N degrees of freedom, taking into account both intensity and phase. However, the FROG spectrogram corresponds to this field has N^2 pixels, representing N^2 degrees of freedom. Therefore the FROG trace is oversampled, meaning that there are many more possible FROG

spectrograms, than are allowed by a physically realizable electric field. The result is, if some systematic or random error is added to a retrieved FROG spectrogram, it will be unlikely to correspond to an experimentally measured FROG spectrogram, leading to the non-convergence of the algorithm.

4.3.4.2 **Retrieval algorithm of the FROG spectrogram**

The FROG is a simple spectrally resolved autocorrelation. To retrieve pulse information using FROG, an iterative phase retrieval algorithm is implemented [58], which has been proven to be robust, fast and reliable, with convergence usually takes under several seconds, unless the pulse is rather complex. Therefore FROG has become an effective tool to characterize ultrashort laser pulses.

In Figure 4-9, the schematic of a SHG-FROG setup is shown. Input beam is split into two components, a reference arm and a delay arm. These two beams overlap in the second harmonic generation (SHG) crystal and produce another pulse. This signal has a new wavelength which is half the wavelength, and frequency which is double of the frequency of input pulse.

$$A^2(\tau) = \int_{-\infty}^{\infty} I(t)I(t-\tau)\,dt \tag{4.10}$$

The resulting signal is called intensity autocorrelation, with gives temporal information of the pulses. This intensity autocorrelation trace doesn't contain enough information to retrieve spectral phase. Therefore a FROG spectrogram needs to be constructed. The FROG spectrogram is essentially the product of the electric field E(t) and the gate function g(t-τ), which gates out a portion of E(t), centered at τ, $g(t-\tau) \approx |E(t-\tau)|^2$ using the pulse itself as the gate function,

The FROG algorithms starts with a guess for the complex electric field E(t), with the addition of noise in the standard phase retrieval. This electric field E(t) is used to generate the signal field $E_{Sig}(t,\tau)$ from the equation $E_{Sig}(t,\tau) \propto E(t)g(t-\tau) = E(t)|E(t-\tau)|^2$ as given in [65]

This signal field is then Fourier transformed with respect to time to obtain $E_{Sig}(\omega,\tau)$.

$$E_{Sig}(\omega,\tau) = \int_{-\infty}^{\infty} dt E_{Sig}(t,\tau)\, exp(-i\omega t) \tag{4.11}$$

with the magnitude of the FROG trace

$$I_{FROG}(\omega,\tau) = \left|E_{Sig}(\omega,\tau)\right|^2 = \left|\int dt E_{Sig}(t,\tau)e^{-i\omega t}\right|^2 = \left|\int dt E(t)g(t-\tau)e^{-i\omega t}\right|^2 \tag{4.12}$$

By substituting t'= $t-\tau$, the equation for I_{FROG} can be seen as a symmetric function of τ

$$I_{FROG}(\omega,\tau) = I_{FROG}(\omega,-\tau) \tag{4.13}$$

Consequently, SHG-FROG trace has a time reversal ambiguity, resulting from using the same pulse as gating function.

The magnitude of this signal is subsequently replaced by the magnitude of the experimentally measured FROG trace through the equation

$$E'_{Sig}(\omega,\tau) = \frac{E_{Sig}(\omega,\tau)}{\left|E_{Sig}(\omega,\tau)\right|}\left|I_{FROG}(\omega,\tau)\right|^{1/2} \tag{4.14}$$

just as in the usual phase retrieval problem. This new signal field $E'_{Sig}(\omega,\tau)$ is then inverse Fourier transformed to yield $E'_{Sig}(t,\tau)$. By integrating this new temporal signal field $E'_{Sig}(t,\tau)$ with respect to τ, we generate a new guess for E(t).

We then start a new cycle of this procedure, using this new E(t) as our new input. If the current E(t) is the correct one, then the signal field $E_{Sig}(t,\tau)$ would stay unchanged, meaning the new E(t) after this cycle will remain the same. So basically this FROG algorithm iterates, alternatively applying the experimentally measured FROG spectrogram data and enforcing compliance to achieve convergence. The convergence of this algorithm is evaluated by calculating the FROG error, defined as the root-mean-square (rms) difference between the measured FROG spectrogram and the FROG trace of the recovered field

$$G = \left\{ \frac{1}{N^2} \sum_{\omega,\tau=1}^{N} [I_m(\omega,\tau) - I_r(\omega,\tau)]^2 \right\}^{1/2} \quad (4.15)$$

Where I_m is the measured FROG trace, and I_r is the recovered FROG trace, N is the number of frequency and delay points in the trace. The convergence is considered satisfactory when the value of G is on the order of 10^{-3} to 10^{-4} for experimentally measured data.

The FROG spectral retrieval can be further validated by the use of marginal, which are the one-dimensional curves obtained by integrating the FROG spectrogram over one of its coordinates. This marginal can then be compared with the characteristics of pulses such as optical spectrum and autocorrelation. When the computer retrieved results converge with the experimentally measured data, we can be assured of the consistency of the FROG results [65,72,77].

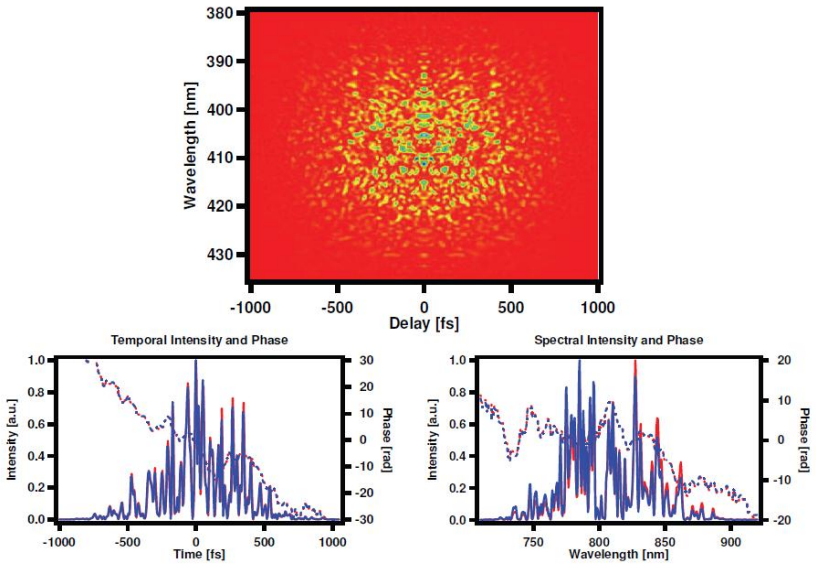

Figure 4-11. Example of SHG FROG Spectrogram of an extremely complex pulse. Top: SHG FROG spectrogram of a pulse with a time-bandwidth product of approximately 100. Bottom, the actual (red) and retrieved (blue) pulses. Adapted from [70]

4.4 Dynamic Feedback Pulse Shaping Procedure

4.4.1 Parabolic intensity pulse shaping

In Figure 4-12 (a), the optical spectrum of pulse without pulse shaping is shown (blue). This optical spectrum has an optical bandwidth of about 15 nm at 10 dB, centered around 1552.5 nm. The desired parabolic pulse output is shown in Figure 4-12 (a) in red dashed. Initially, only spectral amplitude of the input pulse is attenuated to produce parabolic shape of output pulse, phase modulation is not yet performed.

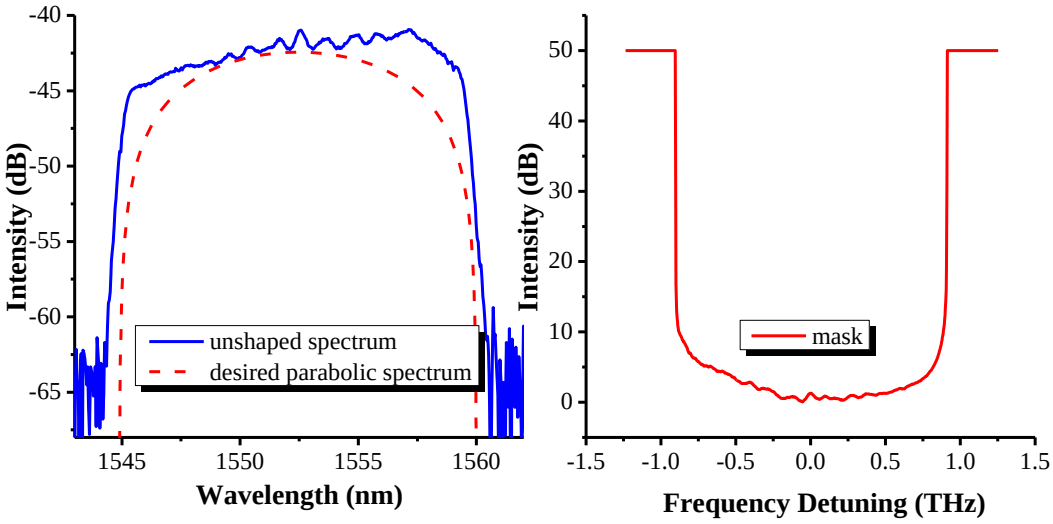

Figure 4-12. Optical spectrum of input signal (solid) and target output signal in logarithmic scale (dashed) (b) Required intensity mask in logarithmic scale, this mask is calculated by taking the difference between input spectrum and desired output spectrum. The signal to noise ratio of the intensity mask is designed according to the modulation depth of the Finisar spectral processor of maximum attenuation 50 dB. This exceeds the signal to noise ratio of input signal of less than 30 dB, ensuring high quality, low noise, and sharp edge output parabolic output pulses.

A mask function is generated by taking the difference between the input optical spectrum (solid) and the desired optical spectrum (dashed) in Figure 4-12 (a). This mask is depicted in Figure 4-12 (b), and is applied to the Finisar spectral processor to produce a parabolic output optical spectrum. The quality of pulse shaping can be improved by utilizing a feedback loop to better tune the mask function with any instantaneous change in the spectral shape of input pulse due to changes in the surrounding environment.

Output pulses after intensity shaping are amplified with an optical amplifier and subsequently compressed with a Treacy compressor. The compressed pulses are sent to the SHG-FROG to analyze and retrieve spectral phase information. This phase information is then fed back to the Finisar spectral processor to adjust phase shaping done on the input pulses. In addition, an autocorrelator is used to monitor quality of of generated parabolic pulses in real-time and to cross-check with results from the FROG. The usage of the autocorrelation has the advantage of providing fast, accurate evaluation of pulses, in contrast to the measurement using FROG,which is rather time consuming.

4.4.2 SHG-FROG Operation

The schematic of a Frequency Resolved Optical Gating (FROG) is depicted in Figure 4-13. A mode-locked laser with 15 nm optical bandwidth at 10 dB, centered at 1553 nm and 1.25 MHz repetition rate was used to calibrate and align the FROG, as shown in Figure 4-14(a). The input beam from this mode-locked laser was split into a delay arm and a reference arm before being focussed on a 1mm-thick BBO nonlinear crystal. A New Focus picometer motorized translational stage is used in the variable optical delay to adjust the difference of optical path length, or time delay. The picometer includes a network controller (model 8752) and a driver, which can control up to three individual piezo Picometer actuators. The piezo linear actuator has travel range of 50.8 mm, and minimum incremental motion of less than 30 nm, or 0.1 fs time delay in free space. A SHG signal was produced at zero-delay and observed on the optical spectrum analyzer shown in Figure 4-14 (b).

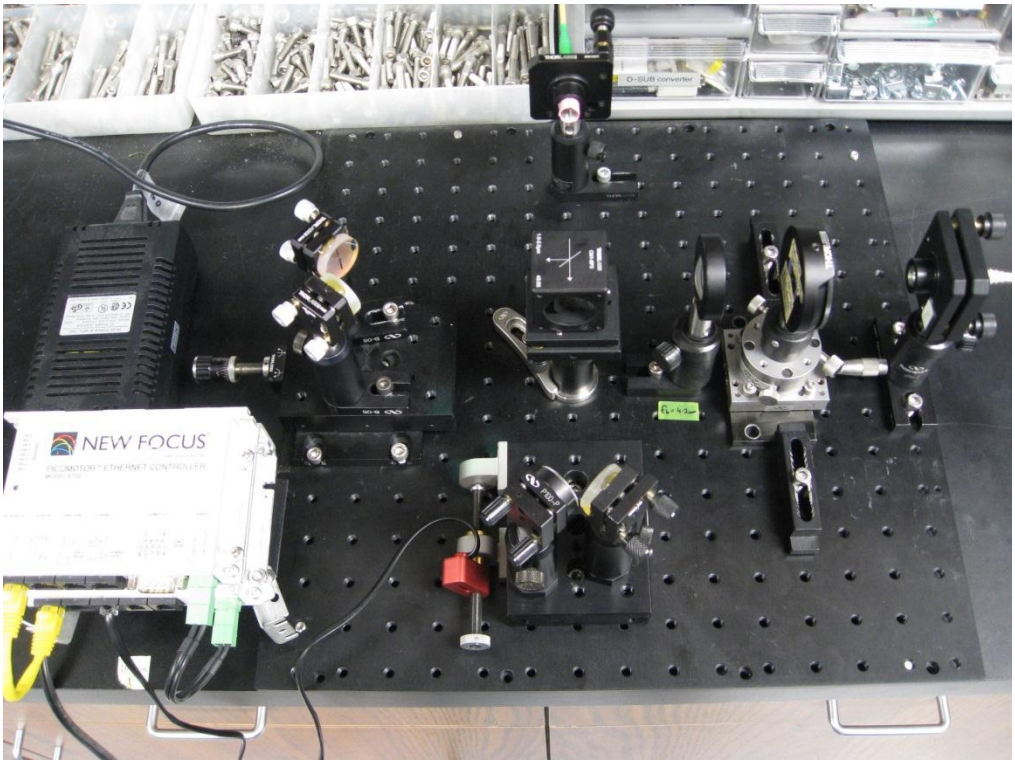

Figure 4-13. Setup of a Second Harmonic Generation FROG apparatus. A pulse is split into two, and one beam is delayed with a variable optical delay. The two beam is recombined at a second harmonic generation crystal, to generate a second harmonic pulse; this SHG spectrum is then recorded with the spectrometer as a function of the relative time delay.

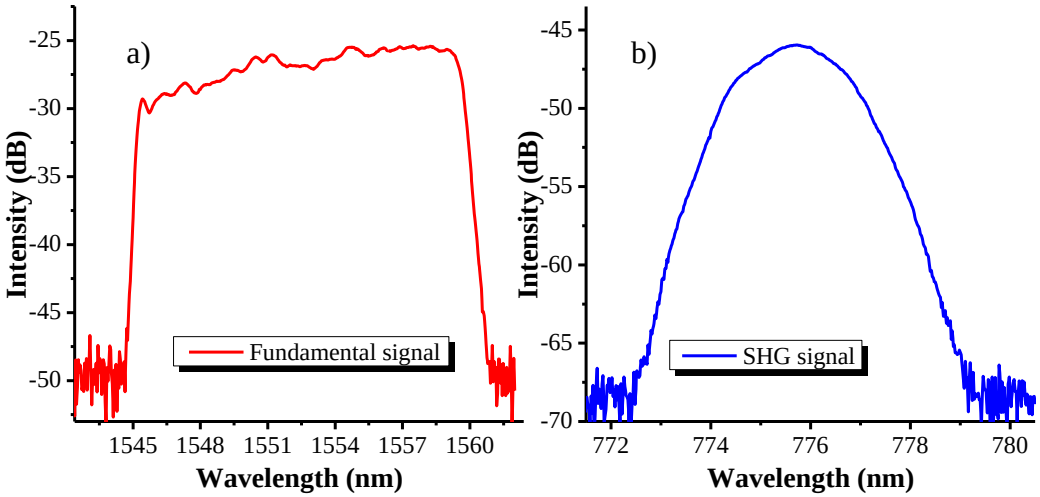

Figure 4-14. Optical spectrum of (a) fundamental signals, the fundamental spectrum has a square-ish shape, with 10 dB bandwidth of approximately 15 nm (b) The SHG signal is the product of the auto correlation of two identical pulses, and has triangular shape, which is the typical cross correlation product of two square pulses. The intensity profile of the SHG shows contrast of ~23 dB signal-to-noise ratio, more than required to achieve accurate FROG retrieval analysis.

A FROG spectrogram is constructed, by recording many SHG spectra at different setting of delay between two arms. In order to ensure the high resolution of the FROG spectrogram as well as the retrieval pulse information, a 1024x1024 FROG spectrogram was generated, which consists of 1024 SHG optical spectrum (or trace) of 1024 data points each. The optical spectra of the FROG traces ranges from 771-781 nm, and each spectra was measured at time delay step of 48 fs. A computer software was used to communicate and control the motorized translational stage to ajust optical path length, or time delay, after the SHG spectum was recorded.

These spectra are then stiched together to generate a 2D spectrogram of SHG signals as a function of wavelength and time delay. The FROG spectrogram utilizes color codes to display intensity as a function of time delay versus wavelength. The horizontal axis of a FROG spectrogram corresponds to a temporal coordinate, while vertical axis corresponds to a wavelength (or frequency) coordinate. These two axes are related by the Fourier transform relationship, therefore fixing the aspect ratio of the FROG spectrogram. A FROG software is used to analyze this spectrogram to retrieve phase information of input pulse, with details of the retrieval algorithms desribed in detail in previous section. The retrieval FROG spectrogram should have minimal difference with the original FROG spectrogram, indicated by the convergence error (less than 0.005 for experimental data). Typically this data processing operation, together with data acquisition, takes about 20 hours, with data acquisition being the fastest procedure of approximately 3 hours.

4.5 Results and Discussion

4.5.1 Pulse shaping utilizing CFBG fiber stretcher

In the first setup, a fiberized CFBG was used as the temporal pulse stretcher. The length of the fiber CFBG is approximately 1 meter, and is suitable for reducing the physical footprint of CPA systems. The short length of the fiber CFBG also makes it much less susceptible to fluctuations in environmental temperature.

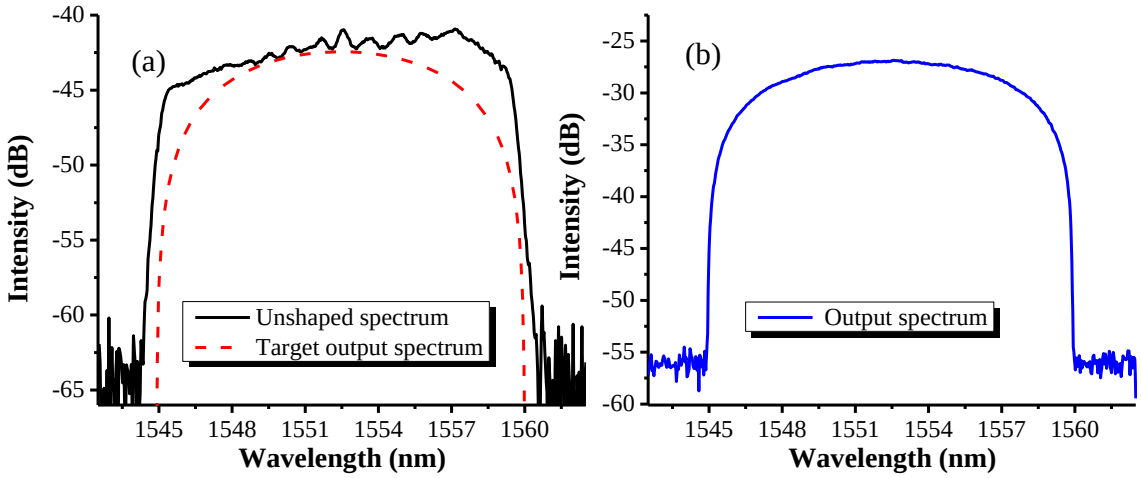

Figure 4-15. Optical spectrum without pulse shaping (solid) and desired output spectrum (dashed) (b) Typical parabolic spectrum generated with the spectral processor. The parabolic pulse after pulse shaping has signal to noise ratio of more than 27 dB and optical bandwidth of approximately 15 nm at 10 dB.

Initially, only spectral intensity modulation was applied to the input pulses. A spectral intensity mask was generated by taking the difference between input spectrum and the desired target output spectrum seen in Figure 4-15(a). This mask was applied to the Finisar spectral processor to produce the desired parabolic optical intensity shape. These output pulses have 15 nm optical bandwidth at 10 dB, centered around 1552.5 nm and have temporal width of 1.4 ps. The output parabolic pulses after intensity shaping, in Figure 4-15(b), were amplified before being compressed with the bulk compressor.

These amplified pulses were sent to the FROG to retrieve spectral phase information. A FROG spectrogram (Figure 4-16) was constructed by collecting 1024 FROG traces by gradually

varying the arrival time difference of the two pulses on two arms of the FROG, with delay setting at 48 fs between traces. These traces, which are the optical spectra of SHG pulses at various delay setting, are afterward stitched together to generate the color-coded, 2-D spectrogram. Due to the symmetry of the pulses and the delay sweeping, the spectrogram also appears to be symmetric along the zero – delay vertical axis, with highest peak power at the center of the spectrogram.

A commercially available FROG software, which implements an iterative phase retrieval algorithm, was used to reconstruct the pulse shape from the FROG spectrogram. The retrieval error of the retrieval procedure was on the order of 1.5E-3, showing a very good convergence. Based on this phase information, the Finisar spectral processor was programmed to adjust phase modulation applied to the input pulse, resulting in much shorter measured autocorrelation (AC) trace and significant reduction of temporal pedestals. In Figure 4-16, the FROG spectrograms of the pulses with and without pulse shaping are shown. Clearly, the shape of spectrogram changes, as well as the green wings (indicates chirp, or higher order dispersion) have been cleaned up very well.

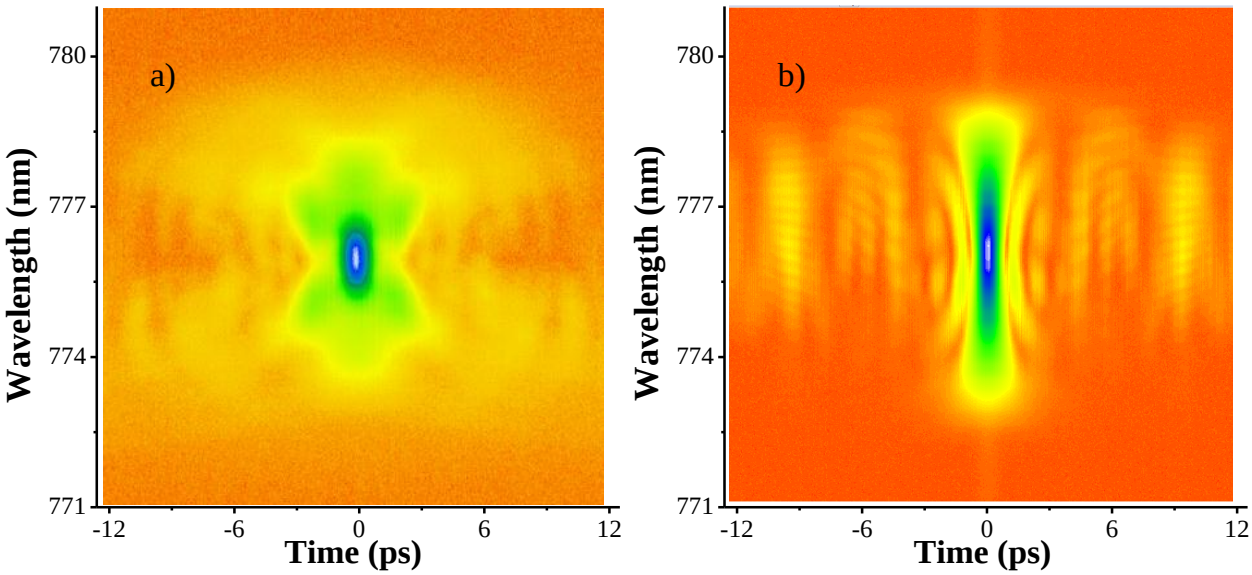

Figure 4-16. (a) Measured FROG spectrogram of CPA pulse without pulse shaping (b) Measured FROG spectrogram with both spectral intensity and phase shaping. Horizontal axis is time, with temporal duration of 24.5 ps, vertical axis is optical wavelength, ranging from 771-781 nm. Notice the significant temporal wings reduction in the spectrogram of pulses after pulse shaping compared with spectrogram of pulse before pulse shaping. The spectrograms were color-coded such that the highest power area is depicted in white, followed by the blue rings and subsequently the green pedestal wings, and the background is shown in orange/red. The spectrogram after pulse shaping is re-normalized so that the background is shown in red, indicating a substantial increase in peak power.

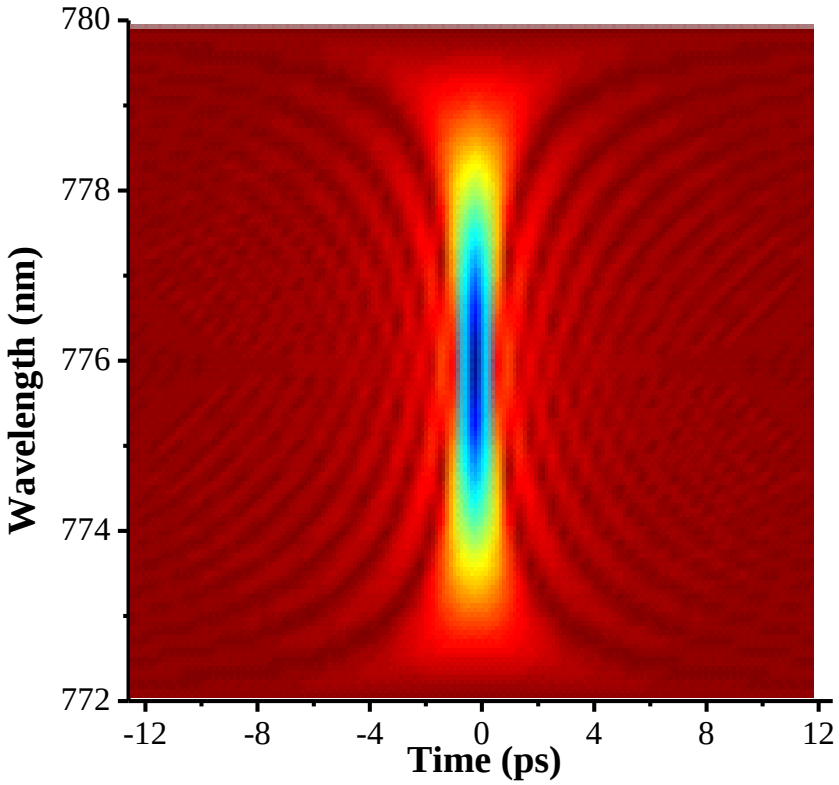

Figure 4-17. Simulation results of SHG-FROG spectrogram generated with input zero-chirped parabolic intensity pulses, horizontal axis is time delay from -12.45 to 12.45 ps, vertical axis is wavelength, centered around 776 nm. The simulation spectrogram matches the measured FROG spectrogram above very well.

Figure 4-16 (a) shows the measured FROG spectrogram of CPA pulses without pulse shaping. The temporal green wings correspond to the temporal pedestals of the pulse, which can also be observed on the autocorrelation trace measured with the autocorrelator. The shape of the experimental FROG spectrogram in Figure 4-16 (b) indicates a chirp-free pulse, with significant temporal wings reduction. These results are further validated by comparing experimental FROG spectrograms with simulation results seen in Figure 4-17.

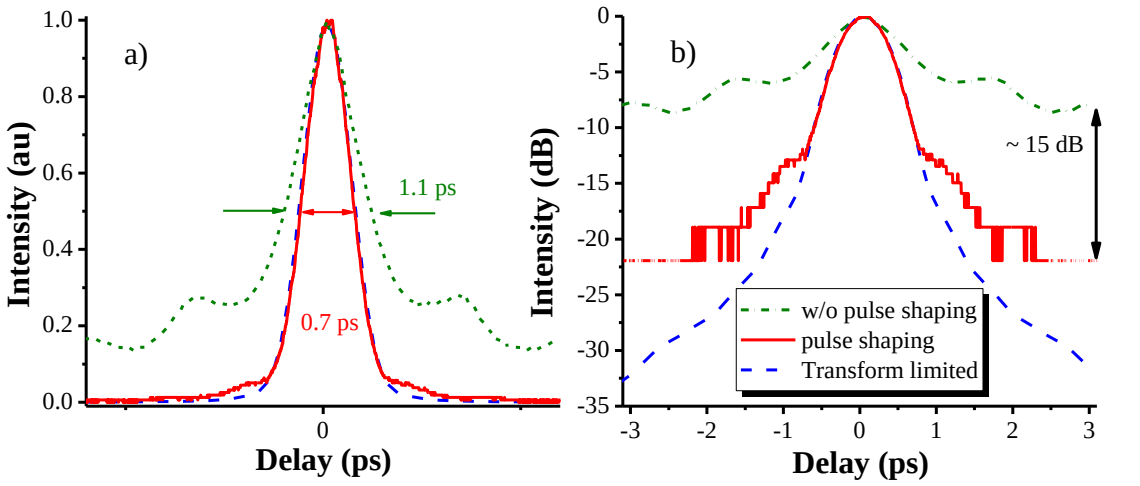

Figure 4-18. Calculated (dashed) and measured (solid) AC traces, in comparison with an AC trace of unshaped CPA pulses (short dashed) in (a) linear scale, with temporal intensity normalized to unity (b) logarithmic scale.

In Figure 4-18(a), the measured autocorrelation trace of pulse without pulse shaping is shown with temporal duration of 1.1 ps at FWHM, with the amplitude of autocorrelation traces normalized to unity. After parabolic pulse shaping, a 0.7 ps temporal duration autocorrelation trace was achieved. This measured autocorrelation trace shows an excellent agreement with a calculated autocorrelation trace of transform-limited pulses with the same parabolic optical spectrum. In order to specify the quality of the compressed pulses as the result of parabolic pulse shaping, the autocorrelation traces were re-plotted in logarithmic scale in Figure 4-18 (b). In this figure, the autocorrelation race of shaped pulse agrees with transform limited pulse up to 12 dB, at approximately 1 ps delay. The pedestals in temporal profile of a CPA pulse without pulse

shaping have been suppressed by 15 dB at 3 ps delay. These results clearly show that a substantial amount of energy under the pedestals on the wings has been transferred to the central lobe, significantly increases pulse peak power.

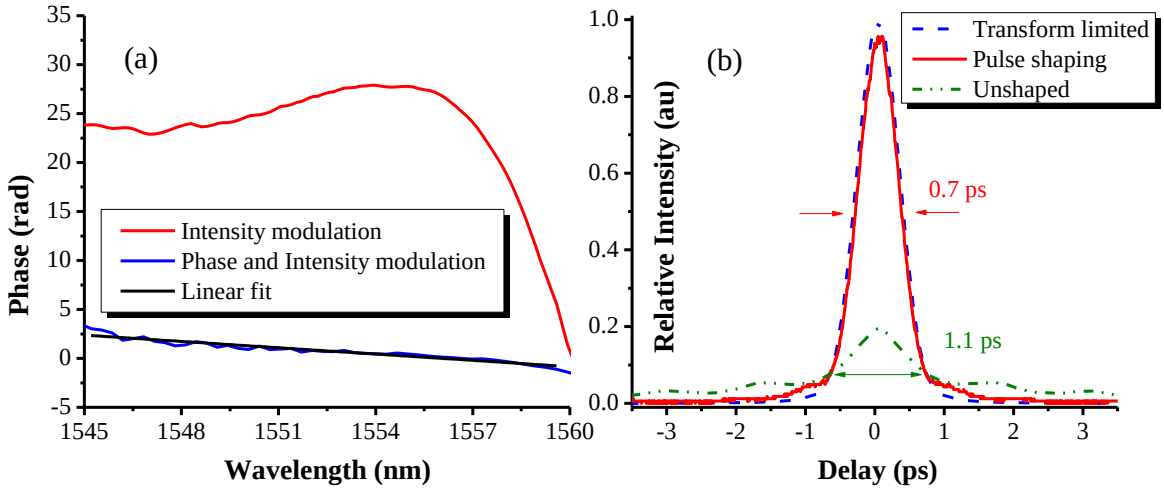

Figure 4-19. (a) Reconstructed spectral phase with only spectral intensity modulation (red), with both spectral phase and intensity modulation (blue), and its linear fit (b) Calculated and measured AC traces, in comparison with an AC trace of unshaped CPA pulses.

In Figure 4-19(a), the reconstructed spectral phases are plotted. The red curve is the spectral phase of pulses without pulse shaping, ranging from 0 to 28 radians. The shape of the curve corroborates the existence of high order dispersion (or chirp). After pulse shaping, the retrieved spectral phase of pulses with pulse shaping is shown in blue. The linear fit of the retrieved spectral phase indicates a maximum deviation of 0.75 radians towards the left tail of the spectrum, almost flat phase across the center, with 0.25 radians root mean square deviation.

In Figure 4-19 (b), the autocorrelation traces are plotted with normalized power under curve. In this figure, the peak power of CPA pulses with pulse shaping (red) is comparable to the maximum theoretical peak power of the calculated transform limited pulses (blue) with the same parabolic optical spectrum, and is increased by a factor of 5, compared to the peak power of unshaped pulses (green).

4.5.2 Pulse shaping utilizing fiber spool stretcher

When the CPA systems operate in high power amplification stage, the fiber nonlinearities, such as self-phase modulation can still be present, with even a small deviation in spectral intensity from a perfect parabola can results in substantial nonlinear phase accumulation, and consequently a spectral modulation is imposed on the envelope spectrum as seen in Figure 4-20. This imperfection is due to the presence of very high frequency intensity modulation imparted by the CFBG on the spectrum, which couldn't be compensated by the Finisar spectral processor, which has spectral resolution of +/- 5 GHz. This intensity modulation can be measured by comparing the optical spectrum of the pulse before and after stretching with the CFBG.

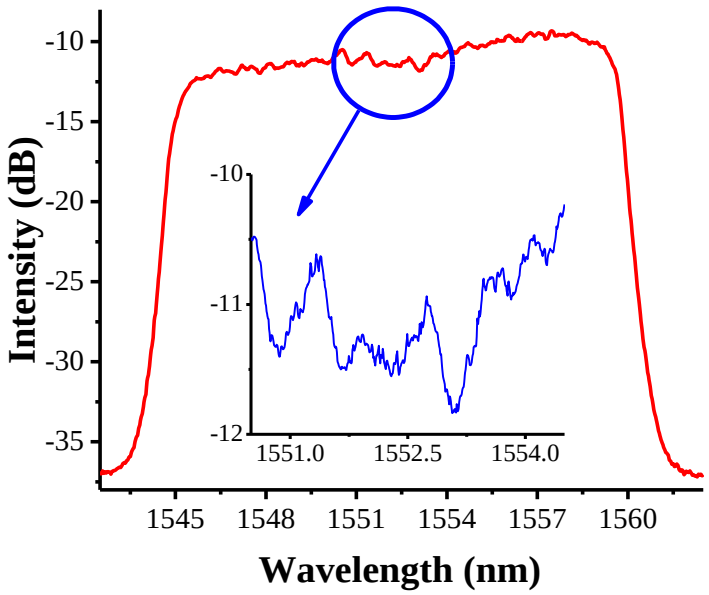

Figure 4-20. Input optical spectrum of seed laser after stretching with a CFBG. The sharp edges of the spectrum is the result of the presence of optical filter embeded with the CFBG unit. Inset is the zoomed-in spectrum with visible high frequency modulation imparted by the CFBG. This high frequency modulation is the result of non-uniform loss of pulse intensity across the optical bandwidh of the CFBG.

In the second setup, a fiber stretcher with minimal group delay ripple (GDR) was used to avoid the high frequency modulation on the optical intensity spectrum. As a result, the amount of spectral intensity modulation on amplified optical intensity spectrum was reduced significantly from 7 dB to less than 2 dB, shown in Figure 4-21.

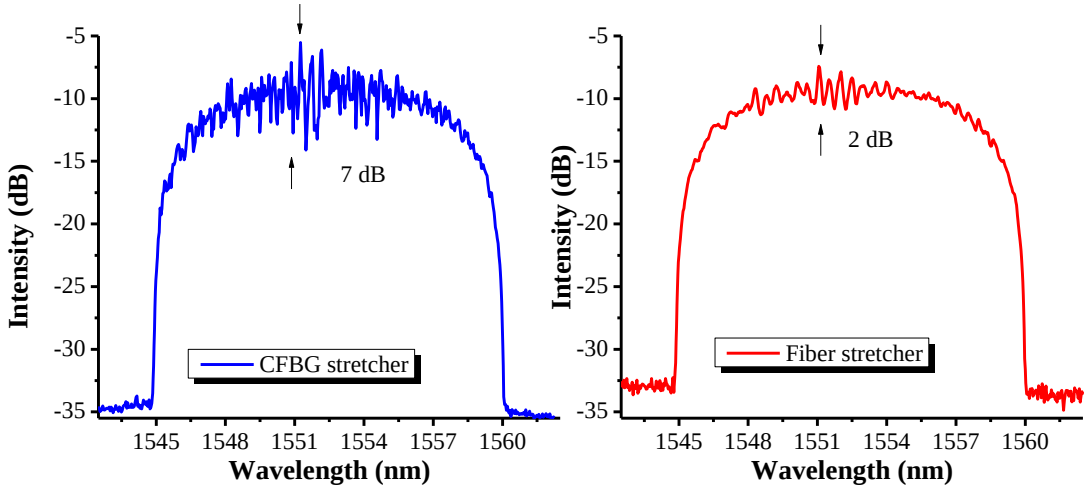

Figure 4-21. Parabolic optical spectrum after amplification (a) with CFBG stretcher (b) with fiber spool stretcher. Clearly the usage of fiber stretcher helps reducing spectral modulation by nonlinear SPM by at least 5 dB at 65 mW output power setting.

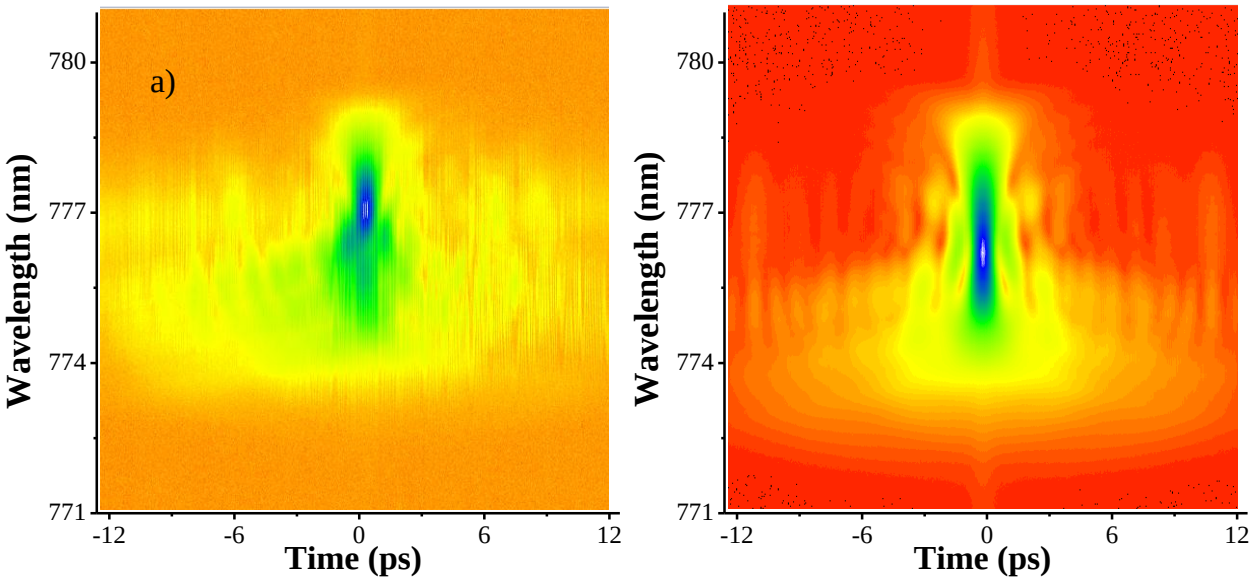

Figure 4-22. (a) Measured FROG spectrogram of CPA pulse only parabolic intensity shaping. The distortion of spectrogram symmetry is due to temperature fluctuation. (b) perfect spectrogram symmetry with implementation of thermal stabilization.

A 4-km long fiber stretcher was use, with a dispersion of D = 100ps/nm. The long fiber length is more vulnerable to temperature fluctuation; resulting to as much as 2 ps change in the overall total dispersion, causing distortion of the FROG spectrograms. The measured FROG spectrogram aftermath of changing stretching media clearly displays a substantial asymmetry in the temporal wings of the spectrogram. This indicates change of dispersion in the system over time. The FROG spectrograms in Figure 4-22 show the effect of temperature fluctuation over time. Without the protection of the thermal box, pulse width varies over a long period of time and subsequently causes distortion in the FROG spectrogram, with the assymetry clearly observed along the temporal coordinate (horizontal axis) in Figure 4-22(a). In the experiment,

this variation of pulse properties with time occurred over a period of 4 hours when the FROG spectrogram was being recoreded.

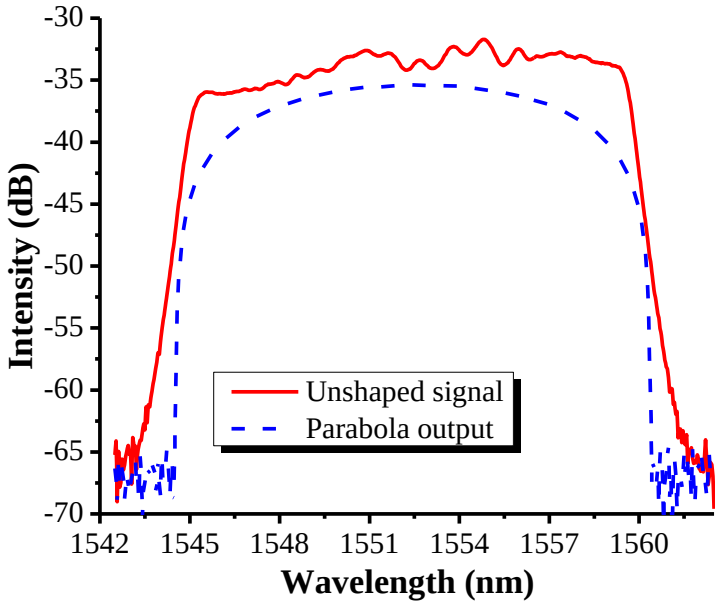

Figure 4-23. Optical spectrum of pulse without parabolic pulse shaping (solid) and parabolic output spectrum of pulse with intensity shaping (dashed).

To counter the effect of temperature fluctuation as well as acoustic and mechanical vibration, a closed thermal box (as shown in Figure 4-4) was constructed to isolate the CPA system from environmental change. This is the thermal isolation architecture developed and matured within our research group that has demonstrated its efficiency in shielding the laser systems from undesirable environmental effects such as mechanical vibration, thermal and

external acoustic noise. The laser is housed in the thermal box, which consists of 1 layer of styrofoam, 1 layer of cardboard, 1 layer of anti-vibration material, one special acoustic filtering layer, all enclosed in a hard Plexiglas case. By implementing thermal box to isolate the long fiber spool from temperature fluctuation of surrounding environment, spectrogram symmetry was achieved, as seen in Figure 4-22(b). Another approach to avoid the aforementioned problems, a fiber stretcher with minimal group delay ripple (GDR) could be used to circumvent the high frequency modulation on the optical intensity spectrum.

Using the pulse shaping procedure on CPA systems described previously, a spectral intensity mask was calculated and applied to the Finisar spectral processor. The parabolic optical intensity pulses generated were afterward amplified and compressed with the Treacy bulk compressor to achive high peak power. These compressed pulses were sent to the FROG to generate the spectrogram and eventually retrieve spectral phase information. The FROG spectrogram was generated by combining 1024 SHG optical traces at 48 fs delay interval. This phase information in turn was used to adjust the phase modulation applied to the Finisar spectral waveshaper to achieve pulses with linear spectral phase. The retrieval error of the FROG was 1.5E-3, showing very good convergence between FROG input and retrieval results

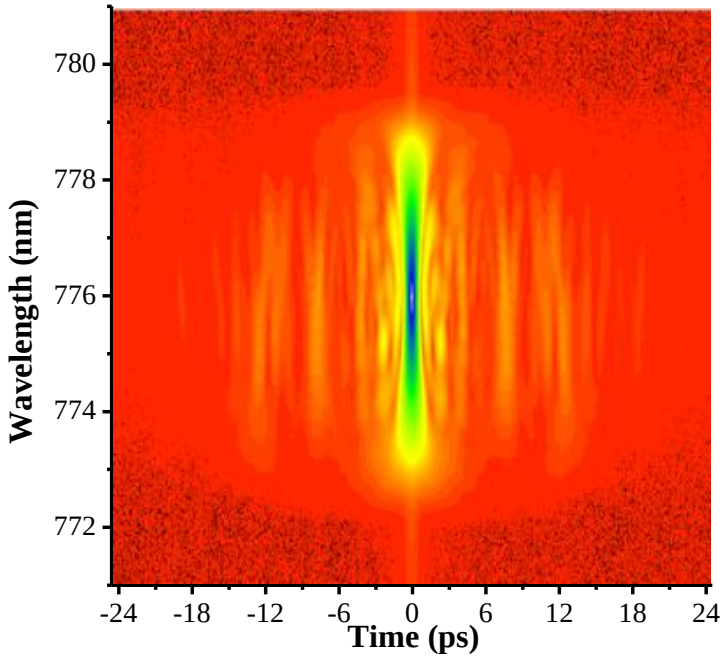

Figure 4-24. Experimental result of SHG-FROG spectrogram with both spectral phase and intensity modulation. The measured spectrogram matches the theoretical FROG spectrogram as shown in previous section very well.

In Figure 4-23, optical spectrum of pulse without parabolic pulse shaping is shown (solid), together with a typical parabolic output pulse (dashed). The output parabolic spectrum was designed to resemble output parabolic spectrum in CPA system with CFBG stretcher to facilitate comparison of two settings.

In Figure 4-24, the FROG spectrogram of pulses with parabolic pulse shaping is shown, with x-axis represents temporal coordinate, with 50 ps duration, and y-axis represents optical

wavelength, ranging from 771-781 nm. The spectrogram shows very good agreement with a typical simulation FROG spectrogram of chirp-free parabolic pulses, shown in Figure 4-17.

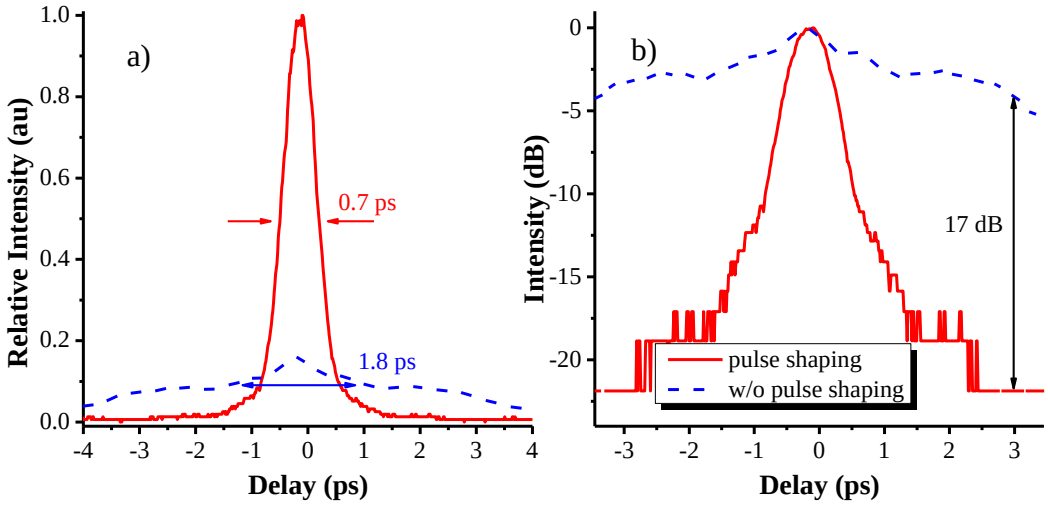

Figure 4-25. (a) Autocorrelation traces of pulses with spectral pulse shaping (solid) and without pulse shaping (dashed) in linear scale with normalized energy under curves, (b) replot of autocorrelation traces in logarithmic scale.

In Figure 4-25(a), autocorrelation traces of pulses with pulse shaping (solid) and without pulse shaping (dashed) are shown, with normalized energy under curves. The AC of pulses without pulse shaping has temporal width at FWHM of 1.8 ps, and is considerably shortened to 0.7 ps of pulses with pulse shaping. As with the case of CPA system using CFBG stretcher, clearly energy under the pedestals on the wings was transferred to the main peak, leading to an increase of 6.2 times in peak power. The graphs in Figure 4-25 (b) of autocorrelation traces plotted in logarithmic scale show 17 dB pedestal suppression on the wings of the autocorrelation

traces at 3 ps delay. This results show better compression of pulses and achieve higher increase in peak power compared to the CPA system with CFBG fiber stretcher.

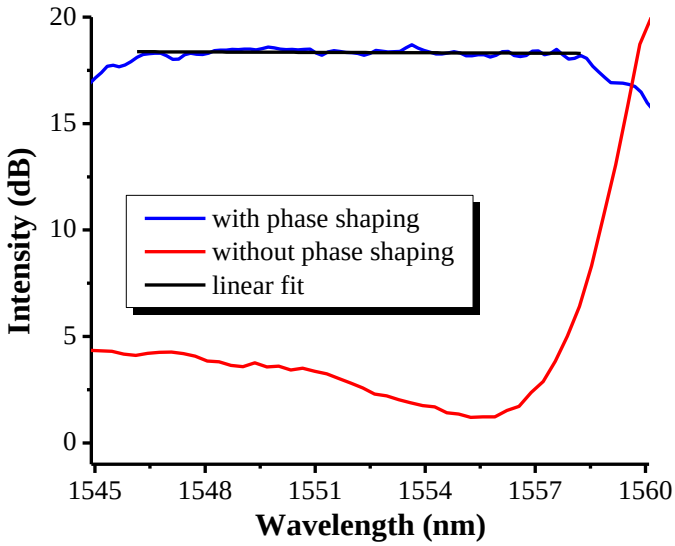

Figure 4-26. Reconstructed spectral phase with only spectral intensity modulation (solid), with both spectral intensity and intensity compensation (dashed), and its linear fit. The results again show almost perfect linear behavior of retrieved spectral phase near in the middle when phase compensation is applied, and higher deviation at the tails.

Figure 4-26 shows the retrieved spectral phase of the amplified pulse in the linear regime with and without phase modulation. The retrieved phase shows a deviation of 1.5 and 2.5 radians toward the left and right tail of the spectrum, respectively, flat phase across the center with 0.15 radians root mean square deviation. These results show 40% improvement of the linearity of

spectral phase over the results shown with CFBG stretcher, demonstrating the benefit of minimizing the group delay ripples (GDR) in CPA systems for optimal pulse compression.

4.5.3 Conclusions

In summary, we have demonstrated parabolic pulse shaping with both spectral intensity and spectra phase modulation in a CPA system. The use of SHG – FROG together with the spectral processor in an active feedback loop allows controlling of spectral phase and intensity modulation, resulting in high quality sub-picosecond pulses after compressing CPA pulses using a bulk grating compressor. The usage of the spectral waveshaper with versatile dispersion compensation capability immensely simplifies alignment requirement of the Treacy compressor to match the dispersion of the fiber stretcher. Using CFBG pulse stretcher, we achieved transform limited parabolic pulses of 0.7 ps temporal autocorrelation duration at FWHM, with linear spectral phase across the optical spectrum (1545 nm to 1560 nm) with 0.25 radians deviation. Measured autocorrelation traces show 5 times increase in peak power and 15 dB pedestal suppression on the wings at 3 ps delay. Similar results were achieved with a spool of dispersive fiber. A temporal autocorrelation trace with 0.7 ps width (FHMW), representing 6.2 times increase in peak power and 17 dB pedestal suppression at 3 ps delay was attained. The spectral phase retrieved by FROG software shows a linear spectral phase with 0.15 radians rms deviation. The consistency in these results confirms this approach as highly reliable, versatile, and can be readily applied to any existing CPA systems. This will be of significance in many CPA applications of fiber laser systems, allowing the generation of high quality ultrafast pulses

However, the FROG-based approach for phase retrieval in feedback loop is rather time intensive. To achieve transform limited pulses, three feedback loop iterations were performed. To ensure high resolution spectral phase profile, the spectrogram was constructed with 1024 traces, which cover the optical range of 776-786 nm of SHG signals. The data acquisition process takes approximately 3 hours, together with about 7 hours phase-retrieval data processing, resulting in on average 10 hours long process for a single iteration. This is a constrain in the ultimate goal of achieving real-time control feedback loop. The following section describes a high precision characterization of the spectral phase of the fiber CPA laser system, which was essential in the laser development. This approach is a well-known technique, promising a fast, reliable and accurate measure of spectral phase comparable to the FROG approach.

CHAPTER 5: MACH-ZEHNDER INTERFEROMETRIC SPECTRAL PHASE CHARACTERIZATION

5.1 Introduction

Fiber based chirped pulse amplification (CPA) systems have generated great interest because of their ability to amplify ultrafast pulses to energy comparable to conventional bulk solid-state systems, while offering significant advantages, such as compactness, simplification of components, and freedom of alignment. Optical pulses with parabolic temporal intensity profile are of much practical significant for CPA systems because of their intrinsic resistance to optical wave breaking, ability to retain their intensity profile during propagation in gain media, and enhanced linearity in chirp, therefore allows the scaling of fiber amplifiers to higher energy regimes. Their linear chirp also allows efficient and high quality pulse compression. Consequently, parabolic pulse generation has attracted much attention, and pulse shaping approach involving a dynamic technique to control spectral intensity as well as spectral phase utilizing an active feedback loop has been reported recently [78].

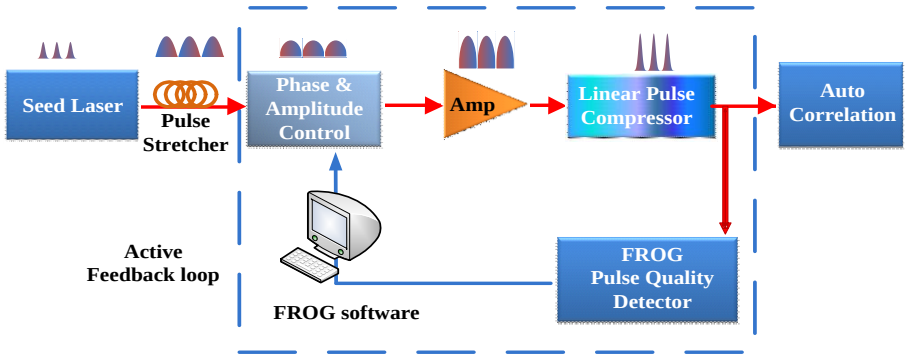

Figure 5-1. Block diagram of chirped pulse amplification setup. Amp: optical amplifier; AOM: acousto-optic modulator; Finisar: waveshaper; LPF: low pass filter; f/N: frequency divider; RFAmp: RF amplifier; SG: signal generator, Driver: AOM driver. The dash box is the seed laser for the Finisar spectral processor

In this setup, the use of second harmonic generation frequency resolved optical gating (SHG-FROG) in conjunction with the Liquid Crystal on Silicon (LCOS) waveshaper in the active feedback loop allows dynamic control of spectral phase and intensity modulation, resulting in transform limited parabolic pulses of 0.7 ps temporal duration after compression, and five time increase in peak power.

The implementation of the second harmonic generation frequency resolved optical gating (FROG) [57,70,79] is instrumental to analyse the quality of the pulses in terms of their temporal duration, intensity and spectral frequency, and to retrieve spectral phase of the pulses. This information is directed to an adaptive feedback loop to dynamically modify the pulse shaping parameters in the Finisar spectral processor, based on the input profiles and the retrieval information from the FROG, to produce high quality pulses..

However, this phase retrieval approach using FROG is rather time intensive. On average, the feedback iteration takes about 10 hours to complete. The use of the FROG adds to the cost of the pulse shaping systems as well as increasing the overall volume of the CPA setup. Here we propose and devise a different approach for spectral phase retrieval. This approach must be cost effective, time efficient and has a small footprint. And it's important that this approach allows us to achieve equivalent pulse quality as the FROG approach for our CPA system.

In the following sections, a brief description of experimental setup and procedure are shown. We will present results of phase retrieval using spectral interferometry (SI) approach, followed by a summary and conclusion. Spectral interferometry approach using interference of two beams in a standard Michelson or Mach-Zehnder interferometer has been widely used in a variety of research areas, such as laser ranging, material characterization and optical communications. It has also become a very useful tool in fiber-based sensing.

5.2 Spectral Interferometry

The intensity profile of the optical spectrum of a signal, such as an ultrashort pulse, can be measured easily using an optical spectrum analyzer (OSA), or spectrometer. However, the task of measuring optical spectral phase is much more difficult, and can either be performed using nonlinear or linear approach. One such linear measurement technique is Fourier transform spectral interferometry, or frequency domain interferometry, which has the potential to provide fast, accurate and at the same time guarantees high quality measurements. In this approach, a

typical Mach-Zehnder interferometer is employed to combine two pulses, and the resulting interference spectrum is recorded with an OSA, or spectrometer. The optical path length of the two pulses is carefully monitored so that one of the pulses is subjected to a small time delay τ, so that the combined electric field is $E(\omega) = E_1(\omega) + E_2(\omega)e^{i\omega\tau}$, resulting in the modulation of the combined field.

5.2.1 Reference pulse for spectral retrieval

In order to measure the ultrashort pulse, a well-defined source of the reference beam is required, the spectrum of which covers the full range of the pulse to be characterized. This can be achieved by either use a relevant, well characterized pulse, or a heterodyne approach, with the reference pulses from the same source, albeit with lower pulse energy than pulses from CPA arm.

5.2.1.1 **Spectral shearing interferometry**

A well-known approach for obtaining a reference pulse is accomplished by sending a pulse from the same laser source through a sinusoidally modulated phase modulator at a time close to the zero crossing of the phase. In this approach, an arm of the Mach-Zehnder interferometer contains an electro-optic phase modulator, the nearly linear phase modulation then corresponds to the spectral shift of magnitude $\delta\omega$. The spectrum of the combined pulses then has a modulation phase

$$\varphi(\omega) = \varphi_1(\omega + \delta\omega) - \omega\tau \approx \frac{\delta\varphi_1}{\delta\omega}\delta\omega + \omega\tau \tag{5.1}$$

where the approximate relation holds if $\delta\omega$ is not too large. This shows that the spectral derivative of the phase of the signal pulse can be obtained, which is the frequency-dependent group delay.

This method is called *spectral shearing interferometry* [80–82], and it works well for relatively long pulses. For very short pulses, where the group delay variation within the pulse duration is small, it is difficult to obtain a sufficiently large spectral shift in the modulator. A larger spectral shear can be achieved by using a nonlinear interaction, as discussed in the following section

5.2.1.2 **Spectral phase interferometry for direct electric field reconstruction**

Another method of spectral shearing interferometry, often applied for the complete characterization of ultrashort pulses, is called Frequency Resolved Optical Gating (FROG) [57,70,83]. Here, the signal pulse is split into two identical copies with a significant temporal distance, so that there is no temporal overlap. Another pulse, derived from the same input pulse, is strongly temporally broadened by sending it through a highly dispersive optical element, such as a long block of glass or a pair of diffraction gratings.

The long chirped pulse and the two copies of the signal pulse are then combined in a nonlinear crystal, where sum frequency generation occurs (see Figure). The two signal pulses overlap with different temporal portions of the chirped pulse, which have different optical frequencies, so that there is also a spectral shear between the two upconverted pulses. Therefore, the optical spectrum of the sum frequency signal reveals the temporally resolved group delay in a way which is analogous to that discussed above. From the group delay, it is easy to retrieve the frequency-dependent spectral phase, so that complete pulse characterization is achieved.

The FROG method offers various advantages:

- The FROG algorithm has the advantage of delivering additional consistency checks.
- The method can be applied also for very short pulses with durations below 10 fs. FROG relies on the accurate calibration of the spectrometer in a wide wavelength range. However, it may anyway be desirable to know the spectrum precisely for calibration.
- For long pulses, FROG is convenient, and doesn't require a spectrometer with very high resolution, and an optical element with a huge amount of chromatic dispersion.
- The method has variants which allow for single-shot measurements.

A comprehensive comparison of SPIDER and FROG techniques is difficult, because there are many variants of both methods, which have specific advantages under certain circumstances.

5.3 Experimental Setup

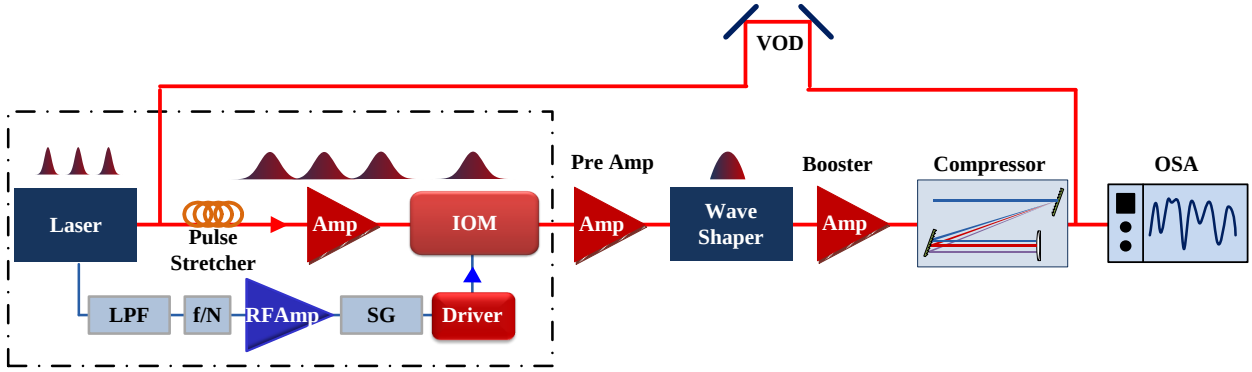

Figure 5-2 Block diagram of spectral interferometry setup for a chirped pulse amplification system. Amp: optical amplifier; IM: intensity modulator; Finisar: waveshaper; LPF: low pass filter; f/N: frequency divider; RFAmp: RF amplifier; SG: signal generator, Driver: AOM driver, OSA: optical spectrum analyzer, VOA: variable optical delay. The dash box is the seed laser for the Finisar spectral processor

The schematic of this CPA system is shown in Figure 5-2. A Calmar seed laser was used o generate pulses at 1552 nm at 20 MHz repetition rate with a full width half max (FWMH) optical bandwidth of ~10 nm. The pulses are temporally stretched using a polarization maintainig (PM) fiber stretcher with a dispersion of 100 ps/nm, resulting in a linear frequency chirp across the pulses. After stretching, pulses are amplified with an optical amplifier.

An $LiNbO_3$ Intensity Modulator (IM), combined with a RF driver, is employed to frequency-select the pulse train to a lower frequency. The IM has an extinction ratio of approximately 25 dB, as contrast to the extinction ratio of an Acousto-optic modulator (AOM) of over 40 dB. However, using AOM would cause a frequency shift in axial modes of the laser

corresponding to the driving frequency of the AOM of about 200 MHz. This frequency shift effectively renders laser beams from two arm incoherent with each other, and no interference fringes would be observed on the OSA.

After frequency selection, a second optical amplifier is used to amplify the pulse train. The RF signal from Calmar laser is injected into a 20 MHz low pass filter (LPF) to select the first 20 MHz tone. A frequency divider is used after the LPF to down convert the frequency of RF signal from 20 MHz to 1.25 MHz, followed by amplification with an RF amplifier, before being used to trigger the signal generator. The signal generator produces a square gating signal to modulate the 200 MHz carrier frequency signal from the AOM driver. This signal is applied to the AOM, resulting in an output pulse train with the desired repetition rate. Throughout the operation, to ensure the AOM operating at minimum transmission when the gate signal is not applied, a DC voltage is applied to the AOM.

A Finisar spectral processor, which utilizes Liquid Crystal on Silicon (LCOS) technology, is used to shape the stretched pulses to produce a parabolic temporal intensity profile. Due to frequency to time mapping property of extremely stretched pulse [53], the temporal profile of output pulse after pulse shaping, as seen in sampling scope, resembles the pulse optical spectrum and also assumes parabolic shape. After pulse shaping, an optical amplifier is used to amplify the pulses. A Treacy grating pair [66] is used to compress the amplified pulses to attain high peak power.

To determine the spectral phase in the CPA laser, we use the spectral interferometry approach. A typical Mach-Zehnder interferometer will be used to perform spectral interference

measurements[1,2] [84]. The laser source signal is split into two arms, one containing the CPA setup, and the other containing a variable optical delay (VOD). The VOD is used to balance length of two arms, as well as to introduce a small path length difference between the two interferometer arms. The spectral interferometry approach simply involves measuring the spectrum of the sum of two pulses, which yields the phase difference between the two arms. Since the laser source is transform limited, the spectral phase from the delay arm is linear, therefore spectral phase of the CPA system is the phase difference between the two arms.

Mathematically, the sum of the two pulses can be expressed as:

$$I(\omega) = (E_1(\omega)e^{i\phi_D(\omega)} + E_2(\omega)e^{i\phi_L(\omega)})(E_1(\omega)e^{-i\phi_D(\omega)} + E_2(\omega)e^{-i\phi_L(\omega)}) \tag{5.2}$$

$$= {E_1}^2(\omega) + E_1(\omega)E_2e^{i(\phi_D(\omega)-\phi_L(\omega))} + E_1(\omega)E_2e^{-i(\phi_D(\omega)-\phi_L(\omega))} +$$

$${E_2}^2(\omega)$$

where and $\Phi_L(\omega)$ is the resultant phase excursion after transmission through the CPA laser system. Similarly, $\Phi_D(\omega) = \omega\tau$ is resultant phase of the electric field after travelling an additional distance in the VOD. Eq (1) can be simplified to:

[1] Germain Chartier, Chapter 6, "Introduction to optics", Springer Science+Business Media, Inc, (2005)
[2] Dennis Derickson, Chapter 10, "Fiber optic test and measurement", Prentice-Hall, Inc (1998)

$$I(\omega) = I_1(\omega) + 2I_1I_2(\omega)\cos\big(\phi_D(\omega) - \phi_L(\omega)\big) + I_2(\omega) \quad (5.3)$$

With $I_1(\omega) = {E_1}^2(\omega)$, and $I_2(\omega) = {E_2}^2(\omega)$, are the spectra of the reference (delay) arm and the CPA arm. Spectral interference with periodic fringes will be observed on the OSA due to the linear phase modulation across the optical spectrum. By blocking the CPA arm of the interferometer, the spectral intensity of the light source $I_1(\omega)$ can be obtained. Similarly, by blocking the delay arm, the term $I_2(\omega)$can be determined. The cross-term $2I_1I_2(\omega)\cos\big(\phi_D(\omega) - \phi_L(\omega)\big)$ can then be used to obtain information about the phase $\Phi_L(\omega)$. The spectrum is easily extracted using a well-known fringe-inversion technique[3]. If the VOD is not changed during an experiment, the $\phi_D(\omega)$ term can be considered constant, and therefore does not needed to be independently measured, except to determine its sign to avoid ambiguity in the sign of cosine argument. The experiment can be repeated with different phase delays to validate retrieved spectral phase.

The signal recorded as the function of time delay τ between two arms is well known to be the first order autocorrelation of the incident electric field whose Fourier transform is the power spectrum. This result is the basis of Fourier transform spectroscopy, a standard technique regularly used in the infrared spectral domain. The spectral interferometry technique was introduced by Froehly and coworkers in 1973. The spectral fringes of the interference signal is

[3] S. Kujawinska, "Interferogram Analysis", D.W. Robinson and G.T. Reid, eds (Institute of Physics, Bristol, UK, 1993), pp 141-193.

inversely proportional to the optical path difference between two beams, which in turns depends on the phase difference. One big advantage of using spectral interferometry method is that the spectral interferogram can be recorded simultaneously by using either photography or a multichannel analyzer, such as a CCD detector or OSA. Unlike in time-domain interferometry, small fluctuations of the optical path length do not invalidate the interferogram, although they do reduce the fringe contrast if the time scale is shorter than the exposure time.

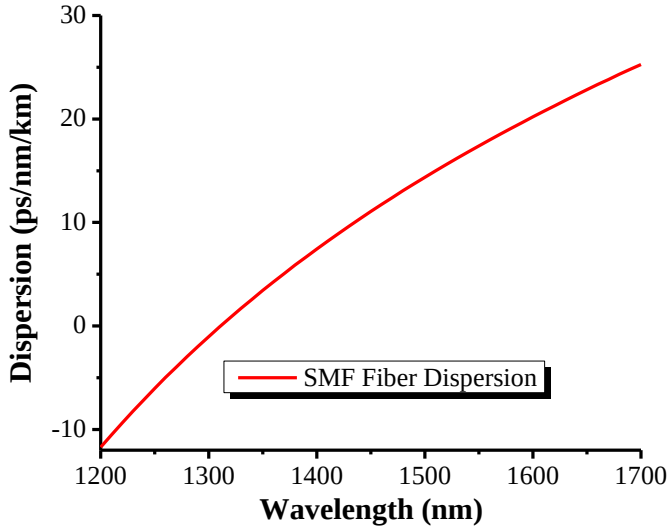

Figure 5-3 Calculated dispersion curve of typical Corning-SMF-28 fiber, with zero-dispersion at 1310 nm. The dispersion is calculated for range from 1200 nm to 1700 nm, which is the typical operating range for light in single mode fiber.

Let's first consider non-dispersion shifted single mode fiber (SMF) used in the experiment, such as Corning SMF-28 single mode fiber. Approximately 100 m of SMF fiber in reference arm is required to balance the length of two arms of the interferometer. This fiber has zero-dispersion wavelength at between 1301 and 1321 nm. However, at zero-dispersion wavelength, the attenuation is rather high, approximately 0.5 dB/km. This attenuation limits transmission distance and increase loss in the laser systems; therefore it's more desirable to operate at the C-band where attenuation is smaller, approximately 0.1-02 dB/km.

The dispersion of the SMF-28 as a function of the wavelength

$$D = \frac{s_o}{4}\left(\lambda - \frac{{\lambda_o}^4}{\lambda^3}\right) \text{ or } D = 2(B\lambda + C\lambda^{-3}) \tag{5.4}$$

With s_o = 0.092 ps/nm/km is the slope of zero dispersion at λo = 1310 nm for SMF-28 fiber, so $B = {s_o}/{8}$ and $C = {s_o {\lambda_o}^4}/{8}$

Approximately the group delay

$$T = (B\lambda^2 + C\lambda^{-2}) \tag{5.5}$$

Knowing

$$T = \frac{\partial \varphi}{\partial \omega} \tag{5.6}$$

Consequently phase excursion

$$\varphi = \int T d\omega = \int (B\lambda^2 + C\lambda^{-2})\, d\omega = \int \left(B\left(\frac{2\pi c}{\omega}\right)^2 + C\left(\frac{2\pi c}{\omega}\right)^{-2} \right) d\omega \tag{5.7}$$

$$\varphi(\omega) = -B\frac{(2\pi c)^2}{\omega} + \frac{C\omega^3}{3(2\pi c)^2} \tag{5.8}$$

Spectral phase is the phase difference between two arms, which can be extracted by Fourier transforming the spectrum, filtering out the negative and zero-frequency components, frequency shifting the positive frequency component to DC (to remove the delay term), and inverse Fourier transforming back to the frequency domain. The phase of the resulting spectrum is then the phase difference between the reference $\phi_D(\omega)$ and the phase $\phi_L(\omega)$ of the CPA arm, with the value of $\phi_D(\omega)$ calculated above to avoid ambiguity in the sign of cosine argument. The experiment can be repeated with different phase delays to validate retrieved spectral phase.

5.4 Experimental Results

In the first setup, a fiberized CFBG was used as the temporal pulse stretcher. The length of the fiber CFBG is approximately 1 meter, and is suitable for reducing the physical footprint of CPA systems. The short length of the fiber CFBG also makes it much less susceptible to fluctuations in environmental temperature.

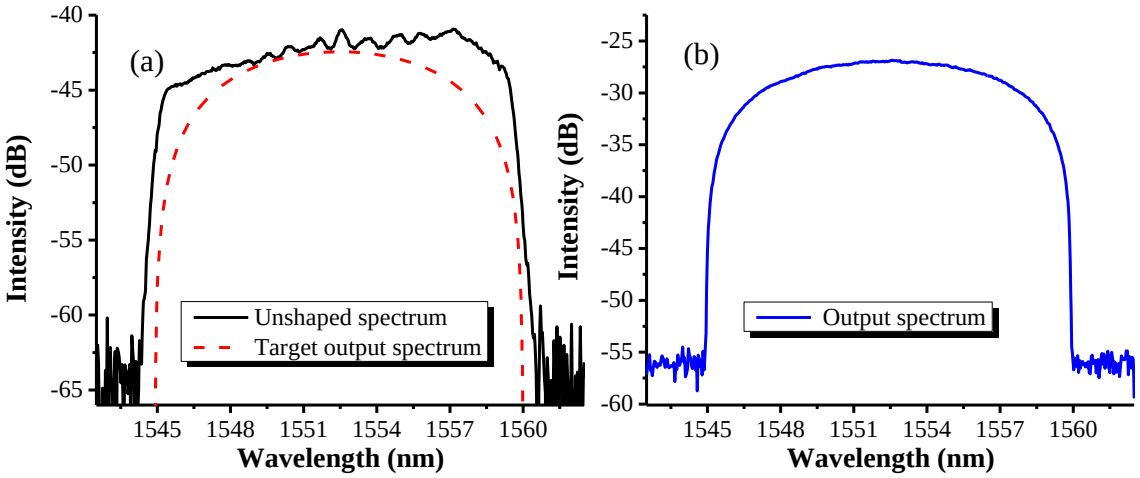

Figure 5-4. Optical spectrum without pulse shaping (solid) and desired parabolic output spectrum (dashed) (b) Typical parabolic optical spectrum generated with the spectral processor. The output spectrum has signal to noise ratio of ~28 dB measured from the maximum of the intensity profile to background noise.

Initially, only spectral intensity modulation was applied to the input pulses. A spectral intensity mask was generated by taking the difference between input spectrum and the desired target output spectrum seen in Figure 5-4 (a). This mask was applied to the Finisar spectral processor to produce the desired parabolic optical intensity shape. These output pulses have 15 nm optical bandwidth at 10 dB, centered around 1552.5 nm and have temporal width of 1.4 ps.

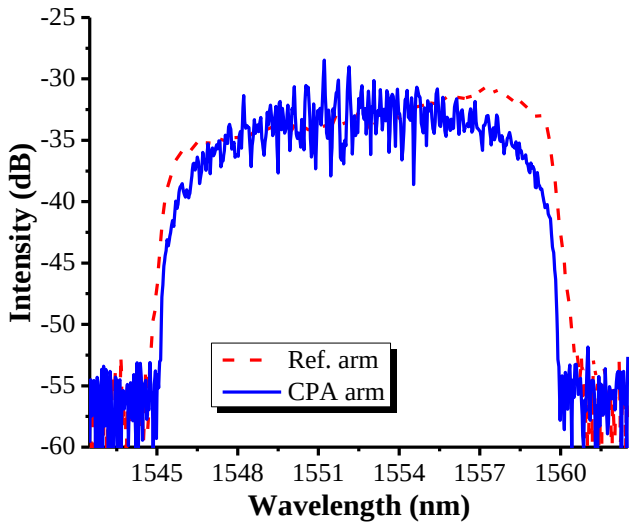

Figure 5-5. Optical spectra of pulses in CPA arm and reference arm. Pulse spectrum in CPA arm has parabolic shape, resulting from the intensity modulation performed at the Finisar spectral processor. However, as the pulses after shaping are amplified to high power, due to low repetition rate and long fiber length of the CPA arm as well as the optical amplifier, nonlinearity caused intensity modulation observed on the amplified spectrum. This modulation is periodic, indicating the presence of SPM.

The output parabolic pulses after intensity shaping, in Figure 5-4 (b), were amplified before being compressed with the bulk compressor. Due to high power setting, there will be intensity modulation as seen on amplified spectrum in Figure 5-5. This pulse is used to interfere with pulse from reference arm. The resultant interference spectrum can be seen in Figure 5-6. To maximize the depth of interference fringes as well as avoiding SPM due to high peak power, power of pulses in CPA is attenuated to match pulse power in reference arm using a bending optical attenuator. A polarization controller is utilized to ensure the same polarization in both arms.

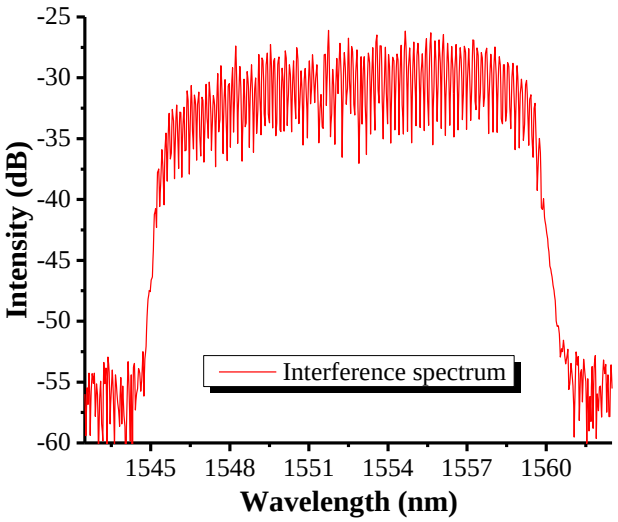

Figure 5-6. Typical spectral interferogram of parabolic optical pulses generated with the spectral processor and reference pulses

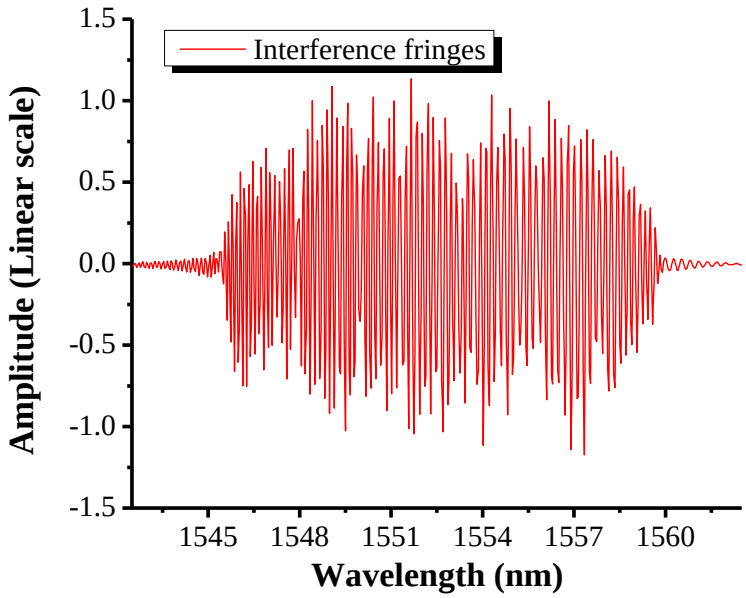

Figure 5-7. Typical spectral interference fringes

In Figure 5-7, interference fringes of SI approach is plotted in linear scale. This interference fringes is obtained by subtracting the spectrum of reference arm and CPA arm from the spectral interferogram in Figure 5-6. To implement fast Fourier transform for phase retrieval, the spacing and the number of points in which the spectrum is measured is set to be 1024. Afterward, the standard Fourier transform spectroscopy technique is implemented to retrieve spectral phase difference between two arms.

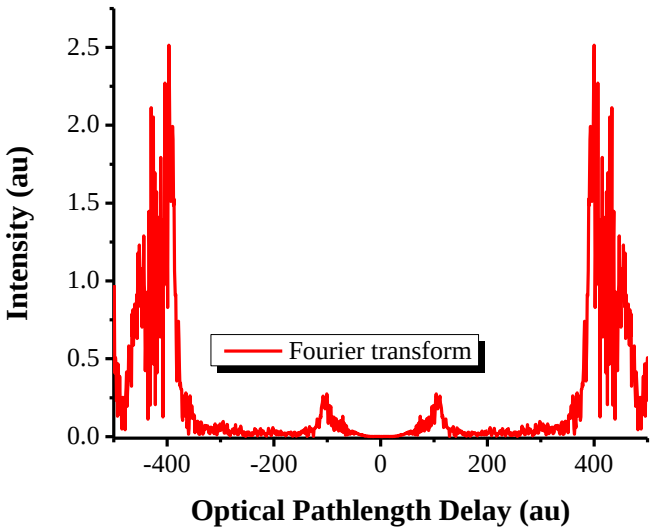

Figure 5-8. Fast-Fourier-transform (FFT) of the interference fringes.

In Figure 5-8 the Fourier transform of the interference fringes shown in Figure 5-7 is shown. This graph shows symmetric behavior, typical for the Fast Fourier transform operation; therefore only half the graph is sufficient to provide the information of the spectral phase. This data will be used in the inverse Fourier transform to retrieve spectral phase difference between

the two arms of the Mach-Zehnder interferometer. Physically changing the optical path length difference between the two arms by adjusting the variable optical delay will result in shifting the plot closer or further from DC in this graph.

If pulses from two arms have the same (or no) chirp, then the interference pattern will show a perfect sinusoidal function, with the frequency of the function inversely proportional to the time delay (or optical path length) between pulses. The resultant Fourier transform of that interference fringes will be the Fourier transform of a sinusoidal function, which is a delta function. However, when there is chirp presence, the delta function broadens accordingly to the complexity of the chirp, as seen in Figure 5-8, and chirp information can be obtained by performing inverse Fourier transform

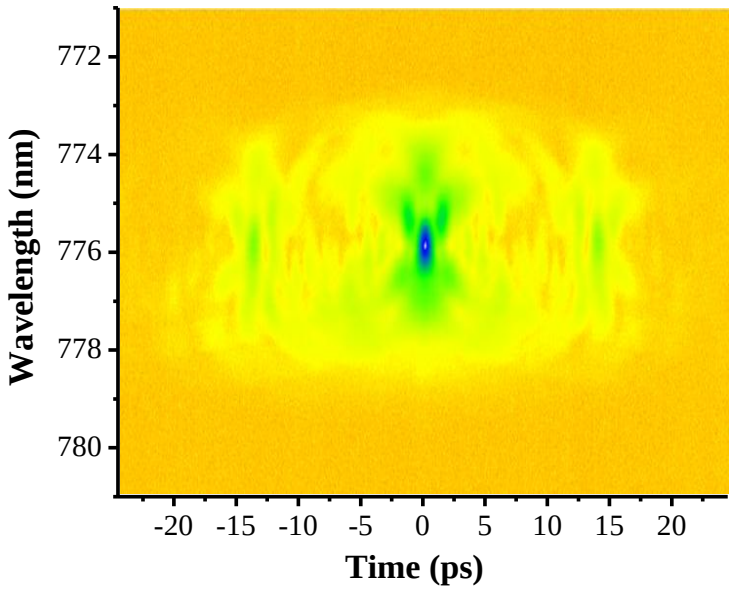

Figure 5-9. Measured FROG spectrogram of CPA pulse without phase compensation. Notice the significant smear out from the zero-delay central pulse, as well as the green structures at ~12 ps delay, corresponding to the satellite pulses seen in autocorrelation trace plot.

To validate spectral phase retrieval using SI approach, the FROG-based phase retrieval is used for comparison. A FROG spectrogram was constructed by collecting 1024 FROG traces by gradually varying the arrival time difference of the two pulses on two arms of the FROG, with delay setting at 48 fs between traces. A commercial FROG software, which implements an iterative phase retrieval algorithm, was used to reconstruct the pulse shape from the FROG spectrogram. The retrieval error of the retrieval procedure was on the order of 2.5E-3, showing a very good convergence. In Figure 5-9, the FROG spectrogram of parabolic pulses without phase

compensation is shown. In this figure, the green wings indicate the presence of chirp, or higher order dispersion.

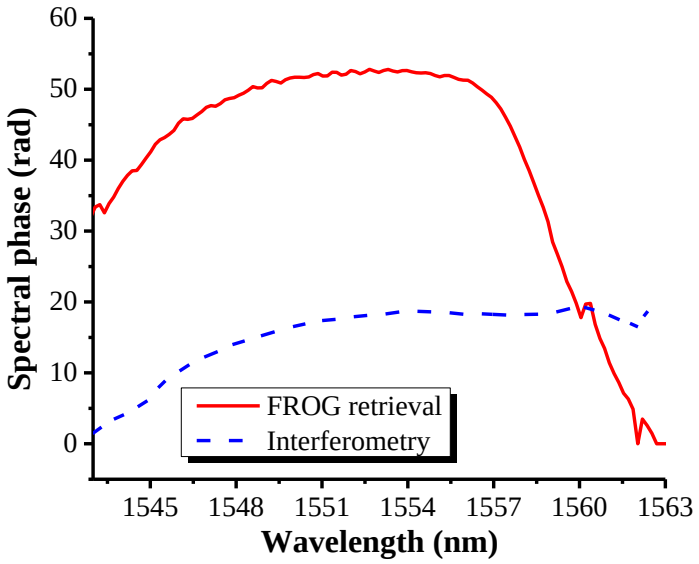

Figure 5-10. Reconstructed spectral phase using spectral interferometry approach (dashed) and FROG approach (solid). The shape and amplitude of these two spectral phases match very well within 1545-1558 range, and less well at the red (longer) wavelength.

To retrieve spectral phase of pulse, inverse Fourier transforming back to the frequency domain was performed. In Figure 5-10, the retrieved spectral phase using SI approach is plotted, together with spectral phase retrieved with the FROG. The retrieved spectra show remarkable agreement, with about 30 radians offset, ranging from 1542-1558 nm. Moreover, the Matlab-based phase retrieval code used to calculate spectral phase has a significant time advantage over

the FROG-based approach, with only 10 minutes long procedure, in comparison with FROG-spectrogram generation and phase retrieval of about 10 hours. Consequently, the SI phase retrieval approach brings up the prospect of real time pulse monitoring and shaping for CPA systems. The faster retrieval time also allows multiple feedback loops to be performed, potentially improve pulses quality and pulses width to theoretically transform limited.

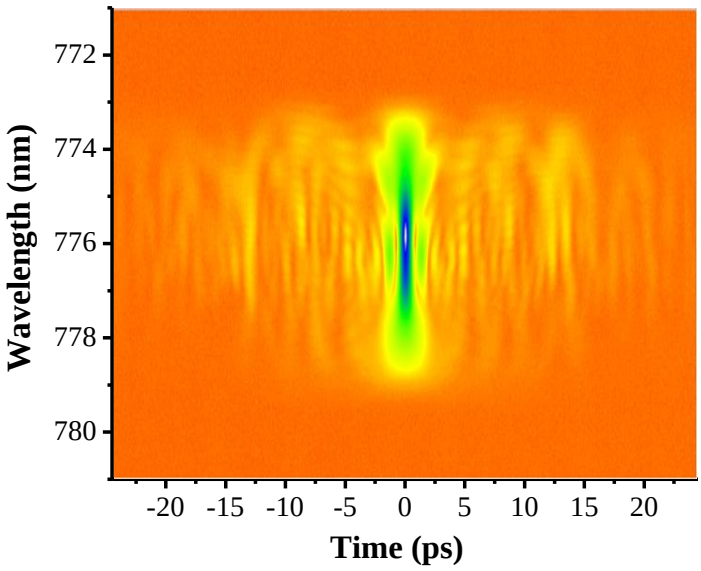

Figure 5-11. Measured FROG spectrogram of CPA pulse with phase compensation. The spectrogram is constructed with 1024 FROG traces, with total time delay of about 24.5 ps and optical range of 10 nm, from 771-781 nm.

The spectral phase from Figure 5-10 using SI approach is fed back to the Finisar waveshaper to adjust spectral phase compensation. Figure 5-11 shows the measured FROG spectrogram of parabolic CPA pulses after phase compensation. The shape of the experimental

FROG spectrogram in Figure 5-11 is strikingly similar to the expected FROG spectrogram of a chirp free parabolic pulse, with significant reduction in the temporal wings.

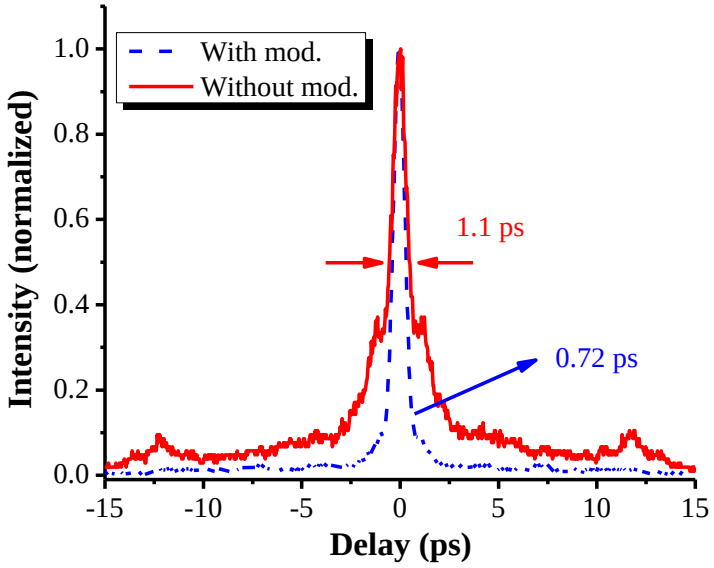

Figure 5-12. Measured AC trace of a phase compensated pulse (blue-dashed), in comparison with an AC trace of CPA pulses with only parabolic intensity modulation (red-solid) in linear scale, with temporal intensity normalized to unity. Notice the occurrence of pedestals at 13 ps delay at both AC traces before and after phase compensation, indicating the presence of satellite pulses, which can't be compensated by changing dispersion.

The contour of the retrieved spectral phase using spectral interferometry approach follows the contour of the FROG-based retrieval phase, with about 35 radians offset. The right wing of the spectral phase however doesn't match, that could be attributed to the lack of interferometry information at wavelength longer than 1557 nm, as seen in Figure 5-7. Since the SHG is a nonlinear optical phenomenon, the intensity, or amplitude of the SHG signal strongly

correlates to the peak power of the input pulses. The contrast in background of the FROG spectrograms in Figure 5-11 with the background of the FROG spectrogram in Figure 5-9 implied substantial increase in peak power of pulses after phase compensation.

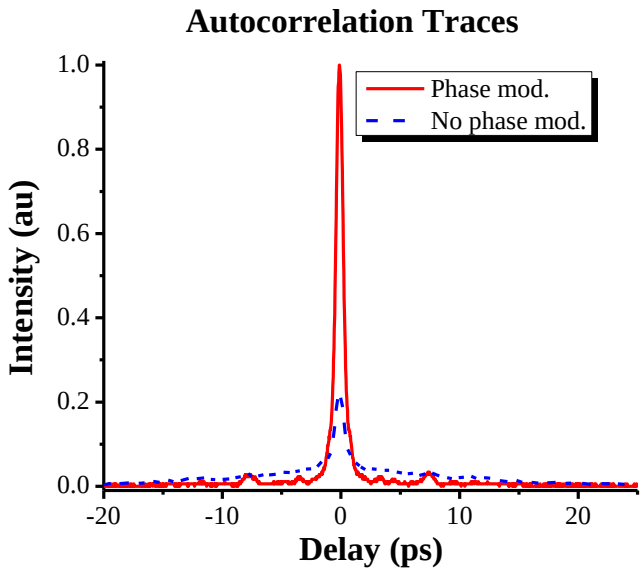

Figure 5-13. Measured AC trace of a phase compensated pulse (dash), in comparison with an AC trace of CPA pulses without phase compensation (solid) in linear scale, with temporal intensity normalized to unity

In Figure 5-12, the measured autocorrelation trace of pulse without phase compensation is shown (solid) with temporal duration of 1.1 ps at FWHM, with the amplitude of autocorrelation traces normalized to unity. After phase compensation, a 0.72 ps temporal duration autocorrelation trace (dashed) was achieved. This measured autocorrelation trace shows very good agreement with a calculated autocorrelation trace of transform-limited pulses with the

same parabolic optical spectrum of 0.7 ps. It should be noted that the pedestals in temporal profile of a CPA pulse without phase compensation have been well suppressed by 13 ps delay.

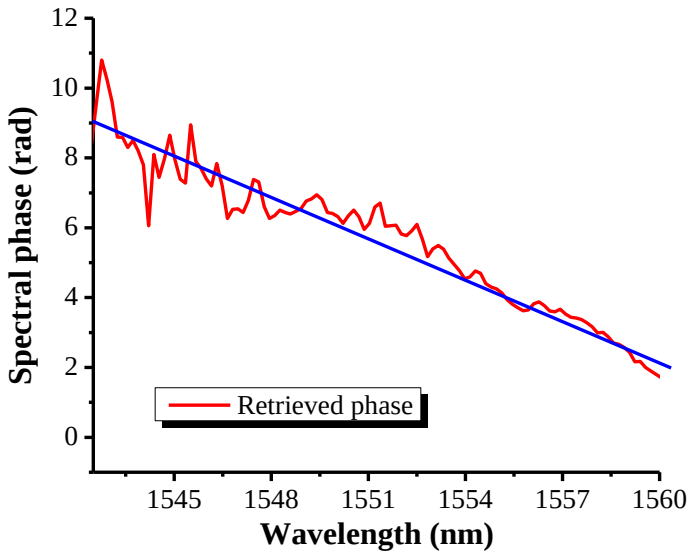

Figure 5-14. Reconstructed spectral phase of parabolic pulses with both spectral intensity and spectral phase modulation. The graph shows very good linear trend of spectral phase, compared with a linear fit (solid blue), indicating good spectral phase compensation.

In Figure 5-13, the autocorrelation traces are renormalized and re-plotted, with respect to power under curves. These results clearly show that a substantial amount of energy under the pedestals on the wings has been transferred to the central lobe, significantly increases pulse peak power. The relative intensity of the autocorrelation trace of pulse before phase compensation is approximately 0.22, indicating a 4.5 fold increase in peak power. In this figure, the pedestals occur at 13 ps delay, these pedestals appears on both autocorrelation traces before and after

phase compensation, indicating the presence of satellite pulses. These satellite pulses could be the results of a local Fabrey-Perrot oscillator, or pulse reflection within the laser system.

In Figure 5-14, the reconstructed spectral phase of parabolic pulses after phase compensation is plotted. After pulse shaping, the retrieved spectral phase of pulses with pulse shaping is shown in blue. The linear fit of the retrieved spectral phase indicates a 0.45 radians root mean square deviation over the whole optical spectrum of the pulse.

5.5 Summary and Discussion

In summary, we have demonstrated a spectral interferometry (SI) approach to measure spectral phase of our CPA system. This SI approach appears to be an excellent method because of its simplicity, small footprint, low cost and time efficient. And yet this approach allows the generation of high quality CPA pulses comparable to the FROG-based feedback loop approach. This approach allows the portability of the CPA systems by bypassing the use of the FROG as well as enables real-time pulse monitoring and adjusting. Using SI spectral phase retrieval for our feedback loop, we achieved near transform limited parabolic pulses of 0.74 ps temporal autocorrelation duration at FWHM, with fairly linear spectral phase across the optical spectrum (1545 nm to 1560 nm). By suppressing the temporal pedestals, energy under temporal pedestal was transferred to the central peak, resulting in 4.5 times increase in peak power. The time duration for this spectral interferometry approach is on the order of 10 minutes, that's 60-fold improvement over the FROG-phase retrieval approach. The consistency of the pulse spectrogram

with this technique and the FROG approach confirms this approach as highly reliable, can be readily adapted to any existing CPA systems.

Several improvements however can still be implemented.

The spectral phase retrieval approach gives the phase difference between two arms of the Mach-Zehnder interferometer. Therefore in order to successfully measure and compensate for the accumulate phase in the CPA system, it's very important for the seed laser to be chirp-free, as the quality of the pulse after compensation will be limited by the seed laser, and the measured spectral phase with interferometry will only reflect the phase accumulation in the CPA. The pulse picking operation (or frequency selection down) from 20 MHz to 1.25 MHz was performed with an EOM instead of an AOM. This was done to avoid frequency shifting of the axial modes of the pulse in the CPA arm with respect to the pulse in the reference arm, and consequently would render laser beams from two arms incoherent for interference purpose.

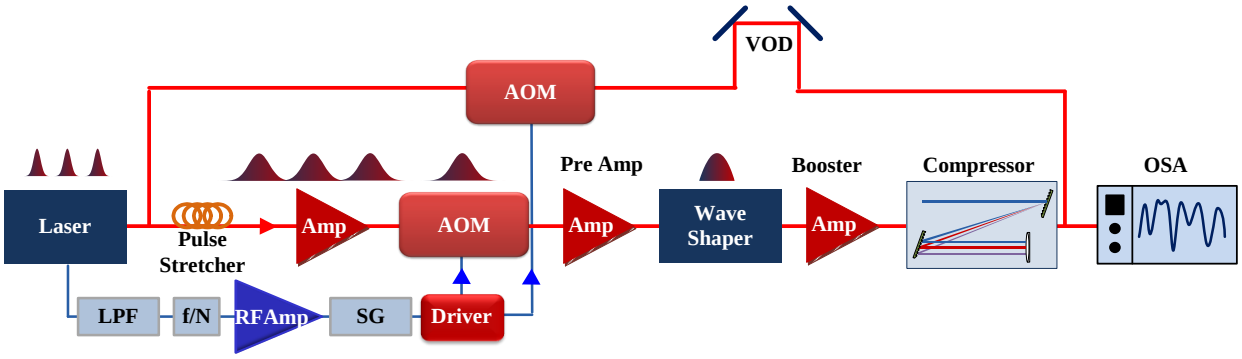

Figure 5-15. Block diagram of spectral interferometry setup for a chirped pulse amplification system with AOM on both arms. The signal generator produces a square gating signal to modulate the 200 MHz carrier frequency signal from the AOM driver. The RF driver sends out sinusoidal

signal of 200 MHz to drive the AOM modulators. The AOM on the reference arm is used to shift axial modes of pulses to the same amount of the CPA arm.

However, the EOM have much smaller extinction ratio of around 24 dB compared to an extinction ratio of approximately 45 dB of an AOM. This would eventually lead to increasing noise of the interference measurement. One possible approach avoid this issue is to use two AOM intensity modulators in both arms of the Mach-Zehnder interferometer, driven with the same RF drive source so the frequency shifting of the axial modes in two arm would be identical. The sketch of this setup can be seen in Figure 5-15**.** The use of the AOM in the CPA arm would reduce leak and subsequently improve the contrast of signal to noise.

The repetition rate of the laser in the reference arm is 20 MHz, corresponds to a 50 ns time period, or ~10 m of optical path length in fiber. In the CPA arm, due to frequency selection down to 1.25 MHz, the time separation between pulses is 800 ns, or approximately 160 m of optical path length. In order to balance the optical path length of the two arms of the Mach-Zehnder, a 110 m fiber spool was added to the reference arm. The coherent length of a transform limited mode locked laser is typically on the order of many kilometers. Therefore, if the optical path length difference is much smaller than the coherent length, instead of interfering with its own copy in the reference arm, a pulse from the CPA arm can interfere with a different pulse from reference arm, without losing signal to noise contrast. Consequently, the length of the fiber spool was reduced to ~10m. The reduction in length of the fiber spool helps reducing fiber fluctuation and change in dispersion due to thermal fluctuation as well as mechanical vibration.

The number of the interference fringes is proportional to the change in time delay (or optical path length ΔL) between two pulses. The larger the ΔL, the bigger the number of the interference fringes. Increasing the number of interference fringes help improving the resolution of the retrieved spectral phase. The maximum resolution of the OSA in the experiment is 0.05 nm. By using an OSA with higher resolution, the interference fringes can be better resolved, resulting in more accurate phase retrieval.

A phase retrieval using a stationary-phase point scheme can be implemented[4]. The stationary-phase point scheme would help reducing false maxima and minima, hence further enhance the feature of the interference fringes. Also, in the phase retrieval Matlab code, instead of using a hard filtering window with cut-off values, a Hamming window $\omega(n) = \alpha - \beta \cos\left(\frac{2\pi n}{N-1}\right)$ with $\alpha + \beta$=1 and N is the number of data point, could be applied to filtering out the negative and zero-frequency components after Fourier transforming the spectrum.

[4] "Phase retrieval from spectral interferograms including a stationary-phase point", Petr Hlubina, Jacek Olszewski, Opt. Comm, Vol. 285, Iss 24, pp. 4733-386 (2012)

FUTURE WORK

This section describes the suggested paths that the student's work may lead in the near and long-term future.

- One approach that will be pursued is the incorporation of a spectral phase characterization using spectral interferometry approach. This would greatly reduce the required acquisition time to generate spectrometer with the nonlinear FROG method, without compromising the quality of data. The use of Mach-Zehnder spectral interferometry setup would be much simpler, cost effective, easy to design and implement, as it consists of using only fiber.
- Another future direction for the parabolic pulse shaping is in high power regime. The current focus is on parabolic pulse shaping for fiberized CPA laser system at average power output of about 50 mW. At higher output power setting, the effect of nonlinearity becomes more apparent, and therefore additional care is required to limit the degradation effects of self-phase modulation and higher order dispersion.

APPENDIX A:

CHIRPED FIBER BRAGG GRATING SPECIFICATION

In this appendix, the characteristics of CFBGs is presented, and the necessity for high quality CFBGs for pulse shaping as well as X-CPA and lidar ranging applications are discussed. The dispersion required, or the differential temporal delay between the wavelength components, required for pulses stretching to the 15 ns period regime, is extremely large. The optical bandwidth of the laser in question is about 10 nm at FWHM. Consequently, the required dispersion is in the order of 1.5 ns/ nm, which corresponds to a differential path length of 30 cm/nm in fiber.

A typical dispersion media in communication is the single mode fiber (SMF), which has ~17 ps/nm/km dispersion. With SMF, to achieve the same stretching regime, one would need tens of km of fiber to reach 15 ns in pulse duration. To date, most CPA as well as X-CPA applications require availability for complimentary dispersion to that used for the stretching. Dispersion compensating fiber (DCF), which has approximatelly over 10 times the dispersion of SMF can be utilized. However, as the group delay spectral profile of DCF does not match SMF for all wavelength components, matching complimentary stretching and compressing for pulse compression is very challenging. Consequently, CFBG technology arise as the cutting edge in providing large dispersions and making essential components for extremely chirped pulse generation and appplications. One important advantage of using CFBGs over fiber spool is the inherent small footprint, and less vulnerability to the thermal fluctuation of surrounding environment.

However, CFBG development faces its own challenges and the performance of many frequency-to-time mapping applications are limited by the current CFBG technology. It should

be noted that 1 ns/nm which can translate to a 10 ns differentail group delay for 10 nm of spectral separation, corresponds to 0.2 m of spatial separation in fiber. The most common technique to attain broadband reflection combining narrowband gratings individually recorded using interferometric techniques. Apparently, the detrimental results of this effect are shown in Figure A.0-1, where typical characteristic of a commercially available CFBG is shown. Both the insertion loss (reflectance) and the group delay demostrate periodic modulation is the result of the stitching process performed on many gratings.

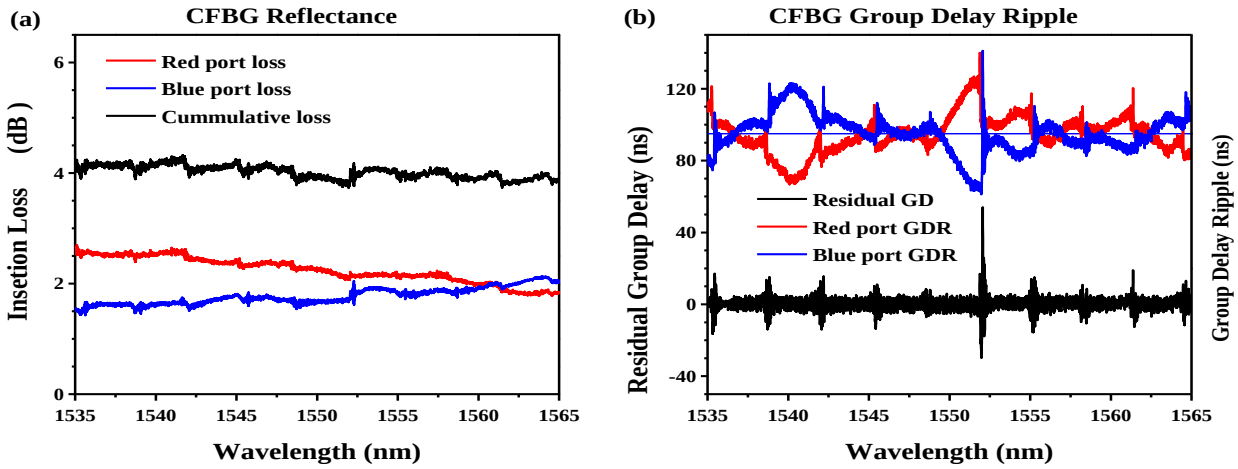

Figure A.0-1: Commercially available CFBG characterization. (a) Insertion loss. (b) Group delay ripple and round trip residual group delay. The GDR plots are also centered on zero and have been shifted for viewing purposes. Grating dispersion 991 ps/nm. The GDR has the order of magnitude of approximately 80 ps. This is the limiting factor of pulse compession in CHAPTER 1:

As seen in Figure A.0-1 (b), the group delay ripple of a CFBG is defined as the higher order group delay modulation. Ideally, the dispersion should show linear behavior, or zero-group delay ripple. In practice, the dispersion is only near linear, and the imperfections on the CFBG manufacturing result in residual group delay, which is the group delay sum of the two complimentary grating ports.

In the future, the advance in technique to manufacture CFBG can significantly reduce the amount of group delay ripples, and consequently, improve on the performance of pulse shaping, X-CPA oscillators, lidar ranging and many other applications.

APPENDIX B:

ARBITRARY WAVEFORM GENERATOR

Table 2. Arbitrary Waveform Generator Specification

Sampling Frequency	10 GSamples/sec
Resolution	8 digits
Accuracy	$\pm$1 ppm
Rise/Fall Time	50 ps
Amplitude	50 mV_{p-p} to 2.0 V_{p-p}
Amplitude Resolution	1 mV
Bandwidth	10 GHz
Output Impedance	50 Ω
Harmonic Distortion	$\leq$ -35 dBc
Insertion Loss	~ 6 dB
Timing Jitter	50 ps at 0.5 Gb/s
Trigger Rate	1.0 μs to 10.0 s
Trigger Resolution	3 digits, 0.1 μs minimum
Connector	SMA
Display	LCD color display with touchscreen
Operating System	Windows XP, USB communication port

In the RF world, a variety of modern technologies ranging from a wireless computer keyboard to a satellite image require signal generator equipments that can provide fast sample rate with high resolution to recreate complex RF behavior. The latest digital RF technologies often exceed the capabilities of current test equipment to generate wide-bandwidth and fast-changing signals that are increasingly seen in many wireless applications such as radar, UWB, and many others.

The Arbitrary Waveform Generator (AWG) used in the experiment is among the latest signal generator devices that enable the direct generation of RF signals and their output through the D /A converter for signals up to a carrier frequency of 5 GHz and a bandwidth of 10 GHz. The direct generation of IF or RF signals avoids I/Q degradations and lengthy adjustments associated with traditional generation using I/Q modulators. The AWG7000 Series with its maximum sample rate of 20 GS/s is an excellent solution that allows a direct RF signal generation for up to 5 GHz. In the experiment, the AWG is used to generate the required electrical (RF) signal to drive the $LiNbO_3$ Intensity modulator. The complexity of the electrical signal depends on the intensity profile of the input optical signal to the Intensity modulator, and the shape of the required output signal. In order to produce that complex signal, the AWG needs to have sufficient RF bandwidth; ideally the broader the inherent bandwidth, the better the generated RF signal matches the required signal. However, the cost of the AWG devices would go up exponentially with the available bandwidth. Therefore it's essentially to balance the needed quality of the output signal and the available bandwidth of AWG device to achieve a cost effective solution.

APPENDIX C:

ACOUSTO-OPTIC INTENSITY MODULATOR SPECIFICATION

Table 3. Acousto-Optic Intensity Modulator Specification

Wavelength	1550 nm
Optical Power Density	20 W/mm^2
Carrier Frequency	200 MHz
Rise Time	20 ns
Modulation Bandwidth	25 MHz
Max RF Power	1.5 W (~ 31 dBm)
Fiber Pigtail	PM single mode fiber
Back Reflection	40 dB
Insertion Loss	~ 6 dB

An acousto-optic modulator (AOM) is used to frequency select the repetion rate of the seed laser from 20 MHz to 1.25 MHz. The AOM is driven by an AOM driver with carrier frequency of 200 MHz. The AOM is a fiberized modulator, with output coupled into fiber, would significantly simplify alignment as well as reduce overall footprint of the laser system. It's advantagous to use the AOM instead of an Intensity modulator (IM), to improve the signal to noise ratio, and therefore achieve a higher quality results. An Intensity modulator would have less than 30 dB signal to noise ration, in contrast to at least 40 dB signal to noise ration of an AOM.

APPENDIX D:

FINISAR DESIGN AND SPECIFICATION

Table 4. Finisar Waveshaper Specification

Waveshaper	**Finisar**
Wavelength	1530 – 1562 nm
Frequency Range	191 – 196.05 THz
Insertion Loss	4 dB
Return Loss	> 30 dB
Filter Bandwidth	0.1 – 32 nm
Frequency Accuracy	+/- 5 GHz
Attenuation Range	0 – 35 dB
Attenuation Resolution	Better than 0.1 dB
Max Input Power	13 dBm
Dispersion x Bandwidth product	40s

Finisar programmable optical processor

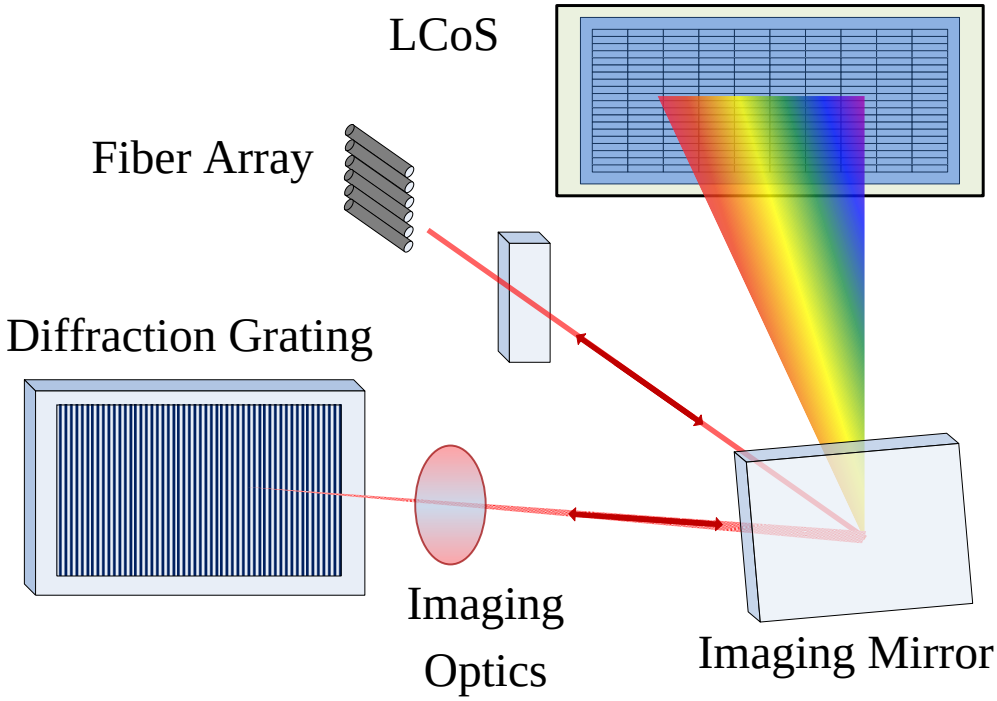

Figure D.0-1: The programmable optical processor Finisar is connected and controlled by a computer via USB gate. The Finisar used in the experiment is the Programmable Optical Filtering (Waveshaper 1000E) version, with one input and one output optical port. The waveshaper has a low insertion loss, typically around 4.5 dB, flat spectral response across the C-band. Additionally, the 4000E version (not used in the experiment) has low cross talk between ports.

The Finisar spectral processor is a programmable, flexible wavelength selective switch (WSS) device based on liquid crystal on Silicon (LCoS) technology, which can be programmed, reconfigured, updated to arbitrary modulate spectral intensity and phase of specified channels. The LCoS acts as a programmable and reconfigurable 2-D optical phased array reflector.

Light enters the Finisar optical wave processor fiber array, and is then sent through polarization diversity optics to align orthogonal polarization states to maximize efficiency at the diffraction grating. Beam incidents the diffraction grating at first-order Littrow angle, which is the angle in which the grating diffracts light back along the incident beam. The diffraction grating angularly disperses the incoming light, so that each color is sent to different pixel of the LCoS array across the horizontal axis. The light diverges vertically so that the signal overlaps a large numbers of pixels. The reflected light is traced back through the system to the output port. As the wavelengths are separated on the LCoS after dispersion from the grating, each color (or wavelength) is controlled independently and without interfering, or cross-talking with other colors. [85]

The phase of the signal is modulated by controlling the voltage dependent retardation of each pixel. The attenuation control for each pixel is achieved by setting the phase pattern on the LCoS array such that the light is split into two components. One component is sent to the output port, while the other component is directed to a power dump within the Finisar wave processor. By changing the relative power in each of these two beams, the attenuation is precisely controlled, with better than 0.1 dB attenuation resolution.

Moreover, the phase of the signal on the LCoS can also be varied along the horizontal (or spectral) axis. A linear change in spectral phase corresponds to a temporal shift in the time domain. For example parabolically varying spectral phase will correspond to a linearly varying group delay, which translates to a change in group dispersion or temporal delay. Therefore dispersion and temporal delay generation and compensation is also possible. [85]

APPENDIX E:

MATLAB ALGORITHMS AND LABVIEW INTERFACES

Appendix E 1. Matlab algorithms

In CHAPTER 5: the spectral phase retrieval was performed by analyzing the optical spectral interferogram. The Matlab algorithm to generate FROG spectrogram is shown in the following section. The spectral phase retrieval code is also presented in the following paragraph. An input data file is required to run the algorithm, which contains two columns, one for wavelength, and one for interference spectrogram in linear scale.

```
%FROG spectrogram generation using a parabolic input pulse
%This program will calculate the Wigner OR Ambiguity Distribution;
%Note the time reversal of the waveform a2 for calculating the Wigner.
clear; close all;
N=64; Ntot= 4*776;
i=1:N;
j=1:N;
k=1:3*N;
a2(k)=0;
a1(k)=0;

%Parabolic Pulse
%T=30;
%a1(N+1:2*N)=1.0*sech((i-N/2)./T);
%a2(N+1:2*N)=1.0*sech((i-N/2)./T);
a1(N+1:2*N)= (1.0*(-(i-N/2).^2)+ Ntot)./Ntot;
a2(N+1:2*N)= (1.0*(-(i-N/2).^2)+ Ntot)./Ntot;
%plot(i,e(i));

%Gaussian Pulses w/ quadratic / or cubic phase (change exponent)
%a1(N+1:2*N)=(1.0*exp(sqrt(-1)*(2*pi*32.0*i/N+0.002*(i-N/2).^3))).*(1.0*exp(-(i-
N/2).^2/10.^2));
%a2(N+1:2*N)=(1.0*exp(sqrt(-1)*(2*pi*32.0*i/N+0.002*(i-N/2).^3))).*(1.0*exp(-(i-
N/2).^2/10.^2));
%a2(2*N:-1:N+1)=(1.0*exp(sqrt(-1)*(2*pi*32.0*i/N+0.002*(i-N/2).^3))).*(1.0*exp(-(i-
N/2).^2/10.^2));

%Gaussian Pulses w/ intensity dependant SPM
%a1(N+1:2*N)=(1.0*exp(sqrt(-1)*(2*pi*16.0*i/N+ (1.0*exp(-(i-
N/2).^2/10.^2)))).^2).*(1.0*exp(-(i-N/2).^2/10.^2));
%a2(N+1:2*N)=(1.0*exp(sqrt(-1)*(2*pi*16.0*i/N+ (1.0*exp(-(i-
N/2).^2/10.^2)))).^2).*(1.0*exp(-(i-N/2).^2/10.^2));
%a2(2*N:-1:N+1)=(1.0*exp(sqrt(-1)*(2*pi*16.0*i/N+ (1.0*exp(-(i-
N/2).^2/10.^2)))).^2).*(1.0*exp(-(i-N/2).^2/10.^2));

for j=1:N,
   for i=1:N,
%      a3(i,j)=a1(3*N/2+i-j).*(conj(a2(N/2+i+j))).*(-1).^(j+i);
%Use this for rect pulses
     a3(i,j)=a1(N+j+i).*(conj(a2(N+i-j))).*(-1)^(j+i);
     a4=a3.';
 %     a4(j,i)=a3(i,j);
   end
end
```

```
 i=1:N;
 figure;
 plot(i,real(a1(N+i)),i,real(a2(N+i)));

sound(real(a1));
A3=((fft(a4)));
A3M=sum(A3.');

 %A4=((fft2(A3)));
 %plot (i,A3M(i));
%mesh(A3);
%contour(A3);
figure;
 %surfl(25-abs(A3));
pcolor(-abs(A3'));
% surfl(a4);
  shading interp;
  %colormap(hot);
  colormap(jet)
%waterfall((A3));
%contour((A3));
%colormap(hsv);
%view(0,90);
rotate3d on;
```

```
%Fast Fourier transform algorithms to retrieve optical spectral phase using spectral
%interferometry approach

clear all
clc;
c = 3*10^8;
%-------------------------------------------------------------------------------
%Input interference spectrum
load OSAinput.txt
wavelength= OSAinput(:,1)
interference= OSAinput(:,2)
figure(1)
plot(wavelength,interference);
Ftransform= fft(interference);
pft= abs(Ftransform);

subplot(2,2,1); plot(abs(Ftransform));
%manually create the window, set All but the window to zero
iR=200
iL=35
for ii = iR:1001
   Ftransform(ii) = 0;
end
for ii = 1:iL
   Ftransform(ii) = 0;
end
subplot(2,2,2); plot(abs(Ftransform));
%-------------------------------------------------------------------------------
%shift peak to zero
SFtransform = zeros(1001,1);
[Max Pos] = max(Ftransform);
for ii = 1:iR-iL
   SFtransform(ii+499-Pos+iL) = Ftransform(ii+iL-1);
end
%-------------------------------------------------------------------------------
%Retrieve spectral phase by  inverse Fourier transforming Ftransform
subplot(2,2,3); plot(abs(SFtransform));
Sphase = (unwrap(angle(ifft(fftshift(SFtransform)))));
Sphase= Sphase/2/pi;
subplot(2,2,4); plot(wavelength,Sphase)
```

```
%Finisar mask generation


clc; clear all; %close all; clf;
% loading optical spectrum in dB scale
load OSAinput.txt
lambdas = OSAinput(:,1);
Spectrum= OSAinput(:,2);

c= 299792458; % speed of light
min_intensity= -69; % in dB
pmin= 10^(min_intensity/10); %extend parabola tails low dB.
lspect= 10.^(Spectrum/10);   %change intensity to linear

%parabola parameters can be changed to match specific input spectrum
a= 0.0155; x0= 1552.65; b= 0.0135;
x1= x0-sqrt(b)/a;
x2= x0+sqrt(b)/a;
parabola= (-(a*(lambdas-x0)).^2+b);
parabola= 0.027*(-(a*(lambdas-x0)).^2+b).*(lambdas>x1).*(lambdas<x2);
parabola= parabola-(lambdas<x1)*pmin-(lambdas>x2)*pmin;
paradB= 10*log10(parabola); %%change intensity to dB
paradB= real(paradB);

%IMPORTANT
%OSA needs to be calibrated to match central frequency of Finisar
freq=c./lambdas/1000; % frequency in THz
%freq0= c/1552/1000;
freq0= 193.117        % specify central frequency
freq_detune=(freq-freq0);

figure(1); clf,
subplot(2,2,1);
plot(lambdas,lspect,lambdas,parabola,'k','linewidth',1.5);
xlim([1542.5,1562.5]); ylim([-(1e-6),1.5e-3]); grid on
set(gca,'fontweight','demi');
xlabel('Wavelength (nm)'); ylabel('Power (au)')
title('Linear spectrum')
```

```
subplot(2,2,2);
plot(lambdas,Spectrum,lambdas,paradB,'k','linewidth',2); grid on
xlim([1542.5,1562.5]); ylim([-70,-25]);
grid on
set(gca,'fontweight','demi');
xlabel('Wavelength (nm)'); ylabel('Power (dB)')
title('Spectrum in dB');


% mask in linear scale
subplot(2,2,3);
lmask=lspect-parabola;
lmask= lmask;
plot(lambdas,lmask,'k','linewidth',1.5);
xlim([1542.5,1562.5]); ylim([-(1e-6),1.5e-3]); grid on
set(gca,'fontweight','demi');
xlabel('Wavelength (nm)'); ylabel('Power (au)')
title('Required attenuation');

% mask in dB scale
subplot(2,2,4);
mask= (Spectrum-paradB).*(lambdas>x1).*(lambdas<x2);
```

Appendix E 2. Finisar Interface

Finisar programmable optical processor

Figure E.0-1: The programmable optical processor Finisar is connected and controlled by a computer via USB gate. The Finisar used in the experiment is the Programmable Optical Filtering (Waveshaper 1000E) version, with one input and one output optical port. The waveshaper has a low insertion loss, typically around 4.5 dB, flat spectral response across the C-band. Additionally, the 4000E version (not used in the experiment) has low cross talk between ports.

Finisar software

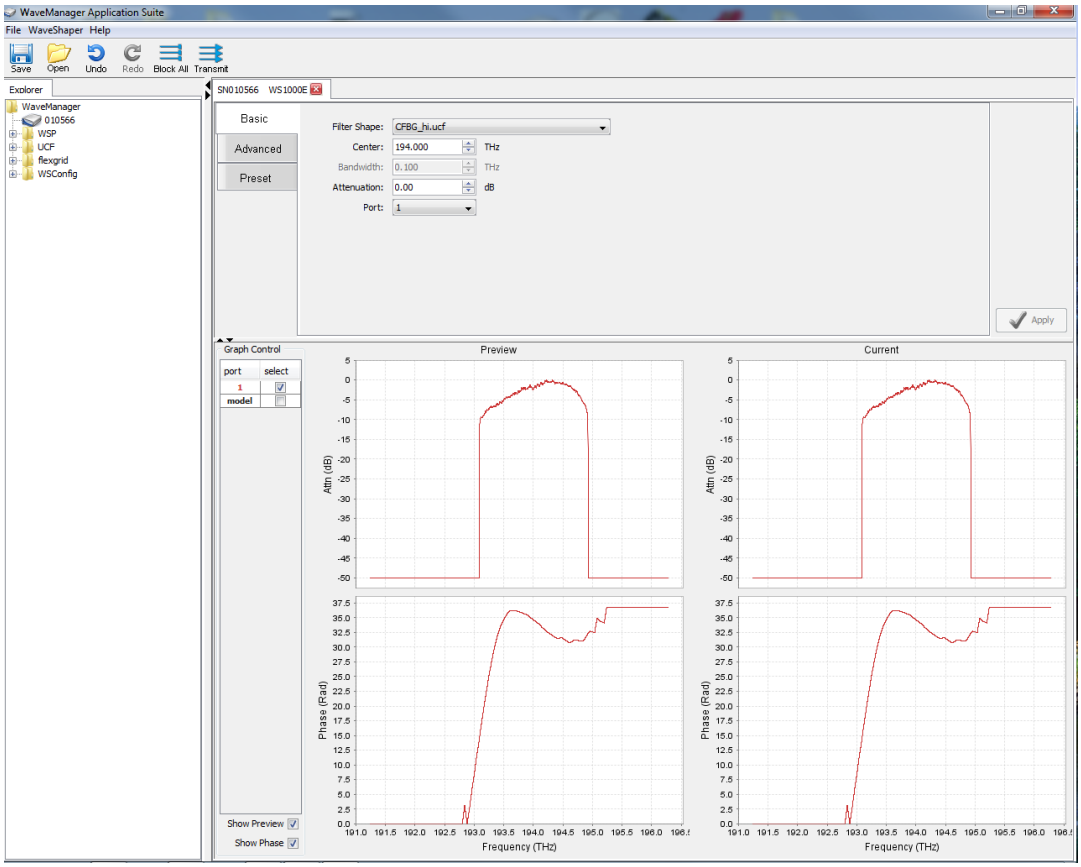

Figure E.0-2: Commercially available Finisar software to control the optical Finisar spectral wave processor. The interface is controlled with a desktop computer, and communicates with the Finisar spectral processor via USB gate. An intensity mask and a spectral phase mask are designed and applied to the input optical pulses, as can be seen in the picture. An input center wavelength frequency is calculated to properly align spectral masks to optical spectrum of the pulses.

APPENDIX F:

PUBLICATIONS AND PRESENTATIONS

1. M. U. Piracha, D. Nguyen, and P. J. Delfyett, "Spectral Pulse Shaping and Group Delay Ripple Compensation with 10 dB SNR Improvement and 284 μm Range Resolution in a Chirped Pulse Lidar," Photonics Technology Letters, IEEE (n.d.).

2. D. Nguyen, M. U. Piracha, M. Bagnell, and P. J. Delfyett, "Near Transform Limited Sub-picosecond High Power Pulse Generation via Interferometric Spectral Phase Compensation," CLEO: Science and Innovation (2013). (submitted)

3. P. J. Delfyett, D. Mandridis, M. U. Piracha, D. Nguyen, K. Kim, and S. Lee, "Chirped Pulse Laser Sources and Applications," Progress in Quantum Electronics (2012).

4. D. Nguyen, M. U. Piracha, and P. J. Delfyett, "Spectral Pulse Shaping with Adaptive Feedback in Fiberized CPA Systems for Sub-Picosecond , High Contrast Pulses," Photonics Conference (IPC) IEEE Proceeding **5**, 840–841 (2012).

5. M. U. Piracha, D. Nguyen, and P. J. Delfyett, "Compensation of Group Delay Ripple in Chirped Fiber Bragg Gratings and its Application in Chirped Pulse Laser Radar," Photonics Conference (IPC) IEEE Proceeding **3**, 646–647 (2012).

6. S. Shabahang, M. P. Marquez, G. Tao, M. U. Piracha, and D. Nguyen, "Octave-spanning infrared supercontinuum generation in robust chalcogenide nanotapers using picosecond pulses," Optics Letters **37**, 4639–4641 (2012).

7. M. U. Piracha, D. Nguyen, and P. J. Delfyett, "High resolution chirped pulse lidar with spectral phase moduationfor two fold improvement in range resolution," Avionics, Fiber-Optics and Photonics Technology Conference Proceeding (2012).

8. M. U. Piracha, D. Nguyen, and P. J. Delfyett, "A Chirped Fiber Bragg Grating with Ripple Free Group Delay and its Application in Laser Ranging," CLEO: Science and Innovation **1**, 1–2 (2012).

9. D. Nguyen, M. U. Piracha, K. Kim, M. Hamamoto, M. Mielke, and P. J. Delfyett, "An Active Feedback Pulse Shaping Technique with Spectral Phase and Intensity Modulation to Generate Transform Limited , Parabolic Pulses for CPA Systems," CLEO: Science and Innovations (2012).

10. D. Nguyen, M. U. Piracha, and P. J. Delfyett, "Sub-picosecond, transform limited pulse generation in fiber CPA systems utilizing spectral pulse shaping with adaptive feedback loop," IEEE Avionic conference proceeding 1–2 (2012).

11. D. Nguyen, M. U. Piracha, and P. J. Delfyett, "Transform-limited pulses for chirped-pulse amplification systems utilizing an active feedback pulse shaping technique enabling five time increase in peak power," Optics Letters **37**, 4913 (2012).

12. M. U. Piracha, D. Nguyen, and I. Ozdur, "Chirped pulse lidar using a mode locked laser source for metrology," (PHO), 2011 IEEE **4**, 700–701 (2011).

13. D. Nguyen, M. U. Piracha, D. Mandridis, and P. J. Delfyett, "Temporal shaping of ultrafast chirped pulses with 27dB extinction ration using an arbitrary waveform generator," Proceedings of SPIE (2011).

14. M. U. Piracha, D. Nguyen, I. Ozdur, and P. J. Delfyett, "A High Resolution, Chirped Pulse Lidar for Simultaneous Range and Velocity Measurements," in *CLEO: Science and Innovations* (Optical Society of America, 2011), pp. 1–2.

15. D. Nguyen, M. U. Piracha, P. J. Delfyett, and D. Mandridis, "Temporal Shaping of Parabolic Chirped Pulses with 27 dB Extinction Ratio for Fiber Chirped Pulse Amplification Systems," in *CLEO: Applications and Technology* (Optical Society of America, 2011), pp. 2–3.

16. D. Nguyen, M. U. Piracha, D. Mandridis, and P. J. Delfyett, "Dynamic parabolic pulse generation using temporal shaping of wavelength to time mapped pulses," Optics express **19**, 12305–11 (2011).

17. M. U. Piracha, D. Nguyen, I. Ozdur, and P. J. Delfyett, "Simultaneous ranging and velocimetry of fast moving targets using oppositely chirped pulses from a mode-locked laser.," Optics express **19**, 11213–9 (2011).

18. D. Nguyen, M. U. Piracha, D. Mandridis, P. J. Delfyett, Jr., M. Greenberg, M. Mielke, and T. Booth, "Time domain parabolic pulse creation of ultrafast chirped pulses," Proceedings of SPIE **7700**, 77000J–77000J–8 (2010).

19. M. U. Piracha, D. Nguyen, D. Mandridis, T. Yilmaz, I. Ozdur, S. Ozharar, and P. J. Delfyett, "Range resolved lidar for long distance ranging with sub-millimeter resolution.," Optics express **18**, 7184–9 (2010).

20. M. U. Piracha, D. Nguyen, D. Mandridis, T. Yilmaz, D. Gaudiosi, and P. J. Delfyett, "Sub-millimeter resolution laser ranging at 9.3 kilometers using temporally stretched frequency chirped pulses from a mode-locked laser," Proceedings of SPIE **7339**, 73390I–73390I–11 (2009).

21. L. Jia, D. Nguyen, J. W. Halleý, P. Pham, W. Lamanna, and S. Hamrock, "Proton Transport in HTFSI–TFSI–EMI Mixtures: Experiment and Theory," Journal of The Electrochemical Society **156**, B136 (2009).

22. M. U. Piracha, D. Nguyen, and D. Mandridis, "Range resolved, high resolution lidar using frequency chirped pulses," LEOS'09. 260–261 (2009).

23. M. U. Piracha, D. Nguyen, D. Mandridis, I. Ozdur, T. Yilmaz, S. Ozharar, and P. J. Delfyett, "Range Resolved, Sub-Millimeter Resolution Lidar Using Temporally Stretched, Frequency Chirped Pulses," in *Frontiers in Optics* (Optical Society of America, 2009), pp. 3–4.

24. M. U. Piracha, D. Nguyen, D. Mandridis, T. Yilmaz, D. Gaudiosi, and P. J. Delfyett, "Sub-millimeter resolution laser ranging at 9.3 kilometers using temporally stretched frequency chirped pulses from a mode-locked laser," Proceedings of CLEO 73390I–73390I–11 (2009).

25. V. Nguyen and T. Nguyen, "Coulomb blockade threshold in finite one-dimensional arrays of small tunnel junctions: computer simulation," Physics Letters A **291**, 150–158 (2001).

26. V. L. Nguyen, M. T. Nguyen, and T. D. Nguyen, "Magnetic field effects on the binding energy of hydrogen impurities in quantum dots with parabolic confinements," Physica B **292**, 159 (2000).

APPENDIX G:

INVENTION DISCLOSURES

[1] “A chirped fiber Bragg grating with ripple-free group delay”, P.J. Delfyett, M. U. Piracha, and **D. Nguyen** (pending).

[2] “Dynamic feedback mechanism with spectral pulse shaping to generate and amplify femtosecond pulses for chirped pulse amplification systems”, P. J. Delfyett, **D. Nguyen**, M. U. Piracha (pending).

LIST OF REFERENCES

1. M. Pessot, J. Squier, G. Mourou, and D. J. Harter, "Chirped-pulse amplification of 100-fsec pulses," Optics Letters **14**, 797 (1989).

2. P. Maine, D. Strickland, P. Bado, M. Pessot, and G. Mourou, "Generation of ultrahigh peak power pulses by chirped pulse amplification," IEEE Journal of Quantum Electronics **24**, 398–403 (1988).

3. P. Maine and G. Mourou, "Amplification of 1-nsec pulses in Nd:glass followed by compression to 1 psec," Optics Letters **13**, 467 (1988).

4. R. A. Fisher, "Pulse compression for more efficient operation of solid-state laser amplifier chains," Applied Physics Letters **24**, 468 (1974).

5. J. Limpert and F. Roser, "High-power ultrafast fiber laser systems," Selected Topics in Quantum Electronics **12**, 233–244 (2006).

6. D. Strickland and G. Mourou, "Compression of amplified chirped optical pulses," Optics Communications **56**, 219–221 (1985).

7. J. L. Tapié and G. Mourou, "Shaping of clean, femtosecond pulses at 1.053 microm for chirped-pulse amplification.," Optics letters **17**, 136–8 (1992).

8. D. Normand, M. Ferray, L. A. Lompré, O. Gobert, A. L'Huillier, and G. Mainfray, "Focused laser intensity measurement at 10^18 W/cm^2 and 1053 nm," Optics Letters **15**, 1400 (1990).

9. F. Röser, T. Eidam, J. Rothhardt, O. Schmidt, D. N. Schimpf, J. Limpert, and a Tünnermann, "Millijoule pulse energy high repetition rate femtosecond fiber chirped-pulse amplification system.," Optics letters **32**, 3495–7 (2007).

10. J. van Howe, G. Zhu, and C. Xu, "Compensation of self-phase modulation in fiber-based chirped-pulse amplification systems.," Optics letters **31**, 1756–8 (2006).

11. J. Limpert, T. Clausnitzer, a Liem, T. Schreiber, H. J. Fuchs, H. Zellmer, E. B. Kley, and a Tünnermann, "High-average-power femtosecond fiber chirped-pulse amplification system.," Optics letters **28**, 1984–6 (2003).

12. R. G. Smith, "Optical Power Handling Capacity of Low Loss Optical Fibers as Determined by Stimulated Raman and Brillouin Scattering," Applied Optics **11**, 2489 (1972).

13. A. Kobyakov, M. Sauer, and D. Chowdhury, "Stimulated Brillouin scattering in optical fibers," Advances in Optics and Photonics **2**, 1 (2009).

14. G. P. Agrawa, *Nonlinear Fiber Optics*, 4th ed. (Elsevier Science and Technology Books, 2006).

15. A. J. Hymans and J. Lait, "Analysis of a frequency-modulated continuous-wave ranging system," Proceedings of the IEE Part B: Electronic and Communication Engineering **107**, 365 (1960).

16. G. Beheim and K. Fritsch, "Remote displacement measurements using a laser diode," Electronics Letters **21**, 93 (1985).

17. R. E. Saperstein, N. Alic, S. Zamek, K. Ikeda, B. Slutsky, and Y. Fainman, "Processing advantages of linear chirped fiber Bragg gratings in the time domain realization of optical frequency-domain reflectometry.," Optics express **15**, 15464–79 (2007).

18. M. U. Piracha, D. Nguyen, I. Ozdur, and P. J. Delfyett, "Simultaneous ranging and velocimetry of fast moving targets using oppositely chirped pulses from a mode-locked laser.," Optics express **19**, 11213–9 (2011).

19. M. U. Piracha, D. Nguyen, D. Mandridis, T. Yilmaz, I. Ozdur, S. Ozharar, and P. J. Delfyett, "Range resolved lidar for long distance ranging with sub-millimeter resolution.," Optics express **18**, 7184–9 (2010).

20. C. Cook, "Pulse Compression-Key to More Efficient Radar Transmission," Proceedings of the IRE **48**, 310–316 (1960).

21. A. Galvanauskas, M. Fermann, and D. Harter, "High-power amplification of femtosecond optical pulses in a diode-pumped fiber system," Optics letters **19**, 1201–1203 (1994).

22. T. Ganz, V. Pervak, a Apolonski, and P. Baum, "16 fs, 350 nJ pulses at 5 MHz repetition rate delivered by chirped pulse compression in fibers.," Optics letters **36**, 1107–9 (2011).

23. K. Kim, S. Lee, and P. Delfyett, "1.4kW high peak power generation from an all semiconductor mode-locked master oscillator power amplifier system based on eXtreme Chirped Pulse Amplification(X-CPA).," Optics express **13**, 4600–6 (2005).

24. K. Kim, S. Lee, and P. Delfyett, "eXtreme chirped pulse amplification-beyond the fundamental energy storage limit of semiconductor optical amplifiers," IEEE Journal of Selected Topics in Quantum Electronics **12**, 245–254 (2006).

25. T. Hirooka and M. Nakazawa, "Parabolic pulse generation by use of a dispersion-decreasing fiber with normal group-velocity dispersion.," Optics letters **29**, 498–500 (2004).

26. B. Kibler, C. Billet, P. Lacourt, and R. Ferriere, "Parabolic pulse generation in comb-like profiled dispersion decreasing fibre," Electronics **42**, (2006).

27. C. Finot, G. Millot, C. Billet, and J. Dudley, "Experimental generation of parabolic pulses via Raman amplification in optical fiber.," Optics express **11**, 1547–52 (2003).

28. C. Finot, B. Barviau, G. Millot, A. Guryanov, A. Sysoliatin, and S. Wabnitz, "Parabolic pulse generation with active or passive dispersion decreasing optical fibers.," Optics express **15**, 15824–35 (2007).

29. M. E. Fermann, V. I. Kruglov, B. C. Thomsen, J. M. Dudley, and J. D. Harvey, "Self-similar propagation and amplification of parabolic pulses in optical fibers.," Physical review letters **84**, 6010–3 (2000).

30. a. Y. Plotski, a. a. Sysoliatin, a. I. Latkin, V. F. Khopin, P. Harper, J. Harrison, and S. K. Turitsyn, "Experiments on the generation of parabolic pulses in fibers with length-varying normal chromatic dispersion," JETP Letters **85**, 319–322 (2007).

31. F. W. Wise, a. Chong, and W. H. Renninger, "High-energy femtosecond fiber lasers based on pulse propagation at normal dispersion," Laser & Photonics Review **2**, 58–73 (2008).

32. S. Boscolo, S. K. Turitsyn, V. Y. Novokshenov, and J. Nijhof, "Self-similar parabolic optical solitary waves," Theoretical and mathematical physics **133**, 1647–1656 (2002).

33. A. I. Latkin, S. K. Turitsyn, and A. a Sysoliatin, "Theory of parabolic pulse generation in tapered fiber.," Optics letters **32**, 331–3 (2007).

34. J. Ye, L. Yan, W. Pan, B. Luo, X. Zou, A. Yi, and S. Yao, "Photonic generation of triangular-shaped pulses based on frequency-to-time conversion.," Optics letters **36**, 1458–60 (2011).

35. D. Nguyen, M. U. Piracha, D. Mandridis, and P. J. Delfyett, "Dynamic parabolic pulse generation using temporal shaping of wavelength to time mapped pulses.," Optics express **19**, 12305–11 (2011).

36. S. Boscolo and C. Finot, "Nonlinear Pulse Shaping in Fibres for Pulse Generation and Optical Processing," International Journal of Optics **2012**, 1–14 (2012).

37. A. Weiner, "Femtosecond pulse shaping using spatial light modulators," Review of scientific instruments **71**, 1929 (2000).

38. D. Mandridis, I. Ozdur, and P. J. Delfyett, "An Electrooptic Feedforward System for Dynamic Control of a Quasi-Continuous-Wave Chirped Laser Source," IEEE Photonics Technology Letters **21**, 1226–1228 (2009).

39. D. Anderson, M. Desaix, M. Karlsson, M. Lisak, and M. L. Quiroga-Teixeiro, "Wave-breaking-free pulses in nonlinear-optical fibers," Journal of the Optical Society of America B **10**, 1185 (1993).

40. V. I. Kruglov, a C. Peacock, J. M. Dudley, and J. D. Harvey, "Self-similar propagation of high-power parabolic pulses in optical fiber amplifiers.," Optics letters **25**, 1753–5 (2000).

41. V. Kruglov, A. Peacock, J. Harvey, and J. Dudley, "Self-similar propagation of parabolic pulses in normal-dispersion fiber amplifiers," JOSA B **19**, 461–469 (2002).

42. V. I. Kruglov, D. Méchin, and J. D. Harvey, "All-fiber ring Raman laser generating parabolic pulses," Physical Review A **81**, 1–11 (2010).

43. C. Finot, J. M. Dudley, B. Kibler, D. J. Richardson, and G. Millot, "Optical Parabolic Pulse Generation and Applications," IEEE Journal of Quantum Electronics **45**, 1482–1489 (2009).

44. F. Parmigiani, C. Finot, K. Mukasa, M. Ibsen, M. a Roelens, P. Petropoulos, and D. J. Richardson, "Ultra-flat SPM-broadened spectra in a highly nonlinear fiber using parabolic pulses formed in a fiber Bragg grating.," Optics express **14**, 7617–22 (2006).

45. A. Peacock and N. Healy, "Parabolic pulse generation in tapered silicon fibers.," Optics letters **35**, 1780–2 (2010).

46. D. N. Schimpf, J. Limpert, and A. Tünnermann, "Controlling the influence of SPM in fiber-based chirped-pulse amplification systems by using an actively shaped parabolic spectrum.," Optics express **15**, 16945–53 (2007).

47. L. Zhu and G. Li, "Folded digital backward propagation for dispersion-managed fiber-optic transmission.," Optics express **19**, 5953–9 (2011).

48. M. Pessot, P. Maine, and G. Mourou, "1000 times expansion/compression of optical pulses for chirped pulse amplification," Optics Communications **62**, 419–421 (1987).

49. F. H. Loesel, J. P. Fischer, M. H. Götz, C. Horvath, T. Juhasz, F. Noack, N. Suhm, and J. F. Bille, "Non-thermal ablation of neural tissue with femtosecond laser pulses," Applied Physics B: Lasers and Optics **66**, 121–128 (1998).

50. C. Sauteret, D. Husson, G. Thiell, S. Seznec, S. Gary, a Migus, and G. Mourou, "Generation of 20-TW pulses of picosecond duration using chirped-pulse amplification in a Nd:glass power chain.," Optics letters **16**, 238–40 (1991).

51. A. Dubietis, G. Jonušauskas, and A. Piskarskas, "Powerful femtosecond pulse generation by chirped and stretched pulse parametric amplification in BBO crystal," Optics Communications **88**, 437–440 (1992).

52. D. N. Schimpf, E. Seise, T. Eidam, J. Limpert, and a Tünnermann, "Control of the optical Kerr effect in chirped-pulse-amplification systems using model-based phase shaping.," Optics letters **34**, 3788–90 (2009).

53. B. H. Kolner, "Space-time duality and the theory of temporal imaging," IEEE Journal of Quantum Electronics **30**, 1951–1963 (1994).

54. S. Lee, D. Mandridis, and P. J. Delfyett, "eXtreme chirped pulse oscillator operating in the nanosecond stretched pulse regime.," Optics express **16**, 4766–73 (2008).

55. F. He, H. S. S. Hung, J. H. V Price, N. K. Daga, N. Naz, J. Prawiharjo, D. C. Hanna, D. P. Shepherd, D. J. Richardson, J. W. Dawson, C. W. Siders, and C. P. Barty, "High energy femtosecond fiber chirped pulse amplification system with adaptive phase control.," Optics express **16**, 5813–21 (2008).

56. D. N. Papadopoulos, I. Martial, M. Hanna, F. Druon, and P. Georges, "Active spectral phase control by use of an acousto-optic programmable filter in high-repetition-rate sub-80 fs nonlinear fiber amplifiers.," Optics letters **33**, 1431–3 (2008).

57. K. W. DeLong, D. N. Fittinghoff, and R. Trebino, "Practical issues in ultrashort-laser-pulse measurement using frequency-resolved optical gating," IEEE Journal of Quantum Electronics **32**, 1253–1264 (1996).

58. R. Trebino and D. J. Kane, "Using phase retrieval to measure the intensity and phase of ultrashort pulses: frequency-resolved optical gating," Journal of the Optical Society of America A **10**, 1101 (1993).

59. D. J. Kane and R. Trebino, "Characterization of arbitrary femtosecond pulses using frequency-resolved optical gating," IEEE Journal of Quantum Electronics **29**, 571–579 (1993).

60. K. O. Hill, Y. Fujii, D. C. Johnson, and B. S. Kawasaki, "Photosensitivity in optical fiber waveguides: Application to reflection filter fabrication," Applied Physics Letters **32**, 647 (1978).

61. G. Meltz, W. W. Morey, and W. H. Glenn, "Formation of Bragg gratings in optical fibers by a transverse holographic method," Optics Letters **14**, 823 (1989).

62. G. D. Marshall, R. J. Williams, N. Jovanovic, M. J. Steel, and M. J. Withford, "Point-by-point written fiber-Bragg gratings and their application in complex grating designs," Optics Express **18**, 19844 (2010).

63. F. Ouellette, "Dispersion cancellation using linearly chirped Bragg grating filters in optical waveguides," Optics Letters **12**, 847 (1987).

64. R. Kashyap, *Fiber Bragg Gratings* (Academic Press, 1999), pp. 1–458.

65. A. M. Weiner, *Ultrafast Optics* (John Wiley & Sons, Inc., 2009).

66. E. Treacy, "Optical pulse compression with diffraction gratings," IEEE Journal of Quantum Electronics **5**, 454–458 (1969).

67. O. Martinez, J. Gordon, and R. Fork, "Negative group-velocity dispersion using refraction," JOSA A **1**, 1003–1006 (1984).

68. M. Stern, J. Heritage, and E. Chase, "Grating compensation of third-order fiber dispersion," Quantum Electronics, IEEE … **2**, (1992).

69. S. Kane and J. Squier, "Grating compensation of third-order material dispersion in the normal dispersion regime: Sub-100-fs chirped-pulse amplification using a fiber stretcher and grating-pair compressor," IEEE Journal of Quantum Electronics **31**, 2052–2057 (1995).

70. R. Trebino, P. Bowlan, P. Gabolde, X. Gu, S. Akturk, and M. Kimmel, "Simple devices for measuring complex ultrashort pulses," Laser & Photonics Review **3**, 314–342 (2009).

71. K. W. DeLong, D. N. Fittinghoff, R. Trebino, B. Kohler, and K. Wilson, "Pulse retrieval in frequency-resolved optical gating based on the method of generalized projections," Optics Letters **19**, 2152 (1994).

72. K. W. DeLong and R. Trebino, "Improved ultrashort pulse-retrieval algorithm for frequency-resolved optical gating," Journal of the Optical Society of America A **11**, 2429 (1994).

73. B. Kohler, V. V Yakovlev, K. R. Wilson, J. Squier, K. W. Delong, and R. Trebino, "Phase and intensity characterization of femtosecond pulses from a chirped-pulse amplifier by frequency-resolved optical gating.," Optics letters **20**, 483–5 (1995).

74. L. Xu, E. Zeek, and R. Trebino, "Simulations of frequency-resolved optical gating for measuring very complex pulses," Journal of the Optical Society of America B **25**, A70 (2008).

75. D. N. Fittinghoff, K. W. DeLong, R. Trebino, and C. L. Ladera, "Noise sensitivity in frequency-resolved optical-gating measurements of ultrashort pulses," Journal of the Optical Society of America B **12**, 1955 (1995).

76. D. J. Kane and R. Trebino, "Single-shot measurement of the intensity and phase of an arbitrary ultrashort pulse by using frequency-resolved optical gating," Optics Letters **18**, 823 (1993).

77. J.-C. Diels, *Ultrashort Laser Puslse Phenomena*, 1 edition (Academic Press, n.d.).

78. D. Nguyen, M. U. Piracha, and P. J. Delfyett, "Transform-limited pulses for chirped-pulse amplification systems utilizing an active feedback pulse shaping technique enabling five time increase in peak power," Optics Letters **37**, 4913 (2012).

79. F. Technologies, "Femtoshoft Technologies FROG Fast Guide Tutorial," Femtosoft Technologies 1–39 (2004).

80. V. Wong and I. a Walmsley, "Analysis of ultrashort pulse-shape measurement using linear interferometers.," Optics letters **19**, 287 (1994).

81. C. Dorrer and I. Kang, "Highly sensitive direct characterization of femtosecond pulses by electro-optic spectral shearing interferometry.," Optics letters **28**, 477–9 (2003).

82. I. Kang, C. Dorrer, and F. Quochi, "Implementation of electro-optic spectral shearing interferometry for ultrashort pulse characterization.," Optics letters **28**, 2264–6 (2003).

83. J. W. Nicholson, F. G. Omenetto, D. J. Funk, and a J. Taylor, "Evolving FROGS: phase retrieval from frequency-resolved optical gating measurements by use of genetic algorithms.," Optics letters **24**, 490–2 (1999).

84. S. Diddams and J. Diels, "Dispersion measurements with white-light interferometry," America **13**, 1120–1129 (1996).

85. M. a. F. Roelens, S. Frisken, J. a. Bolger, D. Abakoumov, G. Baxter, S. Poole, and B. J. Eggleton, "Dispersion Trimming in a Reconfigurable Wavelength Selective Switch," Journal of Lightwave Technology **26**, 73–78 (2008).